UNIVERSITY OF CALIFORNIA,
IRVINE

The Combined Quantum and Electrochemical Capacitance of Carbon Nanotubes and In-Solution Nanoscale Capacitance Measurements

DISSERTATION

submitted in partial satisfaction of the requirements
for the degree of

DOCTOR OF PHILOSOPHY

in Physics

by

Jinfeng Li

Dissertation Committee:
Professor Peter J. Burke, Chair
Professor Ilya N. Krivorotov
Professor Zuzanna S. Siwy

2019

DEDICATION

To

my parents, sister, friends, and everyone along the way.

TABLE OF CONTENTS

LIST OF FIGURES

LIST OF TABLES

ACKNOWLEDGMENTS

First and foremost, I would like to thank my advisor Professor Peter J. Burke for his tremendous support and guidance throughout my Ph.D. studies at UC Irvine. His insight and continued support allowed me to conduct meaningful research and grow to become a qualified researcher.

I want to thank my committee members, Professor Ilya N. Krivorotov and Professor Zuzanna S. Siwy for agreeing to be on my thesis committee as well as my qualification committee previously. I am grateful for their valuable advice, discussions, and patience during all the meetings as well as email communications.

I further would like to thank my lab mates including Will Wang, Katayoun Zand, Ted Pham, Weiwei Zhou, Phi Pham, and Zahra Nemati for their endless help, discussion and valuable collaboration in research projects.

I want to thank the funding support from the Army Research Office through the ARO-MURI Program, ARO-Core Grants, and DURIP (Contract Nos.: W911NF-11-1-0024, W911NF-18-1-0076, and W911NF-15-1-0376), National Institutes of Health (Contract Nos.: CA182384), and the French American Cultural Exchange (FACE) Partner University Fund program.

I also greatly appreciate the help I have received over the years from the Integrated Nanosystems Research Facility (INRF) staff and the Irvine Materials Research Institute (IMRI). They provided me with training and access to the fabrication and characterization tools that were crucial to my research.

Finally, I would like to acknowledge my parents and sister for their love, understanding, trust, and unwavering support. This thesis is dedicated to them.

CURRICULUM VITAE

Jinfeng Li

2011	B.A. in Physics Jilin University, Changchun, China
2010-2012	Research Assistant, Laboratory of Polymer Physics and Chemistry Institute of Applied Chemistry, Changchun, China
2012-2014	Teaching Assistant, Department of Physics University of California, Irvine, California
2013-2019	Research Assistant, Peter Burke Lab University of California, Irvine, California
2019	M.S in Physics University of California, Irvine, California
2019	Ph.D. in Physics University of California, Irvine, California

PUBLICATIONS

10 "Measurement of the Combined Quantum and Electrochemical Capacitance of a Carbon Nanotube Enabled by an Integrated On-Chip Shield", **J. Li**, P. Burke, Submitted, 2019

9 "Carbon-Nanotube–Electrolyte Interface: Quantum and Electric Double Layer Capacitance", **J. Li**, P. Pham, W. Zhou, T. Pham, P. Burke, ACS Nano, 12(10), 9763-9774, 2018

8 "Scanning Microwave Microscopy of Vital Mitochondria in Respiration Buffer", **J. Li**, Z. Nemati, K. Haddadi, D. C. Wallace, P. J. Burke, IEEE/MTT-S International Microwave Symposium, Philadelphia, Pennsylvania, Jun. 10-15, 2018

7 "Sensing the Electrical Activity of Single Ion Channels with Top-Down Silicon Nanoribbons", W. Zhou, L. Mu, **J. Li**, M. Reed, and P. J. Burke, Nano Futures, 2(2), 025008, 2018

6 "Scalable and Reusable Micro-Bubble Removal Method to Flatten Large-Area 2D Materials", P. H. Q. Pham, N. V. Quach, **J. Li**, and P. J. Burke, Applied Physics Letters, 112(16), 163106, 2018

5 "Broadband Impedance Match to Two-Dimensional Materials in the Terahertz Domain", P. Pham, W. Zhang, N. Quach, **Ji. Li**, W. Zhou, D. Scarmardo, E. Brown and P. J. Burke, Nature Communications, 8(1), 2233, 2017

4 “Resistive Flow Sensing of Vital Mitochondria with Nanoelectrodes”, K. Zand, T. Pham, **J. Li**, W. Zhou, D. C. Wallace, P. J. Burke, Mitochondrion, 37, 8-16, 2017

3 “Controlling Nucleation Density While Simultaneously Promoting Edge Growth Using Oxygen-Assisted Fast Synthesis of Isolated Large-Domain Graphene”, P. Q. Pham, W. Zhou, N. Quach, **J. Li**, J. Zheng, P. J. Burke, Chemistry of Materials, 28(18), 6511–6519 2016

2 “Cristae Remodeling Causes Acidification Detected by Integrated Graphene Sensor During Mitochondrial Outer Membrane Permeabilization”, T. D. Pham, P. Q. Pham, **J. Li**, A. G. Letai, D. C. Wallace, P. J. Burke, Scientific Reports, 6, 35907, 2016

1 “Charging the Quantum Capacitance of Graphene with a Single Biological Ion Channel”, Y. Y. Wang, P. Ted, K. Zand, **J. Li**, and P. J. Burke, ACS Nano, 8(5), 4228-4238, 2014

ABSTRACT OF THE DISSERTATION

The Combined Quantum and Electrochemical Capacitance of Carbon Nanotubes and In-Solution Nanoscale Capacitance Measurements

By

Jinfeng Li

Doctor of Philosophy in Physics

University of California, Irvine, 2019

Professor Peter J. Burke, Chair

The intimate contact between the electrons in a carbon nanotube and solvated ions in a liquid electrolyte gives rise to a unique electrostatic situation not seen in previous electrochemical cells: electric fields are confined to dimensions comparable to the radius of a solvated ion, and a sharply varying quantum density of states of the electrons directly affects the electrostatics. The corresponding capacitance, in this case, consists of two main types of capacitance in series: a quantum component arising from the electronic density of states and an electrochemical component arising from the ion screening and diffusion.

To quantitatively study these capacitances, in Chapter 2, we start with measuring the ensemble average, complex, frequency dependent impedance between a purified semiconducting nanotube network and an aqueous electrolyte at different ionic concentrations. The potential dependence of the capacitance is convoluted with the potential dependence of the in-plane conductance of the nanotube network, which we model using a transmission-line model to account for the frequency dependent in-plane

impedance as well as the total interfacial impedance between the nanotube network and the electrolyte. In Chapter 3, we push the measurement technique to resolve the liquid-gate capacitance down to a single nanotube level. Due to the atomic dimensions, the small capacitance (~ 100 aF) has been a challenge for researchers to measure and observe directly. In order to resolve the small capacitance (of order 100 aF) above the background stray capacitance (of order 100 pF), we designed, developed, and implemented an integrated, on-chip shield. With this system, we measure the capacitance of one to a few nanotubes quantitatively as a function of both bias potential and ionic concentration at room temperature. The ionic strength dependence of the capacitance is expected to have a root cause from the electrochemical capacitance, which we model using a modified Poisson Boltzmann equation. The relative contributions from those two capacitances can be quantitatively decoupled.

So far, the capacitance measurements are confined in DC-KHz domain, where most Nano-biosensors operate. However, ionic screening effect due to mobile ions prevents target-sensing beyond Debye length. In Chapter 4, we demonstrate capacitance measurement/mapping in GHz domain using scanning microwave microscopy (SMM) and use it to image vital mitochondria in respiration buffer. The SMM is combined with an interferometric and tuned reflectometer to optimize the sensitivity even in an electrophysiologically relevant liquid (hence conducting) environment.

Chapter 1: Introduction

One of the most fundamental properties of the interface between matter and liquid is the capacitance of that interface. The capacitance governs the ability to carry charge, and therefore determines the final fate of any electrical currents flowing through that interface. In biological systems, the capacitance directly affects the speed of propagation of the action potential along neurons,[1] and plays an important role in many other bio-electronic phenomenon, including the beating of a cardiomycyte,[2] as well as the creation and consumption of energy in organelles such as chloroplasts for photosynthesis and mitochondria for oxphos and ATP synthesis.[3] The capacitance also plays an important role in energy storage technologies such as batteries and supercapacitors,[4–6] and governs the behavior of numerous electrochemical sensors.[7]

Bringing an artificial interface made of electronic systems in contact with such biological and chemical systems, one can create functional devices for the applications of biosensing, chemical sensing, fuel cell, and energy storage. Because many sensing targets in the biological and chemical world are of size on a nanometer scale, one would expect a similar-sized (nanoscale) electrode to interact with them for the best sensitivity and resolution. Similar requirements go for energy storage to increase the energy and power density. With the modern advent of nanomaterials and nanofabrication, that has been possible. Reduced dimensional materials such as 2d materials (graphene and beyond graphene), 1d materials (nanoribbons, nanotubes, nanowires), 0d materials (quantum dots) give rise to a whole class of electronic devices in which the size of the structure becomes

comparable to that of sensing targets and even the electron wavelength. At the same time, due to the reduced size, quantum effect becomes unneglectable. Just as Bohr surmised at the dawn of quantum mechanics that the wave function as an electron circles an atom must return to its original value (hence the allowed wavelengths and energies in an atom are quantized), this gives rise to quantization of energy levels within any solid whose size approaches the electron wavelength in any dimension.

What is the effect of this on the capacitance between a reduced dimensional system and a liquid electrolyte? While this has been addressed in theory, in practice for d < 2, it has been impossible (until now) to answer for one very important practical reason: It is almost immeasurably small. The quantum capacitance of a nanotube is generally of order $4e^2/\pi\hbar v_F \approx 0.4fF/\mu m$. In dry systems, it is possible to isolate the nanodevice from the system[8] but in an electrolyte liquid system, the electrolyte contacts everything and creates a stray overlap capacitance between contact electrodes and the nanodevice, which swamps the signal that is being measured.

At the same time, the "classic" Debye layer capacitance deviates from textbook behavior when the radius of curvature of the electrode becomes comparable to the solvated ion radius, also of the order of 1 nm. This can occur in one of two topologies: Nano-caves, and nano-electrodes. In a nano-cave, the cave size becomes small in a porous material giving non-trivial capacitance, changing the behavior by up to 3 times the classic calculation. This was discovered experimentally and only later explained by electrochemical simulations.[9–12] In nano-electrodes, the electrode protrudes into the liquid, and the predicted behavior deviates substantially from the classic one.[13–16] The results of both of these effects

(quantum and electrochemical) give rise to a new regime of electrochemical behavior for nanosystems, qualitatively different from both by new well-studied dry nano-systems and classic large area electrochemical systems.

To quantitatively study these capacitances, in Chapter 2, we start with measuring the ensemble average, complex, frequency dependent impedance between a purified semiconducting nanotube network and an aqueous electrolyte at different ionic concentrations. The potential dependence of the capacitance is convoluted with the potential dependence of the in-plane conductance of the nanotube network, which we model using a transmission-line model to account for the frequency dependent in-plane impedance as well as the total interfacial impedance between the nanotube network and the electrolyte. In Chapter 3, we push the measurement technique to resolve the liquid-gate capacitance down to a single nanotube level. Due to the atomic dimensions, the small capacitance ($\sim$ 100 aF) has been a challenge for researchers to measure and observe directly. In order to resolve the small capacitance (of order 100 aF) above the background stray capacitance (of order 100 pF), we designed, developed, and implemented an integrated, on-chip shield. With this system, we measure the capacitance of one to a few nanotubes quantitatively as a function of both bias potential and ionic concentration at room temperature. The ionic strength dependence of the capacitance is expected to have a root cause from the electrochemical capacitance, which we model using a modified Poisson Boltzmann equation. The relative contributions from those two capacitances can be quantitatively decoupled. This technique, proven in concept for the case of carbon nanotubes, is applicable to a broad class of reduced dimensional devices, including nanowires, nanoribbons, and quantum dots, of any material.

So far, the capacitance measurements are confined in DC-KHz domain, where most Nano-biosensors operate. However, ionic screening effect due to mobile ions prevents target-sensing beyond Debye length. In Chapter 4, we demonstrate capacitance measurement/mapping in GHz domain using scanning microwave microscopy (SMM) and use it to image vital mitochondria in respiration buffer. The SMM is combined with an interferometric and tuned reflectometer to optimize the sensitivity even in an electrophysiologically relevant liquid (hence conducting) environment. This represents proof of concept of SMM in electrophysiologically active organelles, which provides information complementary to optical and electron microscopies. Since this approach is fully functional in biological buffer, it enables studies of the changes mitochondria undergo under different chemical environments, such as cell death signals (e.g. BCL2 proteins), different metabolites, mitochondrial ROS, and many other studies, all in real time.

Chapter 2: Background

2.1 Carbon nanotube and its electronic properties

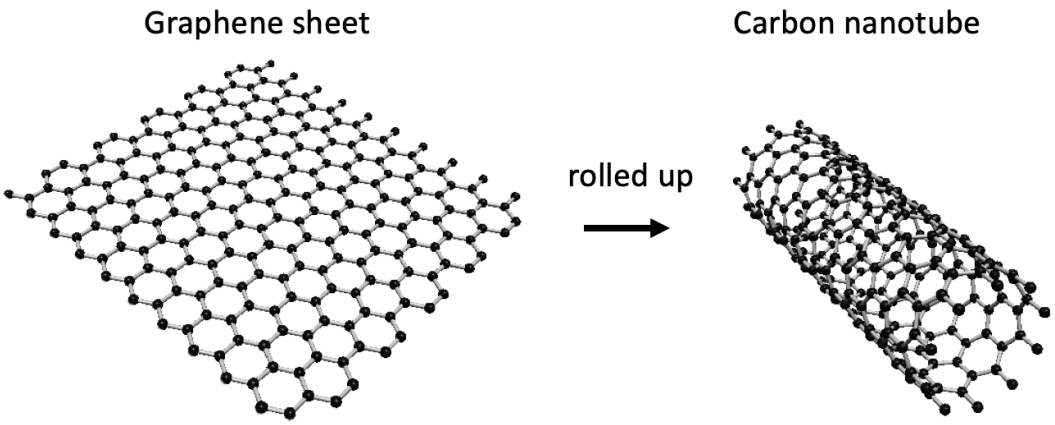

Figure 2.1: Graphene sheet and carbon nanotube.

Carbon nanotubes are hollow cylindrical carbon molecules, in which the carbon atoms are sp^2-bonded and structured in a honeycomb lattice. It can be visualized as a single layer of graphite (called graphene) rolled up into a tube. To understand the electronic properties of carbon nanotubes, one can start with that of graphene. Graphene is a purely 2D material with carbon atoms covalently bonded in a hexagonal honeycomb lattice (Figure 2.1). The bond length between neighboring carbon atoms is ~0.142 nm, and each unit cell of the lattice has two atoms. Because of the 2D confinement, graphene has only one allowed state k_z in the perpendicular direction, and continuously allowed states (k_x, k_y) in the plane of the graphene. Figure 2.2a shows the band structure of graphene. The valence band and conduction band of graphene join each other at the corners (K points) of the Brillouin zone, showing a cone like structure termed Dirac cone. The energy dispersion relation near the K points is linear.

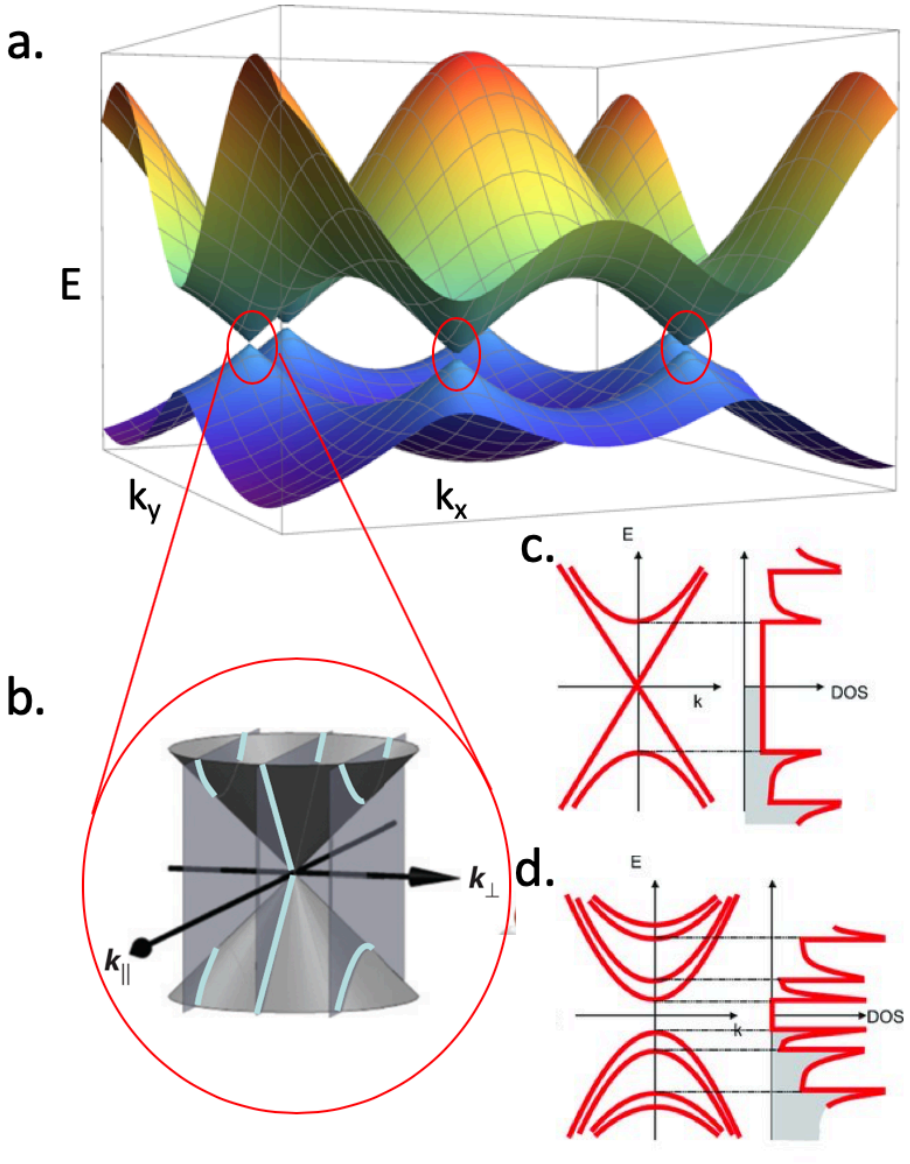

Figure 2.2: Band structure of graphene and nanotube. (a) The band structure of graphene, where the conduction and valence band join each other at the K points. (b) Zoom-in view of the band structure near the K points, shows a linear energy dispersion relation and is well-approximated as cones. (Ref. [17]) (c, d) The quantization slices of the 2D band structure of graphene results in the 1D band structures of nanotubes. Depending on whether the slices pass through the K points, the nanotube can be metallic or semiconducting.(Ref. [18])

Rolling up a single layer graphene to form a cylindrical tube, impose additional periodic boundary conditions on the wavefunction in the circumferential direction. For a nanotube whose diameter is ~1 nm, available electronic states in the circumferential direction

becomes strongly quantized. The quantization results in discrete slices on the 2D band structure of graphene, with each slice corresponding to a sub-band of the nanotube (Figure 2.2b). Depending on the diameter and the rolling-up angle (called chiral angle) of a nanotube, the gap and direction of the slice varies. If the slice pass through the tips of Dirac cones (as shown in Figure 2.2 b, c), the corresponding valence and conduction sub-bands connect each other, resulting in a metallic nanotube. Otherwise (as shown in Figure 2.2d), all sub-bands have gaps, the nanotube is semiconducting.

2.2 Quantum capacitance

The capacitance of a regular conductor is defined as the change of the electric charge it stores divided by the corresponding change in its electric potential. The stored charges distribute within the conductor in a way to minimize the total electrostatic energy. Hence the capacitance is fully determined by the geometry of the conductor and its geometric relationship with the reference conductor (denoted as C_g). However, in the quantum electronic systems who have limited density of states at the Fermi level (such as a carbon nanotube), adding charges need additional energy to occupy available electronic states in higher energy level, which results in a new contribution to the total capacitance, termed as quantum capacitance C_q.

$$\frac{1}{C_{tot}} = \frac{1}{C_g} + \frac{1}{C_q} \tag{2.1}$$

The quantum capacitance C_q can be calculated from the density of states function.

$$C_q(V_{ch}, T) = \frac{dQ}{dV_{ch}}$$

$$= \frac{d}{dV_{ch}} e \int dE\, f_0(E - eV_{ch})\, \rho(E) \tag{2.2}$$

$$= e^2 \int dE\, F_T(E - eV_{ch})\, \rho(E)$$

where, Q is the total charge of the system, e is the elementary charge, $eV_{ch} = E_F$ is the Fermi energy, $f_0(E) = 1/(e^{E/k_BT} + 1)$ is the Fermi function, $F_T(E) = (4k_BT)^{-1}\mathrm{sech}^2(E/2k_BT)$ is the thermal broadening function, $\rho(E)$ is the density of states function of the system.

2.3 Electrochemical double layer capacitance

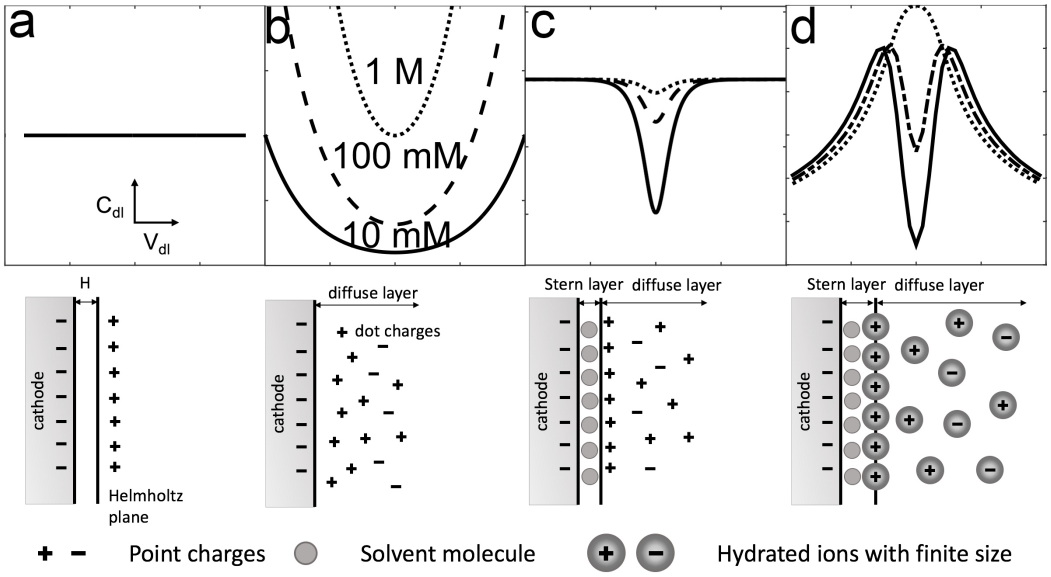

Figure 2.3: Evolution of the electric double layer models. Top panel: capacitance vs. potential $C_{dl}(V_{dl})$ at different ionic concentrations. Bottom panel: the arrangement of solvated ions near the interface. (a) Helmholtz model, (b) Gouy-Chapman model, (c) Gouy-Chapman-Stern (GCS) model, (d) GCS model with the effect of ion size

When a solid electrode is brought in contact with a liquid electrolyte, the electrons at the surface of the electrode are coupled with the ions in the electrolyte, forming an electric

double layer. The electric double layer was first modeled by Helmholtz as a two-plate capacitor, with the metal electrode and electrolyte electrode separated by a certain distance caused by finite ion size (Figure 2.3a). Gouy and Chapman improved the model by considering the electrolyte side as the diffusive structure of counter-ions loosely accumulated to the metal electrode surface (Figure 2.3b). Later, Stern combined the Helmholtz model and Gouy-Chapman model, and described the double layer as two capacitances in series: the Helmholtz's plate capacitance in series with the Gouy-Chapman's diffuse capacitance (Figure 2.3c).[19] The Gouy-Chapman-Stern (GCS) model has become the popular model for the electric double layer. Modern electrochemistry theories still use the GCS model as a framework but include more effects such as the finite ion size and short-range correlations to approach the real system. The Poisson-Boltzmann (PB) equation (Debye–Hückel theory) and the mean sphere approximation (MSA) are two popular approaches adapted to calculate the properties of realistic electrolyte systems.[20,21] The original PB methods treat ions as point charges in a continuous dielectric medium and ignore the short-range correlation of ions, which provides a limiting prediction, valid at low concentrations. MSA overcomes this limitation being able to work well in strong electrolytes, by modeling ions as hard charges spheres in a continuous medium, and includes the correlation effect. Modified PB methods (used in this paper) can also account for the effect of non-zero ion size and close-range correlation, which is easier to compute and can provide approximately the same level of accuracy as MSA. More advanced methods such as classical molecular dynamics (MD) simulations and DFT-based *ab initio* MD simulations,[15,22,23] which treat the medium as discrete molecules with realistic

intermolecular correlations, provide a more detailed model for the system, especially for multivalent molecules. However, MD methods require large computational power.

The bottom panel of Figure 2.3d shows the double layer structure based on the Gouy-Chapman-Stern (GCS) model.[19,24] Near the surface of the charged SWNT electrode, electrostatic interactions cause counter-ions to accumulate to the surface of the electrode, forming a compact Stern layer and a loose diffuse layer. In the Stern layer, the compacted layer of counter-ions strongly attaches to the electrode surface with solvent molecules between them. The solvent molecule can be considered as the hydration shell of the electrode, whose thickness changes according to ionic concentration. In the diffuse layer, free ions with thermally activated movement loosely accumulate near the Stern layer under the influence of electrostatic force. The accumulation of counter-ions in these two layers electrically screens the electrode surface, resulting in electric potential decaying exponentially to zero from the surface to the bulk solution.

Ionic species in the solution are governed by motion dynamics that has a coupled influence from diffusion and electrostatic forces. This behavior can be described by Convection–diffusion equation together with Poisson's equation. From these two equations, and considering both equilibrium state and binary symmetric electrolytes, the potential distribution can be accounted for by the original Poisson-Boltzmann equation:[19]

$$\nabla \cdot (\varepsilon_r \varepsilon_0 \nabla \varphi) = 2\rho_q \sinh\left(\frac{q\varphi}{k_B T}\right) \tag{2.3}$$

where φ is the electric potential distribution in space, $\rho_q = q \cdot N_A \cdot c_0$ the charge density of cation or anion in a symmetric electrolyte solution, c_0 the molar concentration of ion

species, N_A Avogadro constant, and $q=z\cdot e$ is the charge of the ions with valence z and the electron charge e.

For a planar electrode, there is an analytic solution for the Poisson-Boltzmann equation, which can give the double layer capacitance,[19]

$$\begin{aligned}\frac{1}{C_{dl}} &= \frac{1}{C_{Stern}} + \frac{1}{C_{diffuse}} \\ &= \frac{d_s}{\varepsilon_r \varepsilon_0} + \frac{1}{(2\varepsilon_r \varepsilon_0 z e \rho_q / k_B T)^{1/2} \cosh\left(z e \varphi_H / 2 k_B T\right)}\end{aligned} \tag{2.4}$$

where C_{Stern} is the capacitance of the Stern layer, $C_{diffuse}$ the capacitance of the diffuse layer, d_s the thickness of the Stern layer, and φ_H the potential at the outer Helmholtz plane.

Chapter 3: Quantum and Electrochemical Capacitance of Carbon Nanotube Network and Graphene

3.1 Introduction

What is the capacitance between a 1d quantum wire (such as a carbon nanotube) and an electrolyte? This is probably the most fundamental scientific issue for any application where nano-electrodes interface with electrolyte solutions, including for example electrochemical storage systems[4,5] (supercapacitors, batteries, fuel cells) and electronic interfaces with biological systems, such as chemical and biological sensors,[7] neural interfaces, and even electronic actuation of chemistry. Because of the reduced (almost atomic) size compared to traditional electrodes, as well as the low electronic density and quantum effects associated with the Pauli exclusion principle, the capacitance is theoretically expected to have comparable contributions from two significant phenomena: quantum and electrochemical.

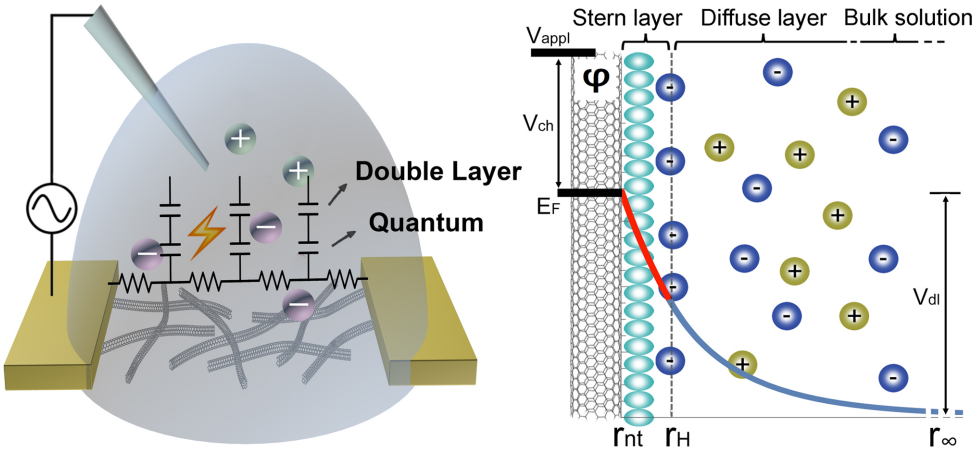

Figure 3.1: Left panel: 3D cartoon of the system under study. Right panel: Schematic of the double layer structure at the nanotube surface. The potential distribution along the radial direction consists of the chemical potential shift (Vch), followed the decay in the Stern layer (red), and the diffuse layer (blue).

One of the most fundamental questions in electrochemistry is, what is the capacitance between an electrode and an electrolyte? The electrochemical portion in planar geometries is well studied, and sophisticated models based on the now "textbook" Gouy-Chapman-Stern (GCS) model[19] which take into account, the effect of ion size[13] and varied Stern layer thickness[25] have been successful in describing a wide variety of electrode-electrolyte systems. However, with the modern advent of nano-materials, a plethora of geometries are now available with electrodes with feature sizes (*e.g.* radius of curvature, pore size, *etc.*) smaller than the Debye length, even approaching the size of a solvated ion. In this case, profound differences from textbook GCS models are expected. What is traditional text book electrochemistry must be discarded and new theories, driven by comprehensive, quantitative experimental data on model systems, will take their place.

As an example, in so-called nano-porous materials,[6,26–30] solution accessible caverns in amorphous, random materials provide a large effective surface area, hence potential applications in supercapacitors. Researchers found that the capacitance per area diverges

from classical, textbook GCS behavior when the average spacing ("pore") becomes of order 1 nm.[9–12,30–32] Here, in that context, "pore" is a random approaching of two electrode regions (positions where the cavern drops to a small value), not a cylindrical hole. Another example system is so-called nanotube paper,[33–35] where the nanotubes are treated as thin wires in a dense spaghetti, also with a large effective surface area. The nanotube paper should include multiple effects such as finite-radius of the nanotubes, as well as other non-GCS effects when nanotube spacing becomes comparable to the Debye length, in analogy with the nano-porous materials. However, due in part to the complexity of the geometry and the electrochemistry, to our knowledge, no such a comprehensive study has been performed, leaving open the possibility of improved nanotube paper supercapacitors if the fundamental underlying science of the electrochemistry can be understood.

An additional significant effect, that of the quantum capacitance, has not been well considered in the context of either nano-porous materials or nanotube paper. The quantum capacitance arises from system's low density of states near the Fermi level,[36] and has been studied in a dry environment.[37] Its effect on the electrical behavior of the capacitance between a material with small radius of curvature and an electrolyte solution has not been well studied, although it has been demonstrated in planar large area graphene electrodes[38,39] with essentially infinite radius of curvature, where the classical textbook GCS describes well the electrochemical capacitance.

In order to elucidate the contributions of the small radius of curvature on electrode-electrolyte capacitance in a well-controlled, model system, as well as study the effects and significance of the quantum capacitance, we have chosen a model system with well

understood, well controlled radius of curvature, and constant (rather than random) cylindrical geometry, that of a sparse array of carbon nanotubes horizontally distributed on a solid (insulating) surface. In this limit, the nanotube-nanotube spacing is much larger than the Debye length, allowing us to treat each nanotube individually. We assume the electrolyte does not penetrate to the inside of the nanotube, so each nanotube is treated as a solid cylinder electrode. (The effect would be small even if it did, which we discuss in detail in the main manuscript below.) In contrast to the nano-porous materials, which have a fractal 3d like geometry, this geometry enables us to carefully study the effects of quantum capacitance and small radius of curvature in one system. A priori, in this system, both the quantum capacitance and the double layer capacitance are comparable in value and interact with each other. One or the other can dominate the total capacitance, depending on the detailed parameters such as ionic strength and applied potential.

This fundamental study is the first step towards a more comprehensive understanding of the dense limit, that of nanotube paper, which is beyond the scope of this paper. However, as this is the fundamental, scientific study of the electrochemical and quantum capacitance of a nano-cylinder geometry, it is expected to have applications in many fields beyond supercapacitors.

With this in mind, here we present quantitative measurements and models of the capacitance between carbon nanotubes and an electrolyte, including developing a comprehensive, and quantitative model for 1d quantum wire to electrolyte electrochemical capacitance as well as the relative magnitude of both the electrochemical capacitance, and the quantum capacitance in liquid. To do this, we measure the differential capacitance

between SWNTs and electrolyte solution, using a semiconducting SWNT network. To ascertain the various contributions to this total interfacial capacitance, we use electrochemical impedance spectroscopy (EIS) to determine the ensemble average, complex, frequency dependent impedance (from 0.1 Hz to 1 MHz) between a purified (99.9%) semiconducting nanotube network and an aqueous electrolyte (KCl) at different concentrations between 10 mM and 1 M. By the interfacial capacitance, we mean the total capacitance, which includes contributions from both the quantum and double layer capacitance in series. We find a total capacitance per tube of order 1 fF/μm and map its dependence on bias and electrolyte strength. This fundamental and experimental study of the total capacitance between a 1d material and an electrolyte provides a comprehensive scientific foundation for understanding interactions between any 1d electronic system and liquid electrolytes, a growing area of research for a variety of fields from energy to biology.

3.2 Device description and measurement configuration

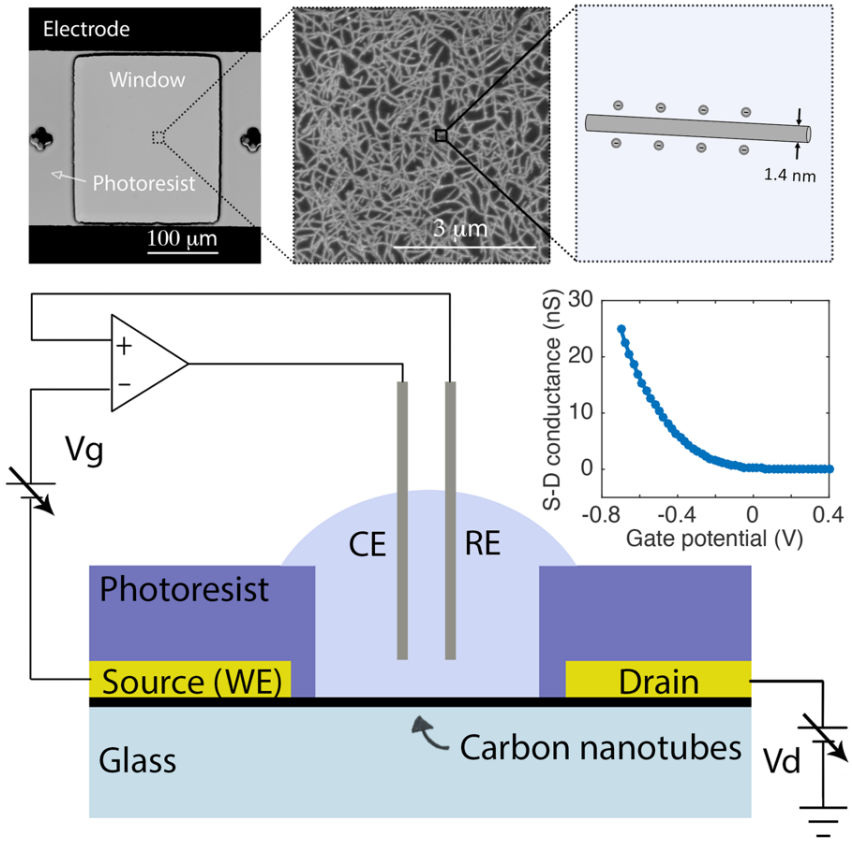

Figure 3.2: Single-walled carbon nanotube (SWNT) network device illustration and measurement configuration. Schematic of the interfacial impedance measurement of the SWNT network on an inert glass substrate with source and drain electrodes covered by photoresist and the channel exposed to electrolyte solution. The nanotube network channel is liquid gated by an aqueous electrode and the impedance of the SWNT-electrolyte interface is measured with an AC perturbation added on the gate potential. The upper panel shows the optical micrograph of the device, the SEM image of the nanotube network, the geometry of SWNTs and the transfer characteristic of the device.

Figure 3.2 shows a schematic of the measurement setup using a thin film transistor type device with single-walled carbon nanotube (SWNT) networks as the semi-conducting channel. The upper panel shows the optical and the scanning electron microscopy (SEM) images of the actual device, along with a diagram of the geometry of the SWNTs, and the DC conductance characteristic. The device fabrication is detailed in the methods section 3.4 .

Briefly, a SWNT network is transferred to an inert glass substrate with Au electrodes deposited on two sides as the source and drain electrodes, with channel length varying from 40 μm to 300 μm and a fixed width of 200 μm. Standard photolithography was used to insulate the electrodes, while exposing the SWNTs to solution through a photoresist window. Using glass as substrate instead of Si/SiO_2 wafer minimizes the background capacitance. The exposed SWNTs have relatively high density (~12 SWNTs/μm^2) and form a uniform random network,[40] as shown in the SEM image, ensuring a good current pathway between the source and drain electrodes.

An ionic solution consisting of 10 mM to 1M potassium chloride contacts the SWNTs through the exposed window and is used as a "solution gate". The gate potential is controlled and varied using a potentiostat (Gamry Reference 600) with a standard three-electrode electrochemical configuration[19] as shown in Figure 3.2. Here the SWNTs act as the working electrode (WE), and are controlled with respect to the Ag/AgCl reference electrode (RE) and a platinum counter electrode (CE). The gate potential window is limited to between -0.7 V (SWNTs in an on-state) and 0.4 V (SWNTs in an off-state) to avoid water oxidation at the SWNTs surface. As there are no active redox species in the potential range in the solution, we expect only trace redox (Faradaic) currents, allowing us to isolate the capacitance exclusively. A small AC perturbation (10 mV, 0.1 Hz – 1 MHz) was superimposed onto the gate potential and the current response was measured to determine the frequency dependent impedance information of the SWNT-electrolyte interface. Before the impedance measurement, the in-plane source-drain conductance of the SWNT network as a function of gate potential was characterized using a source measurement unit.

3.3 Results and Discussion

3.3.1 DC characteristics

The conductance curve in Figure 3.2 shows the transfer characteristics of the SWNT network with length 250 μm and width 200 μm. It is a typical p-type depletion curve with source-drain conductance as a function of liquid gate potential, measured by sweeping the gate potential from -0.7 to 0.4 V at a fixed source-drain bias 100 mV. The on/off ratio is ~1000, demonstrating that the network is dominated by semiconducting SWNTs. This "background current" may be non-zero due to redox reactions with trace impurities in the electrolyte. This term is sometimes called "leakage current", using the language of semiconductors where the liquid is serving as the gate. The (DC) leakage current between the electrolyte and the SWNT film is negligible compared to the (DC) source-drain current, confirming the interpretation that only capacitive current flows between the SWNT film and the electrolyte in our experiments. This enables us to accurately determine the DC in-plane SWNTs conductance and focus on the interface capacitance.

3.3.2 Capacitance measurement at 10 Hz

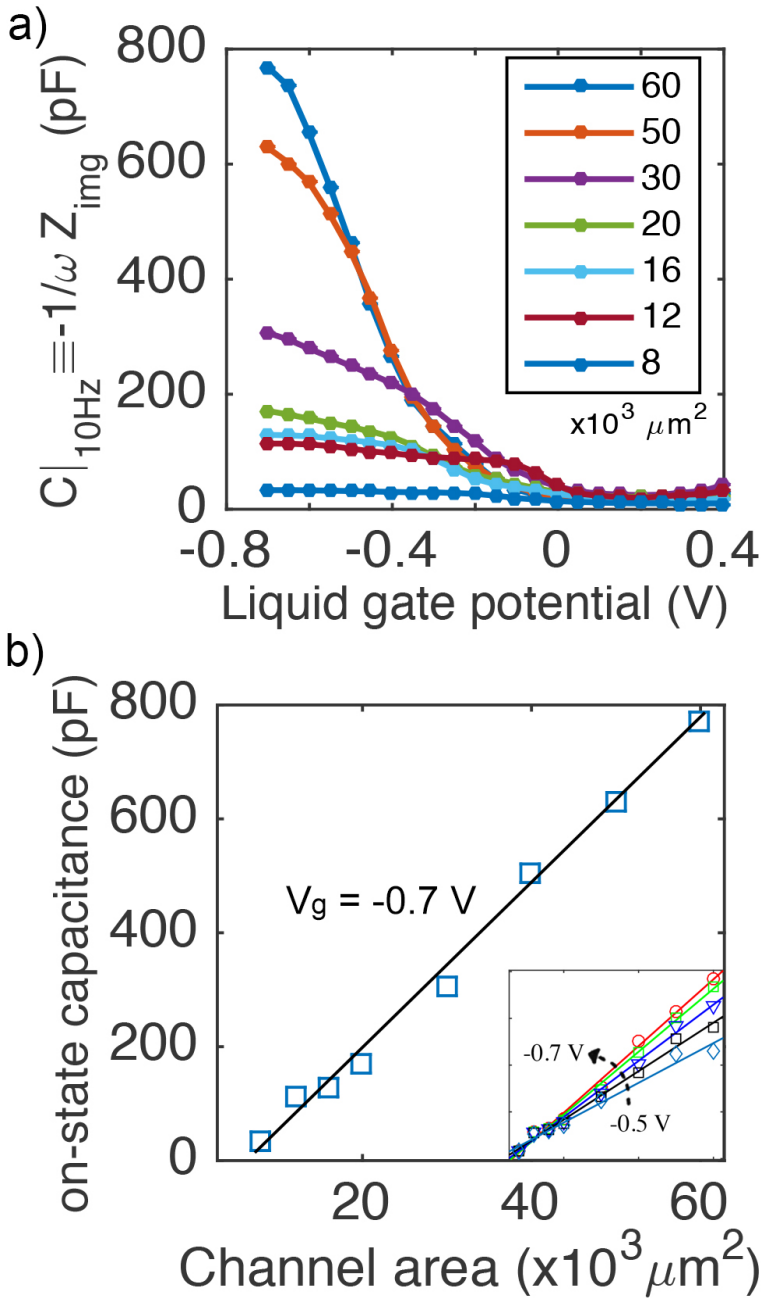

Figure 3.3: SWNT network-to-electrolyte capacitance with different channel areas measured at a single frequency 10 Hz. (a) Capacitance curves as functions of liquid gate potential with varied channel areas, measured on the same sheet of SWNT network film to ensure consistence of SWNT density. (b) The linear relationship between the on-state capacitance and the corresponding channel areas at gate potential -0.7 V, and over a range of gate potentials in the inset.

In order to determine the impedance (hence capacitance) between the SWNT network and the electrolyte, a small AC perturbation at 10 Hz was added to the gate potential and

the in phase 10 Hz current was measured with a lock-in analyzer. At sufficiently low frequencies the system can be modeled as a simple capacitor (discussed in more detail later). The capacitance can be determined from the measured impedance using the relationship $C \equiv -1/\omega \cdot Z_{img}$. Figure 3.3a shows the measured capacitances of various devices with different channel areas on the same chip. Within the positive gate potential window where most SWNTs are in the off-state, there is a parasitic capacitance ~20 pF. As the SWNTs turn on gradually, the capacitances trend to saturate and show a clear correlation with the channel area. Figure 3.3b shows the capacitance scales in a linear trend with the channel area at gate potentials -0.7 V. The slope of the correlation gives the capacitance area density at values 14.2 fF/μm^2. The linearity remains over the range of gate potential between -0.5 V and -0.7 V, corresponding to the capacitance value of 8.4 – 14.2 fF/μm^2 (the inset of Figure 3.3b).

Using this measured capacitance density and the known SWNT density and average length, we can determine the capacitance per unit length of a single nanotube. The density of SWNTs is estimated from the SEM image. Assuming a straight line with enough length lying on the SWNT network sheet, the probability of a single nanotube with length of l crossing the straight line is:

$$P_i = 2\int_0^{l/2} \frac{2\,Cos^{-1}[2x/l]}{b\,\pi}\,dx = \frac{2\,l}{b\,\pi} \tag{3.1}$$

where b is the width of the SWNT network sheet. Then the SWNT density of the sheet will be:

$$density\ of\ SWNT = N \cdot \frac{\pi}{2\,l} \tag{3.2}$$

where N is the average number of SWNTs that cross the line within a unit length.

By placing 5μm lines randomly on the SEM image of the TFT devices and counting the SWNTs that cross the lines, we can estimate N ≈ 8. The SWNTs used in this experiment are commercially available from Nanointegris, and it have mean diameter of 1.4 nm and mean length of $l=1\mu m$. We estimate the density of SWNTs to be 12.6 SWNTs/μm^2, and mean length of 1 μm. This gives us an estimated value of 0.67 – 1.13 fF/μm (the inset of Figure 3.12) for the total interfacial capacitance between SWNTs and electrolyte with dependence on the gate potential.

3.3.3 Effect of in-plane conductance

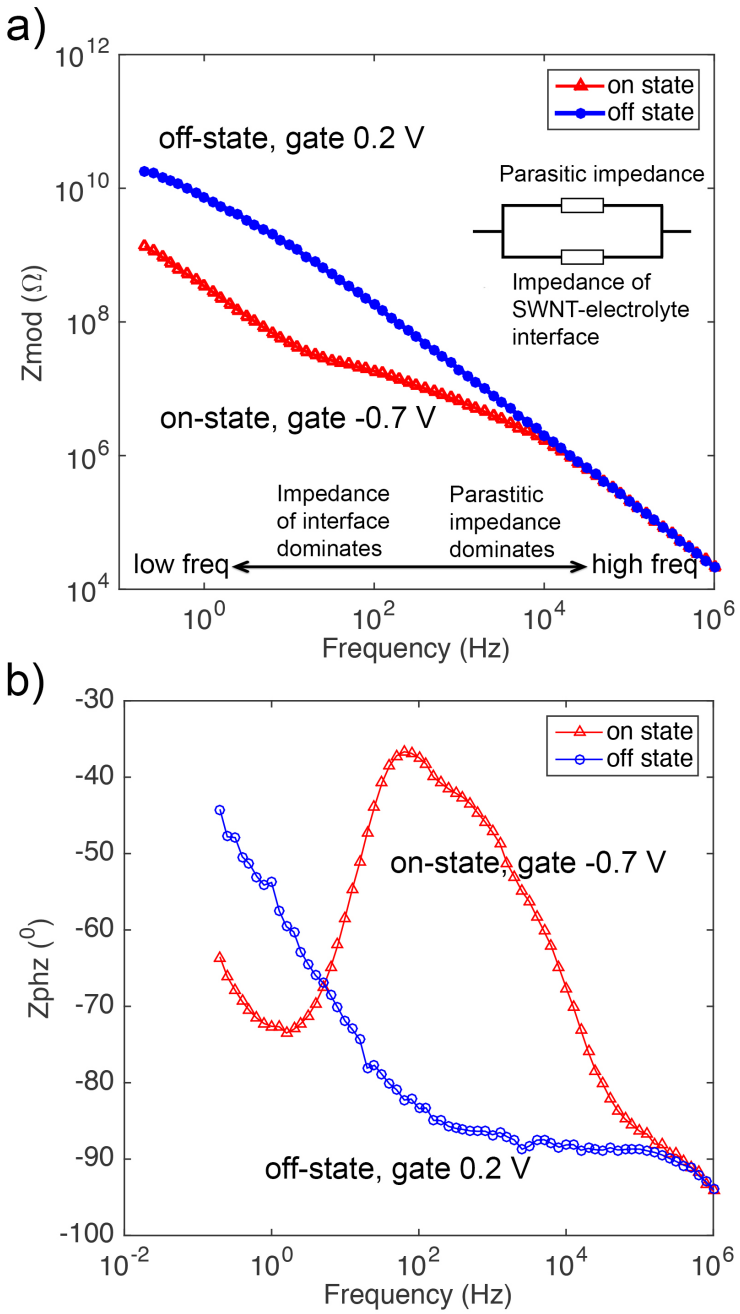

Figure 3.4: Experimental EIS Bode plot of the SWNT-electrolyte interface. Impedance spectrums measured at off state (blue curve) and on state (red curve) are plotted with (a) impedance modulus vs. frequency and (b) impedance phase vs. frequency. The inset circuit demonstrates the parallel relationship between the parasitic impedance and the impedance of interest.

For more quantitative studies, we must take into account the in-plane conductance of the SWNT network. Although a single frequency measurement provides some insight,

electrochemical impedance spectroscopy (EIS) is a much more powerful tool to characterize the system over a broad range of frequencies. Figure 3.4 shows the measured impedance spectrum of the same device, where the red curves correspond to the on-state impedance spectrum with gate potential at -0.7V and the blue curves correspond to the off-state impedance spectrum with gate potential at 0.2V. In the off-state the nanotubes are not conducting, so the only impedance measured is the parasitic impedance between the contact electrodes and the electrolyte. Independent experiments show that this parasitic impedance scales linearly with the area of the contact electrodes confirming this interpretation (see Figure 3.5). Also, at high frequencies, the parasitic impedance dominates, and the on-state and off-state curves merge, as expected. Since we have measured the complete, complex impedance, we can subtract the parasitic impedance to determine the SWNT-electrolyte impedance using:

$$Z_{SWNT-electrolyte} = Z_{measured} - Z_{parasitic} \tag{3.3}$$

where $Z_{parasitic}$ is determined using the off-state or high-frequency measured impedance.

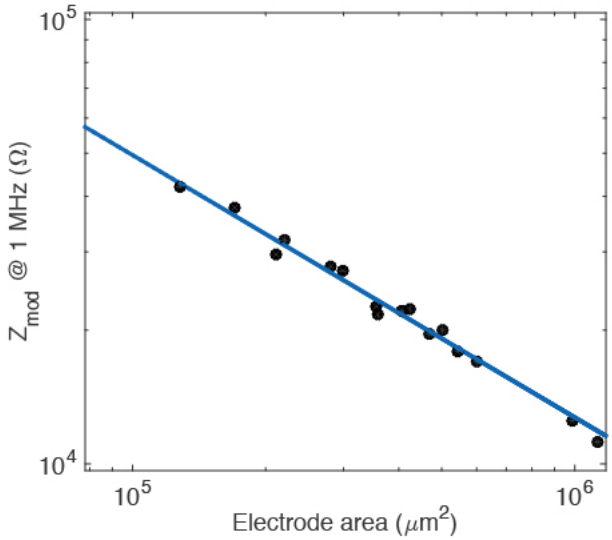

Figure 3.5: Parasitic impedance vs. the area of electrode pads. the strong correlation between the electrode area and the impedance at high frequency (1 MHz). The areas estimation only takes account of the regions of electrodes that are underneath the electrolyte solution. This strong correlation confirms that parasitic current of the device mainly passes from the electrode to the solution through the protective dielectric layer. Hence, the parasitic impedance should be in parallel with the impedance of the SWNT-electrolyte interface.

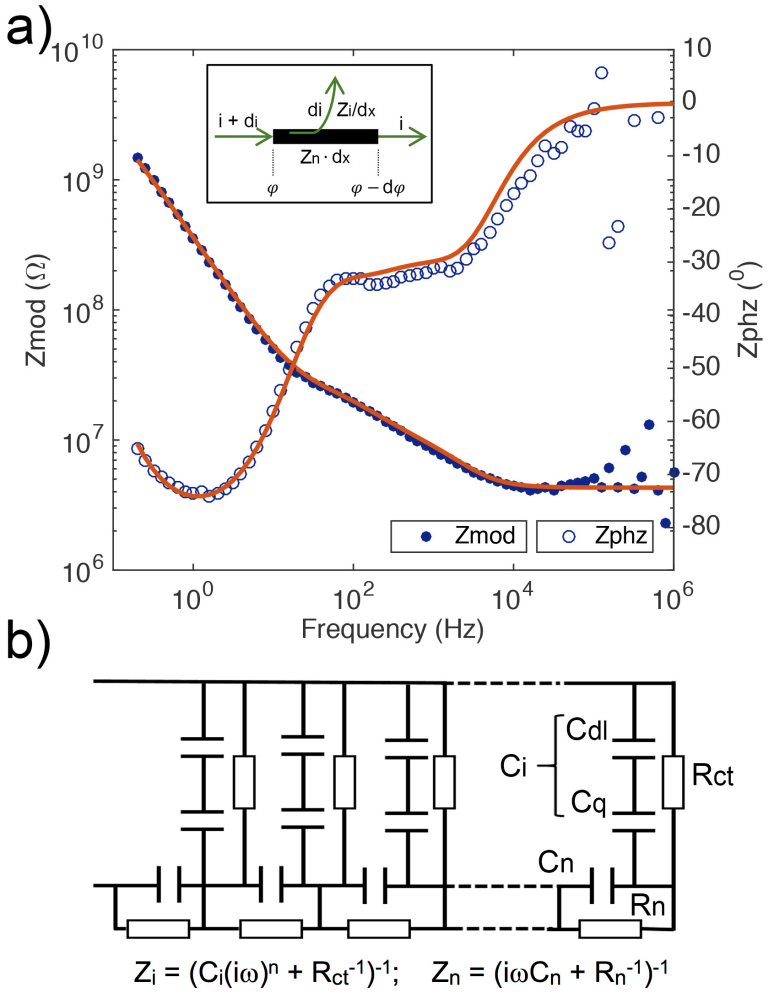

Figure 3.6: Transmission line modeling of the impedance spectrum. (a) Impedance spectrum after subtracting parasitic impedance, fitted by a modified transmission line (TL) model. The inset shows the potential and current variations of a differential length of SWNT network channel. (b) Circuit representation of the transmission line model.

We plot the impedance spectrum of the SWNT-electrolyte interface in Figure 3.6a determined using this procedure. In contrast to most electrochemical experiments, in our experiments, the in-plane conductance of the nanotubes can be lower than the capacitive impedance between the SWNT network and the electrolyte. Therefore, $Z_{SWNT\text{-}electrolye}$ also includes contributions from the in-plane conductance which must be taken into account. In order to do this, we model the system as a distributed in plane and capacitive network ("transmission line", although only Rs and Cs so not like a wave), which includes both the

in-plane impedance of the nanotube network, as well as the network-to-solution impedance. In Figure 3.6b, we diagram the distributed model, which contains all of the important elements: capacitance between the network and the electrolyte, Faradaic (redox) impedance between the nanotube network and the electrolyte, in plane conductance of the nanotube network, and in plane capacitance of the nanotube network. Using this model, we can apply the standard telegraph equations from transmission line theory to find the following relationship between the total (measured) impedance Z and the length of the system as well as the individual components:[41]

$$Z = \frac{\varphi(0)}{i(0)} = (Z_i Z_n)^{1/2} \coth[L(Z_n/Z_i)^{1/2}] \tag{3.4}$$

where L is the channel length of the SWNTs thin film transistor, and Z_i is the complex impedance per unit length ($\Omega\ m^{-1}$) of the interface, and Z_n is the in-plane impedance-length (Ω m) of the SWNT network, shown in the Figure 3.6b.

The impedance of SWNT-electrolyte interface Z_i has components of resistance and capacitance in parallel. The resistance R_{ct} is due to trace Faradaic current; the capacitance C_i is a combination of double layer capacitance and quantum capacitance.[42] An R||C circuit model can intuitively describe the impedance of different types of interfaces, however experimentally, the interface impedance commonly shows a non-ideal capacitance phenomenon[43] with a phase shift at different values from -90 degrees. As we can see in Figure 3.6a, in the low frequency range, the phase part of the impedance goes to $\sim -80^0$, suggesting a non-ideal phase shift of the interface capacitance. A phenomenological constant phase element (CPE),[44–46] $Z_{CPE}=1/C_i(i\omega)^n$, is commonly used to substitute the

interface capacitance with adjustment of phase shift to a value of $-(90n)^0$. The parameter n describes the purity of the capacitance with range from 0 to 1. The overall impedance of the SWNT-electrolyte interface therefore can be formulated as:

$$Z_i = \frac{R_{ct}}{1 + C_i(i\omega)^n R_{ct}} \tag{3.5}$$

The in-plane impedance Z_n of the SWNT network along the TFT channel is gate potential dependent. Its resistance component R_n comes from the SWNTs' intrinsic resistance, cross-junction resistance, and the geometry of the networks (corresponding to the source-drain conductance measured previously). Besides the resistance component, the electrostatic coupling between SWNTs and SWNTs forms a capacitance C_n that is in parallel with the resistance. Since the sweep potential in the interfacial capacitance measurement is a small perturbation added on the gate potential, for a given gate potential E_g, the impedance of the SWNT network can be expressed as:

$$Z_n|_{E_g} = \frac{R_n}{1 + C_n\, i\, \omega\, R_n} \tag{3.6}$$

By combining the equations (3.4)(3.5)(3.6), the theoretical expression to model the impedance of SWNT-electrolyte interface is:

$$\mathrm{Z} = R_c + \sqrt{\frac{R_{ct}R_n}{(1 + (i\omega)^n C_i R_{ct})(1 + i\omega C_n R_n)}}\coth[L\sqrt{\frac{R_n(1 + (i\omega)^n C_i R_{ct})}{R_{ct} + i\omega C_n R_{ct} R_n}}] \tag{3.7}$$

where, R_c is added to represent the series resistances that include bulk solution resistance, the electrode contact resistance and the resistance of non-gated SWNTs covered under photoresist.

We performed a fit of equation (3.7) to the impedance spectrum data with the following as parameters (R_{ct}, C_i, R_n, C_n, n, R_c). The resultant fit describes the data well over the entire frequency spectrum as seen in Figure 3.6a. Using this fit, we can obtain a quantitative value for the components in the SWNT network system. These results are shown in Table 1.

Table 3.1: Total interfacial capacitance density, capacitance purity, charge transfer resistance-area, in-plane sheet capacitance and sheet resistance of the SWNT network, estimated by fitting the TL model to the experimental spectrum.

C_i ($fF/\mu m^2$)	n	R_{ct} ($M\Omega \cdot mm^2$)	C_n (pF/sq)	R_n ($M\Omega$/sq)	R_c ($M\Omega$)
11.5	0.9	247.5	1.7	39.8	4.3

The fitted in-plane resistance of SWNT network along the whole channel is 49.7 $M\Omega$, in good agreement with the DC-measured value a 40 $M\Omega$. The in-plane capacitance is small, as expected. The Faradic resistance (due to redox reactions with trace impurities in the electrolyte) is also high, as expected, and consistent with the DC measured "leakage current". The quality of the curve fit and the agreement with the DC data adds additional confidence when assessing the interfacial impedance. We find an estimated total interfacial capacitance is 11.5 $fF/\mu m^2$, comparable to but a more quantitative measure than the 10 Hz estimation provided above. This demonstrates the need to perform a more comprehensive measurement of the total impedance spectrum opposed to simply measuring the impedance at a single frequency. The EIS measurement yields an estimated capacitance per

length of 0.9 fF/μm at gate potential -0.7 V, consistent with the rough estimate from the 10 Hz capacitance, which neglected the transmission line effects discussed above.

We now discuss the low frequency limit (claimed as 10 Hz above) in more detail, and relate it to the transmission line impedance model. Since the charge-transfer resistance R_{ct} is significantly larger than the in-plane resistance R_n, in the on-state, the low frequency regime ($\omega \to 0$) leads to:

$$\lim_{\substack{\omega \to 0 \\ R_{ct} \gg R_n}} \frac{\partial Z}{\partial \omega} = \frac{\partial Z_{Randles}}{\partial \omega} \tag{3.8}$$

where $Z_{Randles}$ is the impedance of a Randles circuit model[19] containing a resistor in series with a parallel combination of a capacitor and a resistor. The overall impedance can be approximated to first order as a Randles circuit. Further simplification can be made when the charge transfer resistance is significantly larger than the capacitive impedance at the measurement frequency 10 Hz, *i.e.* $\omega C_i R_{ct} \gg 1$, such that the impact of the charge transfer resistance is insignificant. With all of the above assumptions, the transmission-line model can be approximated as a simple circuit model with the total interfacial capacitance in series with other resistive elements. This explains the good agreement between the 10 Hz measured capacitance and the more refined transmission line model measurement. As we can see in Figure 3.7, only in the on state (red curve) and low frequency range (below ~100 Hz), the capacitance spectrum shows less dependence on frequency. However, in the off state (blue curve), even at very low frequency, the capacitance value is still highly

dependent on the measurement frequency. Hence the calculated capacitance based on the simplified model can no longer represent the true capacitance.

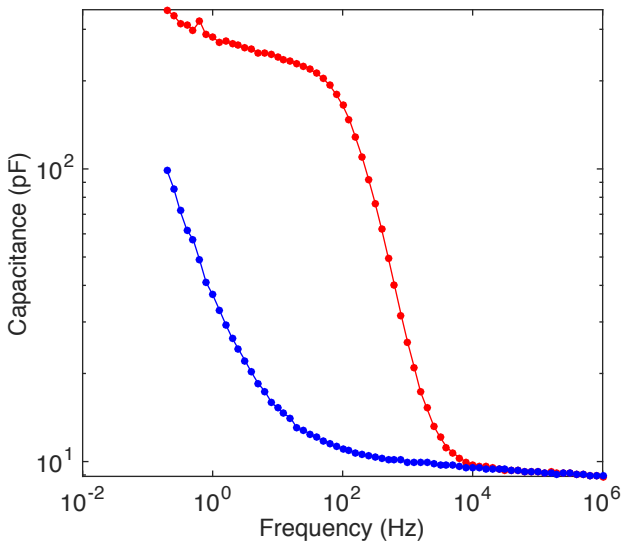

Figure 3.7: Capacitance vs. measurement frequency at on state (red) and off state (blue).

3.3.4 Quantum vs. electrochemical capacitance

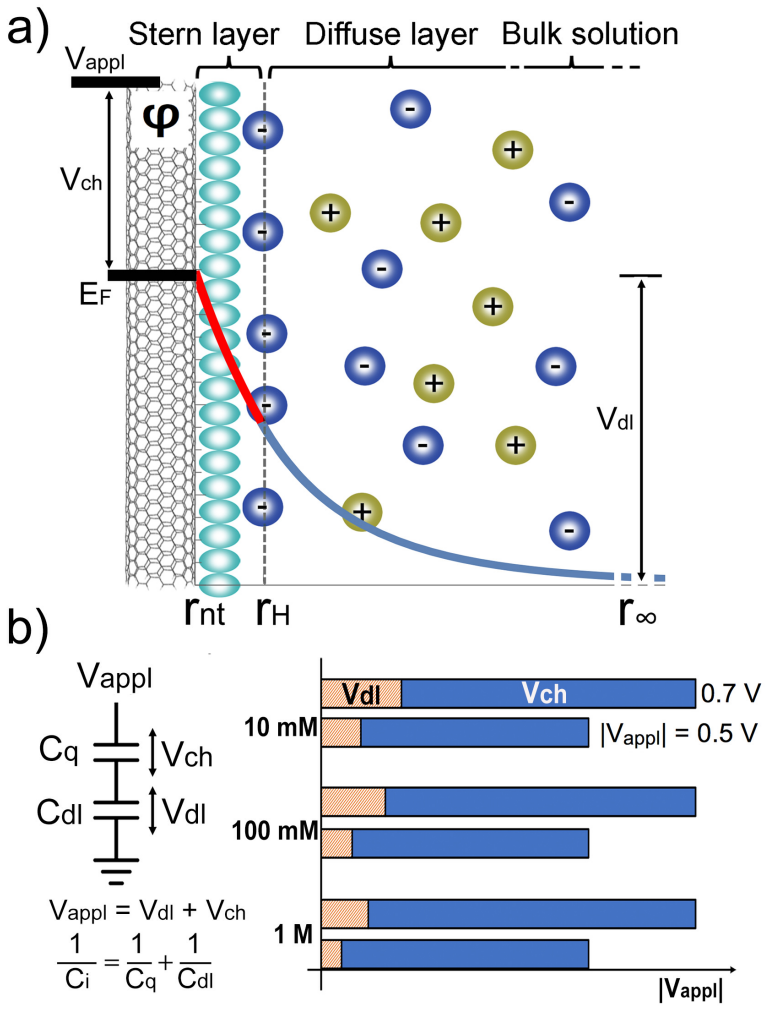

Figure 3.8: Potential drop across the SWNT-electrolyte interface. (a) Schematic of the double layer structure at the SWNT surface. The potential distribution along the radial direction consists of the chemical potential shift (Vch), followed the decay in the Stern layer (red), and the diffuse layer (blue). (b) The relative contribution of each potential drop (Vch and Vdl) to the total potential drop, which is equal to the applied potential (Vappl) at three different ionic strengths, 10 mM, 100 mM, and 1 M.

The measured capacitance between the SWNT network and the electrolyte comes from two physical properties: the finite density of states (DOS) of the SWNT and the double layer structure of the SWNT-electrolyte interface. These two types of capacitances come from two different physical mechanisms, and form the total interfacial capacitance in series (see circuit diagram in Figure 3.8), given by $1/C_i=1/C_q+1/C_{dl}$, with the smaller of the two

capacitances dominating the total capacitance.[42] The series capacitance model is an approximation which ignores the charge transfer effect and contact-induced band bending. This point is discussed in more detail below in the section "Series model approximation".

Now that we have measured the capacitance, we are in a position to determine: *Which capacitance dominates, the electrochemical (double layer) or the quantum capacitance?* In order to answer that question, we need more sophisticated models of each capacitance, which we develop in detail below. In general, the applied voltage (V_{appl}) will be divided unevenly between the two capacitances. Furthermore, each capacitance contribution is dependent on the potential drop across that particular capacitor, *i.e.*, the value of C_{dl} depends on the potential drop across C_{dl}. Similarly, the value of C_q depends (and only depends) on the potential drop across C_q which we call V_{ch} (the change of chemical potential). However, the way in which the total voltage is divided depends on the values of the individual capacitances, so they must all be determined self-consistently, once a suitable model for $C_{dl}(V_{dl})$ and $C_q(V_{ch})$ is determined. This is further complicated because C_{dl} depends also on ionic strength, whereas C_q is not expected to depend on ionic strength.

The detailed models for $C_{dl}(V_{dl})$ and $C_q(V_{ch})$ are presented below in turn. For now, we summarize the results of these findings in Figure 3.8, which shows the relative potential drop across each component at three different ionic concentrations. Two conclusions can be drawn from this. First, the potential is mostly dropped across the V_{ch} in all configurations. This indicates that the quantum capacitance actually dominates in most cases. Second, V_{ch} varies as the ionic concentration changes. As a result, the quantum

capacitance has an indirect dependence on the ionic concentration. We now turn to a detailed discussion of each component.

3.3.5 Double layer model of a SWNT

In this section, we model the double layer for the case of a carbon nanotube geometry based on the GCS model using a modified Poisson-Boltzmann (PB) equation. Initial models in the cylindrical geometry have taken into account the effect of small radius of curvature on the diffuse capacitance of carbon nanotubes and monoatomic wires,[14,47] but the ion size, correlation, Stern layer thickness and close packing issues were not incorporated, which we find is a critical effect to include in order to provide a realistic model for our data. We are particularly interested in extracting the voltage dependence of the double layer capacitance (ie. $C_{dl}(V_{dl})$), as well as the effect of ionic strength.

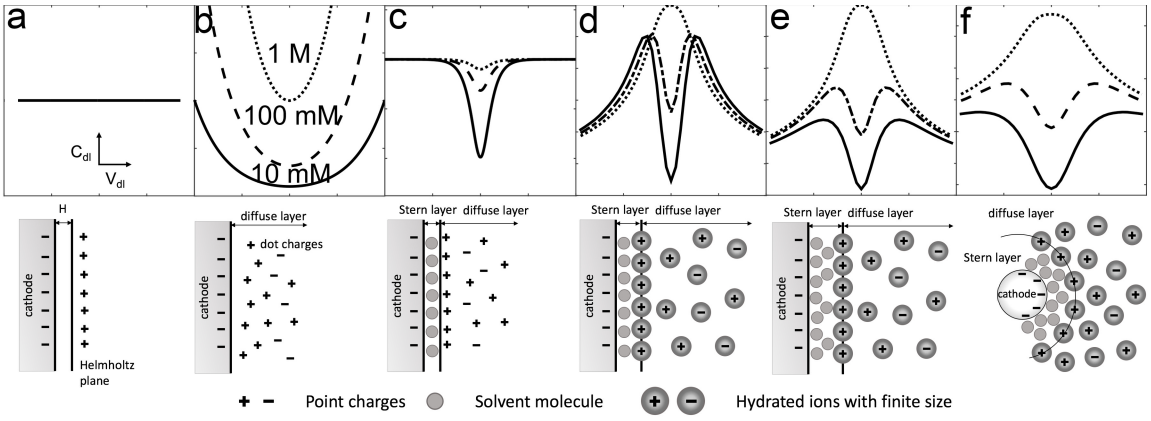

Figure 3.9: Evolution of the electric double layer models. Top panel: capacitance vs. potential $C_{dl}(V_{dl})$ at different ionic concentrations. Bottom panel: the arrangement of solvated ions near the interface. (a) Helmholtz model, (b) Gouy-Chapman model, (c) Gouy-Chapman-Stern (GCS) model, (d) GCS model with the effect of ion size, (e) including the effect of varied Stern layer thickness, (f) applied to SWNT nano-electrode with extreme curvature.

The electric double layer of the electrode-electrolyte interface was first modeled by Helmholtz as a two-plate capacitor, with the metal electrode and electrolyte electrode separated by a certain distance caused by finite ion size (Figure 3.9a). Gouy and Chapman improved the model by considering the electrolyte side as the diffusive structure of counter-ions loosely accumulated to the metal electrode surface (Figure 3.9b). Later, Stern combined the Helmholtz model and Gouy-Chapman model, and described the double layer as two capacitances in series: the Helmholtz's plate capacitance in series with the Gouy-Chapman's diffuse capacitance (Figure 3.9c).[19] The Gouy-Chapman-Stern (GCS) model has become the popular model for the electric double layer. Modern electrochemistry theories still use the GCS model as a framework but include more effects such as the finite ion size and short-range correlations to approach the real system. The Poisson-Boltzmann (PB) equation (Debye–Hückel theory) and the mean sphere approximation (MSA) are two popular approaches adapted to calculate the properties of realistic electrolyte systems.[20,21] The original PB methods treat ions as point charges in a continuous dielectric medium and ignore the short-range correlation of ions, which provides a limiting prediction, valid at low concentrations. MSA overcomes this limitation being able to work well in strong electrolytes, by modeling ions as hard charges spheres in a continuous medium, and includes the correlation effect. Modified PB methods (used in this paper) can also account for the effect of non-zero ion size and close-range correlation, which is easier to compute and can provide approximately the same level of accuracy as MSA. More advanced methods such as classical molecular dynamics (MD) simulations and DFT-based *ab initio* MD simulations,[15,22,23] which treat the medium as discrete molecules with realistic

intermolecular correlations, provide a more detailed model for the system, especially for multivalent molecules. However, MD methods require large computational power.

The effect of finite ion size and the effect of Stern layer thickness on the GCS model creates a more complex $C_{dl}(V_{dl})$ curve, as shown in Figure 3.9 d and e. While these effects have been well studied in ref. [13,25,48], and the resultant prediction is qualitatively different from that of GCS model, they are usually neglected under limited conditions when the curvature of electrode is small, ionic concentration is low and electrode surface potential is low. However, here in the case of a carbon nanotube, none of above conditions are valid, hence all these three effects must be taken into account. In addition, SWNTs have cylindrical geometry with extreme convex surface, the geometrical effect provides larger diffusion space and adds quantitative distinction to the final results such as the change of slope in the decreasing trend of the diffusion capacitance at high electrode surface potential, indicated schematically in Figure 3.9f. We now turn to our detailed model for the nanotube electrolyte capacitance which includes all those effects.

Figure 3.8a shows the double layer structure based on the Gouy-Chapman-Stern (GCS) model.[19,24] Near the surface of the charged SWNT electrode, electrostatic interactions cause counter-ions to accumulate to the surface of the electrode, forming a compact Stern layer and a loose diffuse layer. In the Stern layer, the compacted layer of counter-ions strongly attaches to the electrode surface with solvent molecules between them. The solvent molecule can be considered as the hydration shell of the electrode, whose thickness changes according to ionic concentration. In the diffuse layer, free ions with thermally activated movement loosely accumulate near the Stern layer under the influence of

electrostatic force. The accumulation of counter-ions in these two layers electrically screens the electrode surface, resulting in electric potential decaying exponentially to zero from the surface to the bulk solution.

Ionic species in the solution are governed by motion dynamics that has a coupled influence from diffusion and electrostatic forces. This behavior can be described by Convection–diffusion equation together with Poisson's equation. From these two equations, and considering both equilibrium state and binary symmetric electrolytes, the potential distribution can be accounted for by the original Poisson-Boltzmann equation:[19]

$$\nabla \cdot (\varepsilon_r \varepsilon_0 \nabla \varphi) = 2\rho_q \sinh\left(\frac{q\varphi}{k_B T}\right) \tag{3.9}$$

where φ is the electric potential distribution in space, $\rho_q = q \cdot N_A \cdot c_0$ the charge density of cation or anion in a symmetric electrolyte solution, c_0 the molar concentration of ion species, N_A Avogadro constant, and $q = z \cdot e$ is the charge of the ions with valence z and the electron charge e.

A modification of the Poisson-Boltzmann can be made to account for the short-range correlation:[49]

$$\nabla \cdot (\varepsilon_r \varepsilon_0 \nabla \varphi) = 2\rho_q \sinh\left(\alpha \cdot \frac{q\varphi}{k_B T}\right) \tag{3.10}$$

which only defers from the original PB equation by rescaling the potential dependence with the correlation parameter α.

For a planar electrode, there is an analytic solution for the Poisson-Boltzmann equation, which can give the double layer capacitance,[19]

$$\begin{aligned}\frac{1}{C_{dl}} &= \frac{1}{C_{Stern}} + \frac{1}{C_{diffuse}} \\ &= \frac{d_s}{\varepsilon_r \varepsilon_0} + \frac{1}{(2\varepsilon_r \varepsilon_0 z e \rho_q \alpha / k_B T)^{1/2} \cosh\left(z e \varphi_H \alpha / 2 k_B T\right)}\end{aligned} \tag{3.11}$$

where C_{Stern} is the capacitance of the Stern layer, $C_{diffuse}$ the capacitance of the diffuse layer, d_s the thickness of the Stern layer, and φ_H the potential at the outer Helmholtz plane (r=r_H plane in Figure 3.8a).

For a SWNT electrode, one can treat it as a solid cylindrical electrode, and estimate the double layer capacitance by solving the Poisson-Boltzmann equation numerically in cylindrical coordinates. Though the inner tubular pore of a nanotube also stores charges,[50–56] we ignore this part because the *differential* capacitance of it is small due to narrow confinement and vanishes over a threshold gating potential.[32] The differential capacitance is small because, once the inner portion of the nanotube is filled up with ionic charge, it is "full", and adding additional voltage will not increase the charge. A calculation of diffuse layer capacitance only (neglecting the Stern layer) of carbon nanotube has been reported in ref. [14]. However, as we will see below, the Stern layer is non-trivial, and cannot be neglected in this calculation. In the case of high ionic concentration and high electrode potential, additional assumptions are necessary in order to account for the effect of finite ion size and Stern layer thickness.

A 2nd modification of the Poisson-Boltzmann equation[13,57,58] can be made to account for the finite ion size by setting a maximum limit of the local ion density, and for the Stern layer by setting a plane where charged ions cannot pass through. The Stern layer thickness is chosen according to ionic concentrations, based on hydrated ion radius and reported experiment data.[25,59] For the cylindrical geometry of SWNTs, the modified model can be expressed below,[13,60]

$$\frac{1}{r}\frac{d}{dr}\left(\varepsilon_r\varepsilon_0 r\frac{d}{dr}\right)\varphi = \begin{cases} 0, & r_{nt} \le r \le r_H \\ \dfrac{2\rho_q \sinh\left(\alpha\dfrac{q\varphi}{k_B T}\right)}{1+2v\sinh^2\left(\alpha\dfrac{q\varphi}{2k_B T}\right)}, & r \ge r_H \end{cases} \tag{3.12}$$

where the additional parameters is ν, the packing parameter[13,60] defined as $\nu = 2a^3 \cdot N_A \cdot c_\infty = 2c_\infty / c_{max}$, related to the ratio between the ionic concentration in bulk solution and the local maximum ionic concentration. Within the Stern layer ($r_{nt}<r<r_H$), there is no free charge distribution; the Poisson equation is set to zero. The potential at the electrode surface is the applied potential φ_0, and the potential in the bulk solution decays to zero. Potential and electric force should be continuous at the outer Helmholtz plane (considering a constant electric permittivity). These give us a list of boundary conditions: $\varphi(r=r_{nt})=\varphi_0$, $\varphi(r=+\infty)=0$, $E_{r1-}=E_{r1+}$, $\varphi_{r1-}=\varphi_{r1+}$.

To solve equation 3.12, the essential parameters are chosen to best characterize the present experiment: $T = 298\ K$, electric permittivity $\varepsilon_r=80.2$ for water at room temperature, effective hydrated ion radius[59] of Cl- and K+ $r_{ion}=0.33nm$, the mean van der Waals distance between water molecules $d_w=0.31nm$, the Stern layer thickness $d_s=0.9nm,\ 0.62\ nm$ for electrolyte concentration at 1 mM and 10 mM, and reaches the limit of ion's hydrated

radius at higher concentrations,[19,25] the average SWNT's radius r_{nt}=0.7nm. The correlation parameter α is estimated to be 0.9997 according to the definition in ref.[49], showing a minor correlation effect (α=1 means no correlation effect). Using these numerical values and the boundary conditions, COMSOL 5.1 is applied to solve equation 3.12 at various applied potentials and ionic concentrations. The resulting potential distribution along the radial direction of SWNT exponentially decays from the SWNT surface to the bulk solution as expected. The Debye screening length varies from 1 nm to 10 nm dependent on the electrode potential and electrolyte concentrations. From the potential distribution, the electrically stored charge q^{SWNT} in SWNT can be calculated. According to Gauss's law, the accumulated net charge in the screening layers is,

$$q^{screen} = \varepsilon\varepsilon_0 \oiint_{\substack{Gauss \\ Surface}} \vec{E} \cdot \overrightarrow{dS} = \varepsilon\varepsilon_0 (2\pi r_1 L) \frac{\partial \varphi}{\partial r}|_{r=r_1} \tag{3.13}$$

where L is the length of the electrode. Screening charge counter-balances the net charge in the electrode, so q^{SWNT}=-q^{screen}. Therefore, we can calculate the differential capacitance of the double layer: C_{dl}=$dq^{SWNT}/d\varphi_0$. Here φ_0 is the same as the potential V_{dl} in Figure 3.8.

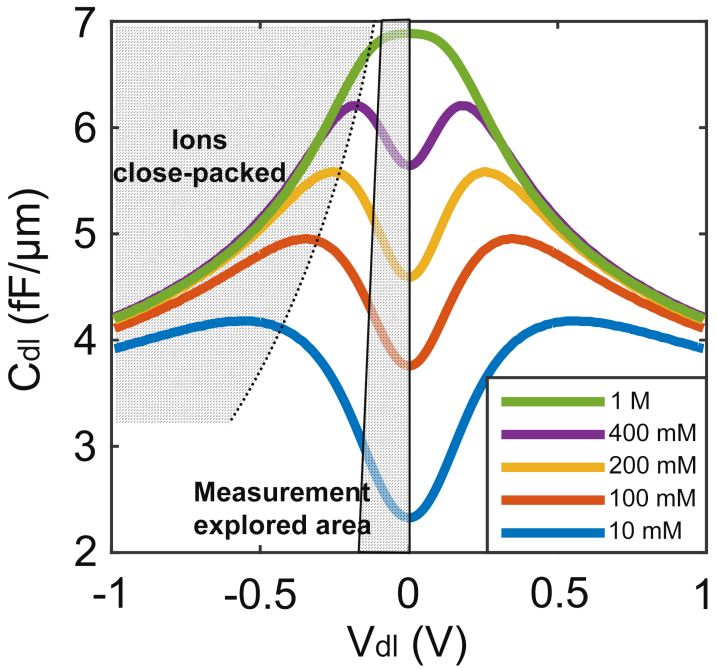

Figure 3.10: Double layer capacitance of a SWNT as a function of surface potential and ionic concentration. Ions are close-packed near the SWNT when either the surface potential or the ionic concentration is high (top left grey area). The measurement here only covers the double layer capacitance in a low potential range (middle grey area), due to the domination of quantum capacitance.

The resulting double layer capacitance of SWNTs as a function of the electrode potential is shown in Figure 3.10. It is symmetric since we used a binary symmetric electrolyte with similar hydrated radius of cations and anions. The close-packing configuration of ions happens at high surface potential or high ionic concentration. As the surface potential increases, the double layer capacitance first increases and then decreases. The change of trend happens at a point where ions are close-packed near the electrode surface. Before reaching the close packing point, the increasing electric field will compact the Stern layer and diffuse layers to make the double layer thinner, which increases the double layer capacitance. Continuing increasing the electric field beyond the close-packing point, instead of getting thinner, the Stern layer and diffuse layer get crowded and grow quickly in thickness (ions are close-packed). Inversely proportional to the thickness, the double layer

capacitance starts to decrease. This change of trend happens earlier in higher ionic concentration and eventually vanishes and only the decrease trend shows (*e.g.* the 1M case in Figure 3.10). The decrease trend will softly level off and the double layer capacitance becomes independent of ionic concentration, which happens as the growth of double layer in thickness balances with the growth of the ion-packed electrode in surface area. Ion distribution near electrode surface is the result of balanced forces caused by potential gradient and concentration gradients, hence changing ionic concentration should have a similar effect as changing electrode surface potential. Close-packing of ions can happen at high ionic concentration, even when the surface potential is low.

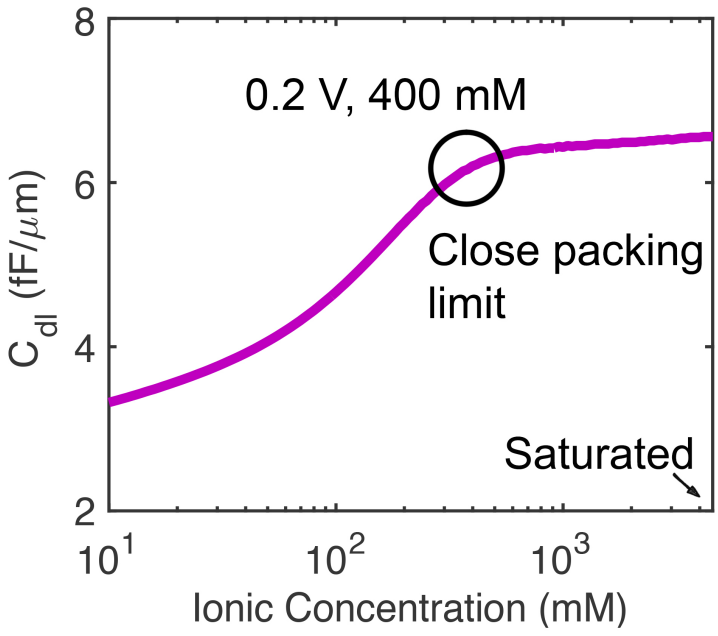

Figure 3.11: Double layer capacitance as a function of ionic concentration. The capacitance reaches close-packing limit at ionic concentration ~400 mM and surface potential 0.2 V.

Increasing ionic concentration has a similar effect on the C_{dl} as increasing surface potential. As shown in Figure 3.11, the C_{dl} first increases and then reaches a limit when ions start close-packing. However due to the extreme convex curvature of SWNTs, there is more

space for ion diffusion per surface area than planar electrode. Hence ion close-packing happens in higher surface potential or higher ionic concentration.

Although we explored the SWNT-to-electrolyte capacitance over a wide range of applied potential -0.7 V ~ 0.4 V, the potential drop on the double layer during the measurement is within a small range as shown in the middle grey area in Figure 3.10. A majority of the applied potential is on the change of chemical potential of SWNTs. Hence, in the limited window of measurement, we did not reach the close-packing condition of ions. In the calculation, we used the hydrated ion size as the minimum distance between ions, however the distance can be larger due to the dielectrophoretic repulsion of ions.[48] In this case, C_{dl} can start to decrease at smaller surface potential. A strong electric field has influence on the dielectric constant of the Stern layer.[13] When the electric field is larger than ~ 25V/nm, the field dependent dielectric constant of Stern layer need to be considered for more accurate estimation.[61]

3.3.6 Quantum capacitance

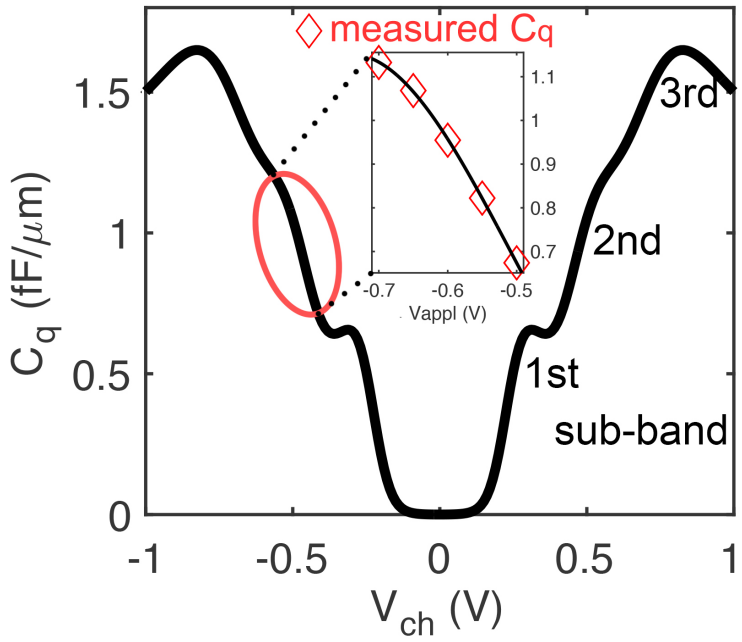

Figure 3.12: Ensemble averaged quantum capacitance as a function of the change of chemical potential. Ions with close interaction with SWNT can effectively gate SWNT and change its quantum capacitance. The inset curve is the measured quantum capacitance as a function of the liquid gate potential. It fits well with the 1st and 2nd sub-band of quantum capacitance, considering a shift of V_{ch} due to the choice of reference electrode.

Although the quantum capacitance has been studied in a dry environment[37] and the principles are well-understood, it is important to develop a model for our particular nanotube diameter distribution and voltage range to adequately ascertain its contribution to the total capacitance in a liquid electrolyte environment, which has not (until now) been measured. We now perform such a calculation.

The quantum capacitance originating from the finite density of states (DOS) of SWNTs is on the order of $C_q^0=4e^2/\pi\hbar v_F\approx 0.4fF/\mu m$ for one sub band occupied.[36] In the case of higher chemical potential with the second sub band occupied, this value can be larger. Here, in the configuration of electrolyte gating, ions closely interacting with SWNTs can very effectively

shift the chemical potential of SWNTs. We expect ~ 1 fF/ μm will hold in the case of electrolyte gated SWNTs. Ref. [37] has measured the quantum capacitance of a SiO_x-gated SWNT in dry environment. In both cases, the measured total capacitance contains two capacitances in series: the gate capacitance (C_{gate}) and the carbon nanotube intrinsic quantum capacitance (C_q). The total capacitance takes the form, $1/C_{total}=1/C_{gate}+1/C_q$. The main difference between our work and the reference work is in the term, C_{gate}. In the reference work, C_{gate} is determined by the geometry and dielectric constant of the oxide layer between the gate electrode and the carbon nanotube, which is a constant value of 61.5 aF/μm. However, in our case, C_{gate} is the double layer capacitance, which is a non-trivial function of the surface potential and ionic strength. This term has not been thoroughly studied in the case of nanoscale 1d nanotube, and presents a major difference in the capacitance measurement. Despite the difference on C_{gate}, the intrinsic C_q should be the same for both cases. The reference work presents the capacitance data (C_{nt}) only as a total quantity, and does not give directly, C_q. However, from the given value of the gate capacitance, 61.5 aF/μm, and the g-parameter (which is the square root of the ratio between the total capacitance and quantum capacitance), ~ 0.26 - 0.34, we can calculate C_q, which yields a value ranging ~ 0.5 - 0.8 fF/μm for the 1st sub-band. This value should be expected to be larger in the 2nd sub-band. Our work measures C_q over both the 1st and 2nd sub-band and gives value of ~ 0.67 - 1.16 fF/μm, showing agreement with the referenced work.

Theory of ensemble averaged quantum capacitance

For quantum capacitance of individual semiconducting SWNTs, its value as a function of chemical potential and tube diameter is given by[37, 62]

$$C_q(\mu, \mathrm{d}) = \int_{subband} dE \cdot F_T(E-\mu) \cdot C_q^0 \sum_{j=-3}^{3} (1-(E_j/E)^2)^{-1/2} \tag{3.14}$$

$$E_j = \hbar v_F \frac{2j}{3\mathrm{d}}$$

where, $F_T(E) = (4k_BT)^{-1}\mathrm{sech}^2(E/2k_BT)$ is thermal broadening function, k_B is Boltzmann constant, T is temperature, v_F is the Fermi velocity, and we included the first three electron and hole sub-bands.

Since our experiments consist of a heterogeneous mixture of nanotube diameters and lengths, we model this as an effective, ensemble average capacitance, which depends only on the average chemical potential of all the nanotubes.

$$C_q(\mu) = \int d\mathrm{d} \cdot \mathcal{N}(\mathrm{d}_0, \Delta\mathrm{d}) \cdot C_q(\mu, d) \tag{3.15}$$

The mean diameter of the SWNTs we used is 1.4 nm and it varies in the range of 1.2 - 1.7 nm. We assume a Gaussian distribution (mean at 1.4 nm and deviation at 0.25 nm) to represent the diameter distribution of the SWNTs within the network. From that, we can estimate the ensemble averaged quantum capacitance of a mixed nanotubes. Figure 3.12 shows the theoretical average quantum capacitance as a function of the chemical potential. Because of the relatively high homogeneity of SWNTs we used, in the calculated Cq curve,

we can still see the sub-band structures. For wider range of diameter distribution such as 1-3 nm, the sub-band information will be averaged out and the Cq curve will be simply "V" shape.

Limitation of measurement window

Compared to the theoretical value, the measured quantum capacitance resides in part of the 1st and 2nd sub-band (red region in Figure 3.12), corresponding to the applied gate potential – (0.7 ~ 0.5) V. The reason we address the capacitance within the limited potential window is that, as potential goes more positive (V_{appl} > -0.5V), the conductance of SWNTs drops exponentially. As shown in the conductance curve (Figure 3.2), -0.5 V is already in the grey area between the conductive and nonconductive states. With more and more SWNTs disappearing from the measurement circuit, the fraction of SWNTs that contribute to the impedance signal can no longer be determined. Another perspective to verify this is to measure the linearity of the relationship between the measured capacitance and the channel area of SWNT network. In the inset of Figure 3.3b, when the applied potential goes to - 0.5 V, we can see the measurement points start to deviate from the linear relationship. On the other hand, as the potential goes more negative (V_{appl} < -0.7V), redox reaction of electrolyte species will occur and cause a permanent change of the system.

Dependence of C_q on V_{ch}

The measured capacitance consists not only the quantum capacitance, but also the double layer capacitance in series. In order to compare it with the pure quantum capacitance estimated from the theoretical model, we need to separately determine the

quantum components from the measured total capacitance. The calculation of the double layer capacitance will show that at high ionic strength (*e.g.* 1 M), the double layer capacitance is large and one order of magnitude higher than the quantum capacitance, thus quantum capacitance will be the dominating part of the measured value and double layer part can be neglected, similar to the case of graphene.[38,63] The inset of Figure 3.12 shows the measured capacitance as a function of the applied potential, which agrees with the theory curve. Note that, at low ionic strength, the double layer capacitance is smaller and cannot be neglected due to its comparable value to the quantum capacitance, hence the measured total capacitance cannot represent the quantum capacitance.

3.3.7 Quantitative determination of both quantum and electrochemical capacitances

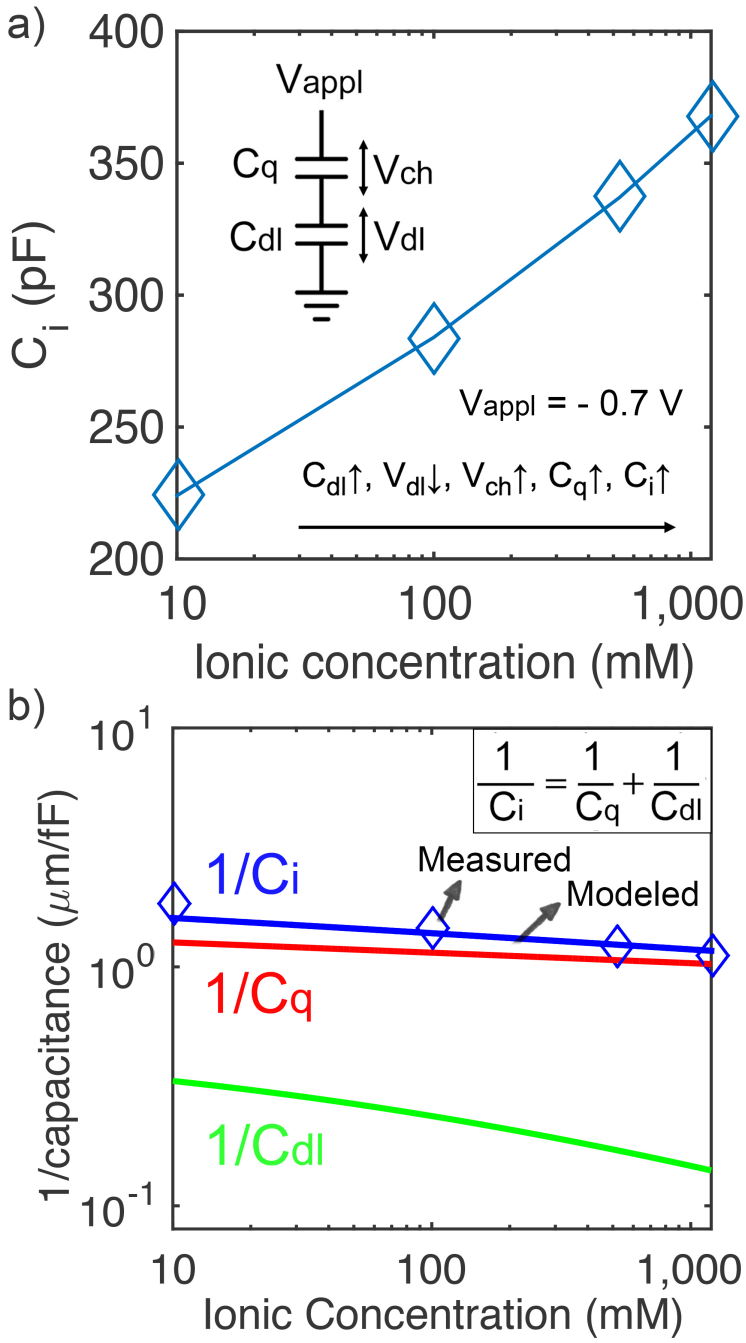

Figure 3.13: Total interfacial capacitance changes with ionic concentration, caused by potential re-distribution between the two types of capacitance. (a) The measured total capacitance of SWNT-electrolyte interface and (b) the modeled total capacitance that includes the quantum capacitance and double layer capacitance.

Now that we have quantitative models for both $C_{dl}(V_{dl})$ and $C_q(V_{ch})$, we can determine the values of V_{dl} and V_{ch} for a given V_{appl} at different electrolyte concentrations. As mentioned above, this determination is done self-consistently using numerical methods. The results are summarized in Figure 3.13.

It is generally known that the double layer capacitance depends on electrolyte concentration, since the Debye screening length changes with the electrolyte concentration.[19] The quantum capacitance, on the other hand, being a property only of the intrinsic density of states, is expected to depend only on the Fermi level, and not the external ionic strength. With this motivation in mind, we measured the ionic strength dependence of the total capacitance.

Figure 3.13a shows the measured total capacitance of the SWNT-electrolyte interface as a function of the ionic concentration under conditions where the nanotube network is clearly in the "on state" (gate potential at -0.7 V). As expected, the data clearly shows a trend of increasing total capacitance with increasing ionic strength: As the ionic strength increases, the Debye length decreases, increasing the double layer capacitance. The prediction in Figure 3.13b takes into account the modeled double layer capacitance, its dependence on ionic concentration, and its dependence on electrical potential. The applied potential is dropped across both the quantum capacitance and the double layer capacitance. Therefore, for a given applied potential V_{appl}, as the electrolyte concentration changes, the division of V_{appl} between V_{dl} and V_{ch} (Figure 3.8) changes since the value of C_{dl} changes. For this reason, even for a fixed V_{appl}, V_{ch} changes with ionic strength and therefore the Fermi energy of the electrons in the nanotubes (which depends on V_{ch})

changes, and so does C_q. (C_q is not changing directly as a consequence of the change in the ionic strength.) Therefore, to model the total capacitance at a given bias voltage (as is measured in Figure 3.8b), it is necessary to self-consistently solve for the total capacitance numerically. Our model, using the experimentally applied voltage in the nanotube on state, reproduces the ionic concentration dependence well.

3.3.8 Capacitance of graphene

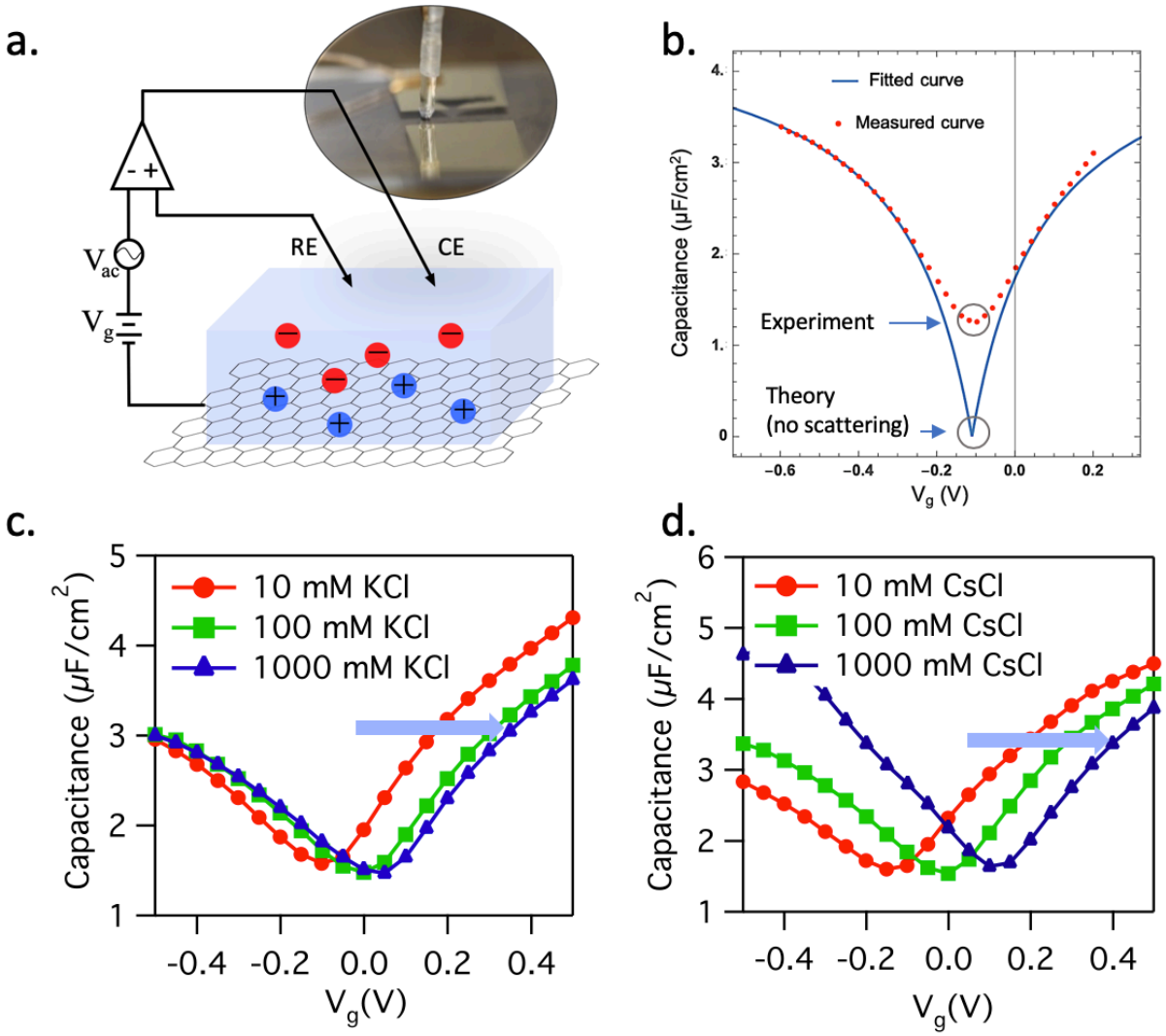

Figure 3.14: Capacitance measurement of graphene. (a) Schematic of the measurement setup. A graphene sheet is liquid-gated using three electrode configuration and the gate capacitance is measured. (b) The measured capacitance vs. gate voltage (red dots) and the fitted theoretical curve

(blue curve). (c) The capacitance vs. gate voltage in different ionic concentration in KCl solution, and in CsCl solution (d).

We conducted the same measurement on graphene for comparison. We measure the electrochemical impedance spectrum (EIS) between the electrolyte and the graphene and calculate the interfacial capacitance. The impedance of the device is measured over the frequency range of $10^{-2} \sim 10^{4}$ Hz, with 7 points per decade. Figure 3.15 presents a typical electrochemical impedance measurement of graphene in 100 mM KCl. The black line is measured data and red line is fitted data using a simple Randle circuit model. The graphene capacitance is ~2 μF/cm^2 that was measured in 100 mM KCl. We also measured the voltage dependent capacitance in different concentrations using the same device. The results are presented in the bottom panel of Figure 3.14.

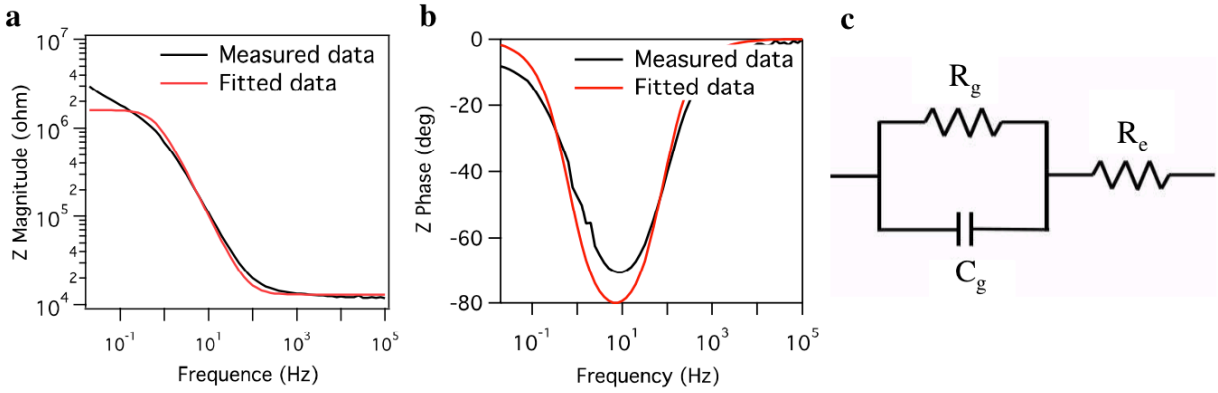

Figure 3.15: The electrochemical impedance spectrum (EIS) between the electrolyte and the graphene (a, b), and the Randle circuit model.

The theoretical expression of the quantum capacitance for graphene is,[38]

$$C_q = \frac{2e^2}{\hbar v_F \sqrt{\pi}} (|n_G| + |n^*|)^{1/2} \qquad (3.16)$$

where n_G and n^* are the carrier concentration induced by the gating V_g and the defects/impurities.

$$n_G = (\frac{eV_{ch}}{\hbar v_F \sqrt{\pi}})^2 \quad (3.17)$$

Assuming a constant capacitance value (20 μF/cm^{-2}) for the double layer, the total capacitance can be calculated based on $C_{tot}^{-1} = C_q^{-1} + C_{dl}^{-1}$. By fitting the measured capacitance with the theoretical model (Figure 3.14b), we estimated the impurity concentration of ~ 10^{12} cm^{-2}.

3.3.9 Series model approximation

We used a series model to account for the relationship between the quantum capacitance and the double layer capacitance. This essentially assumes the interaction between the electrolyte and the nanotube is purely electrostatic, and that the quantum wave functions do not significantly overlap. We now discuss the justification for this model in more detail. First, there is a possibility of charge transfer between the nanotube-electrolyte interface. However, our measurements show this Faradaic current to be negligible. Second, mismatches between the nanotube work function and the electrolyte and reference electrode work functions result simply in an offset to the applied potential. Third, we treat the effect of molecular adsorption as a constant offset to the total applied potential. With all the above assumptions, we can model the total capacitance as $1/C_i = 1/C_q + 1/C_{dl}$. Hence, the combination of the two types of capacitance can be simplified in a series relationship with the smaller one dominating the total capacitance[42] (Figure 3.8). A

similar case was studied on graphite/ionic liquid system, where the electronic state of the electrode plays a role in the total interfacial capacitance, and the two types of capacitance are combined in series relationship.[64]

3.3.10 Charge storage in nanopores vs. nanowires

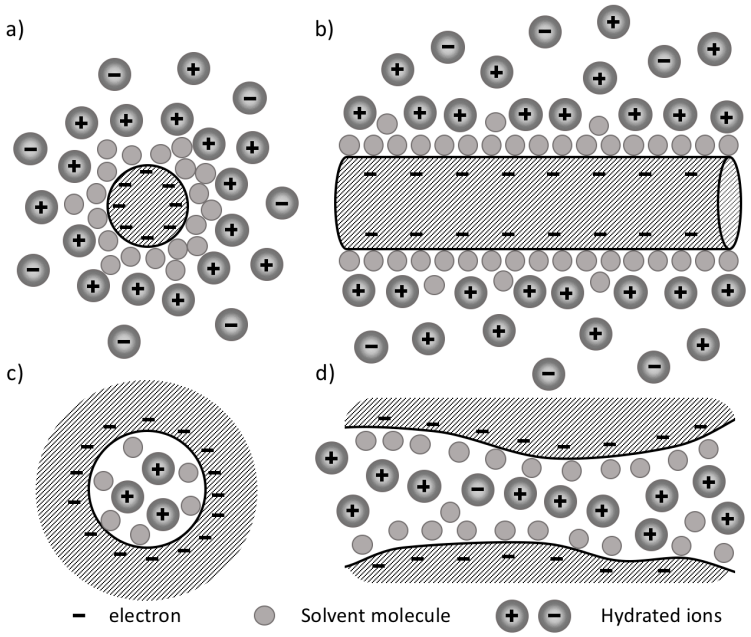

Figure 3.16: Cartoon diagram showing the different mechanism of charge storage outside the surface of a solid cylindrical electrode (a, b) and inside a ultranarrow pore (c, d)

The diagram in Figure 3.16 is to further clarify the case of our study (a, b) vs nanopore case (c, d). Our sample contains an ultrathin layer of carbon nanotubes sparsely deposited on a flat substrate. The SEM characterization shows that the average nanotube density is ~ 12.6/μm^2, which means the average distance between nanotube is large (~ 100 nm) in the substrate plane and no confinement above the plane. Hence the confinement effect can be ignored. Although the nanotubular pore inside a nanotube can contribute to the total capacitance, this part can also be neglected in the case of our study (nanotube gated at

around 0.5 V), because the differential capacitance of the narrow tubular pore is small and vanishes over a threshold potential. The differential capacitance is small because, once the inner portion of the nanotube is filled up with ionic charge, it is "full", and adding additional voltage will not increase the charge.

We turn our attention now to comparison to prior work on small electrodes. In contrast to planar electrodes and ultramicroelectrodes (UMEs), which have been studied both analytically and experimentally in previous work,[19] the total interfacial capacitance of carbon nanotube based electrodes shows qualitatively different behavior arising from the intrinsic quantum capacitance and the geometries of electrodes with extreme curvature and small dimensions. Although the quantum capacitance of individual SWNTs has been evaluated in a dry environment;[37] and the double layer capacitance in ionic liquid has been simulated using classical molecular dynamics,[15] this work represents a comprehensive modeling and measurement of these effects in an electrolyte environment. As far as prior experimental data, the total capacitances of carbon nanotube papers (CNPs) or bulky carbon nanotubes have been measured per gram in previous works,[35,65] however the capacitance properties of SWNTs were not quantitatively assessed. Heller and co-workers have studied the charge-transfer at the SWNT-electrolyte interface as a function of band alignment.[42] Our work studies the charge storage instead of charge transfer at the interface. This work provides a comprehensive model of the double layer capacitance of a long, narrow wire. Although it is being applied to the case of carbon nanotubes, it should apply to any long, narrow wire geometry, a case more and more common in modern research on electrochemistry.

3.3.11 Conclusion

We developed experimental methods and comprehensive models to investigate SWNT-electrolyte total interfacial capacitance, including the quantum capacitance and electric double layer capacitance. The measured overall interfacial capacitance is a combination of two types of capacitance in series: 0.67-1.13 fF/μm for quantum capacitance and 2.3-6.8 fF/μm for double layer capacitance depending on the ionic concentration and applied potential. The obtained quantum capacitance is in consistence with theoretical prediction for SWNTs as well as capacitance measurements in dry environment. SWNTs have critical dimension comparable to ion size. Its double layer capacitance appears quite different from conventional macroscale electrodes. Even though the double layer capacitance of SWNTs is larger than the quantum capacitance, and in many case, it can be one order of magnitude larger, the role of double layer capacitance cannot be neglected. Its sensitivity to ionic concentration can in fact shift the potential distribution across the interface and affects the quantum capacitance. The next logical step to improve on our knowledge and model of the SWNT-electrolyte interface would be to measure directly the impedance of a single nanotube-solution interface. Although a much more challenging to measure as quantitatively as we have here, such a measurement would provide more comprehensive data on which to based models and theories such as diameter and chirality dependence.

3.4 Methods

SWNT networks were obtained by vacuum filtration of 99.9% purity semiconducting single-walled nanotube ink onto mixed cellulose membrane with 25 nm pore size (MF-

Millipore VSWP04700). 600 µl of SWNT ink (IsoNanotubes-S 99.9%, diluted in DI water to a concentration of 1 µg/ml) was filtered through the membrane resulting in a uniform coated SWNT network film. Followed by 200 ml DI water rinse to remove residual surfactant, a SWNT network film on mixed cellulose membrane was made and stored for transfer. Soda lime glass was used as the substrate and treated with hot Piranha for 40 minutes at 140°C to achieve a clean surface. Pre-made SWNT network films were then moistened with ethanol and placed in contact with the cleaned substrate. After one-hour immersion of the device in acetone vapor, most of the mixed cellulose membrane was dissolved and the SWNT network was bonded to the substrate. The residual cellulose was removed in acetone and methanol step by step under carefully tuned conditions (30 minutes in 60°C acetone with stir speed 60 rpm and 20 minutes in methanol at 60°C with stir speed 60 rpm). After IPA rinse and N2 gas blow-dry, a large-area uniform SWNT network on glass substrates was made. Device arrays with various channel lengths were then patterned on the SWNT network by a standard photolithography. Ti (2 nm)/Pd (20 nm)/Au (50 nm) were deposited by e-beam evaporation, followed by a lift-off process to form contact electrodes. Oxygen plasma etching was used to constrain the SWNT network within the rectangular channel region between the source electrode and drain electrode. The final step of photolithography was used to open windows in the channel region, leaving the electrodes protected under photoresist polymer and SWNT network exposed.

A PDMS reservoir was then aligned on the device array for delivering aqueous solution. An electrochemical gate potential was applied to the SWNTs with respect to an Ag/AgCl reference electrode that is immersed inside the reservoir, controlled by a potentiostat (Gamry Reference 600). A counter electrode made of platinum was also immersed in the

reservoir to form a three-electrode configuration in order to control the liquid gate potential precisely. The potentiostat can apply an AC perturbation at various frequencies superimposed onto the gate potential and monitor the corresponding AC current, from which the electrochemical impedance spectroscopy (EIS) was determined. The source-drain conductance was measured by a source/measure unit (Keysight B2902A) previous to the EIS measurement to eliminate non-conducting devices. During the measurements, the devices were shielded in a Faraday cage to minimize background noise.

Chapter 4: Capacitance Study down to a Single Nanotube level Enabled by an Integrated On-Chip Shield

4.1 Introduction

One of the most fundamental properties of the interface between matter and liquid is the capacitance of that interface. The capacitance governs the ability to carry charge, and therefore determines the final fate of any electrical currents flowing through that interface. In biological systems, the capacitance directly affects the speed of propagation of the action potential along neurons,[1] and plays an important role in many other bio-electronic phenomenon, including the beating of a cardiomycyte,[2] as well as the creation and consumption of energy in organelles such as chloroplasts for photosynthesis and mitochondria for oxphos and ATP synthesis.[3] The capacitance also plays an important role in energy storage technologies such as batteries and supercapacitors,[4–6] and governs the behavior of numerous electrochemical sensors.[7]

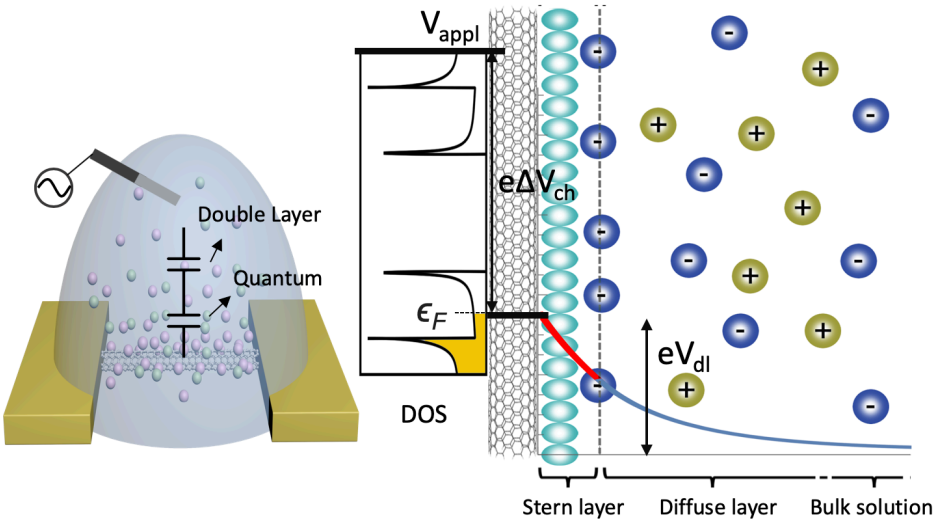

Figure 4.1: Left panel: 3D cartoon of the system under study. Right panel: Schematic of the double layer structure with the state alignment between the nanotube and the solution. The applied voltage drops in part as the change of chemical potential of the nanotube, and then decays exponentially in the Stern and diffuse layer in the solution.

Until this work, the size of typical electrodes has been macroscopic compared to the de Broglie wavelength of the electrons in the solid. With the modern advent of nanomaterials, that has changed, and reduced dimensional materials such as 2d materials (graphene and beyond graphene), 1d materials (nanoribbons, nanotubes, nanowires), 0d materials (quantum dots) give rise to a whole class of electronic devices in which the size of the structure becomes comparable to the electron wavelength. Just as Bohr surmised at the dawn of quantum mechanics that the wave function as an electron circles an atom must return to its original value (hence the allowed wavelengths and energies in an atom are quantized), this gives rise to quantization of energy levels within any solid whose size approaches the electron wavelength in any dimension.

What is the effect of this on the capacitance between a reduced dimensional system and a liquid electrolyte? While this has been addressed in theory, in practice for d < 2, it has

been impossible (until now) to answer for one very important practical reason: It is almost immeasurably small. The quantum capacitance of a nanowire/nanotube is generally of order 100 aF/μm. In dry systems, it is possible to isolate the nanodevice from the system[8] but in an electrolyte system, the electrolyte contacts everything and creates a stray overlap capacitance between contact electrodes and the nanodevice, which swamps the signal that is being measured.

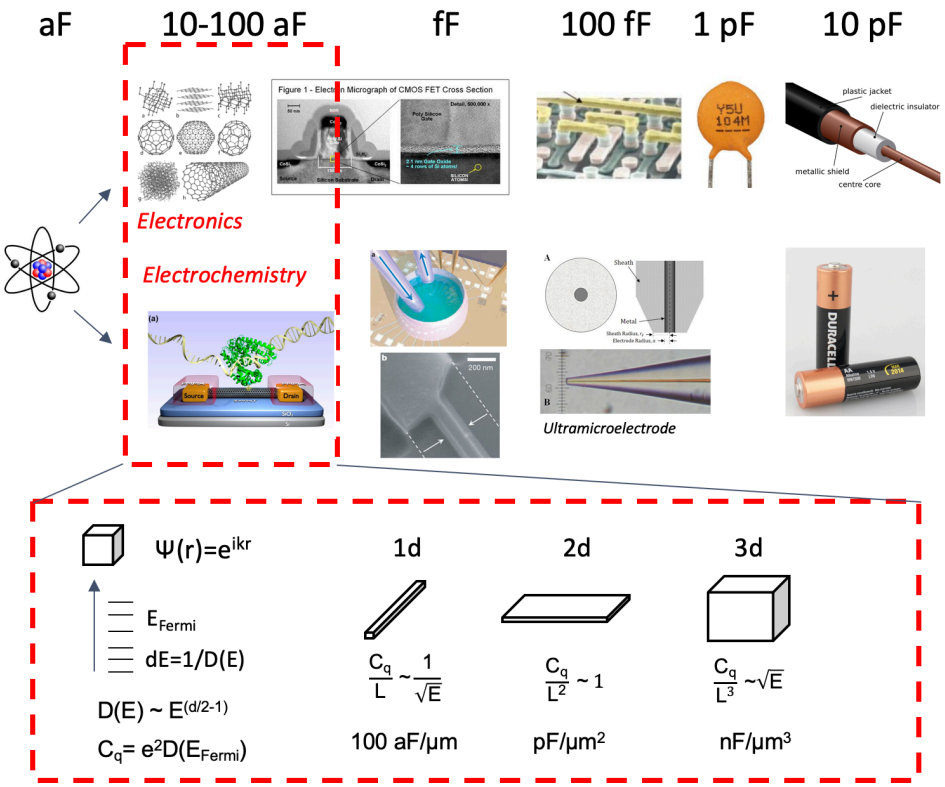

Figure 4.2: Typical capacitance values for various conditions, from atomic to macroscopic. Top: Dry environment (Ref. [66–68]). Middle row: liquid environment (Ref. [69–71]). The inset indicated schematically the density of states for materials whose dimension approach the de Broglie wavelength of the electrons, adding an additional quantum capacitance which is not significant in the larger macroscopic electrode.

At the same time, the "classic" Debye layer capacitance deviates from textbook behavior when the radius of curvature of the electrode becomes comparable to the solvated ion radius, also of the order of 1 nm. This can occur in one of two topologies: Nano-caves, and

nano-electrodes. In a nano-cave, the cave size becomes small in a porous material giving non-trivial capacitance, changing the behavior by up to 3 times the classic calculation. This was discovered experimentally and only later explained by electrochemical simulations.[9–12] In nano-electrodes, the electrode protrudes into the liquid, and the predicted behavior deviates substantially from the classic one.[13–16] The results of both of these effects (quantum and electrochemical) give rise to a new regime of electrochemical behavior for nanosystems, qualitatively different from both by new well-studied dry nano-systems and classic large area electrochemical systems (Figure 4.2).

In this work, in order to resolve the small capacitance (of order 100 aF) above the background stray capacitance (of order 100 pF), we designed, developed, and implemented an integrated, on-chip shield. With this technique, we measure the capacitance between a 1d material and an electrolyte. With this system, we measure the capacitance of one to a few nanotubes quantitatively as a function of both bias potential (from – 0.7 V to 0.3 V) and ionic concentration (from 10 mM to 1M KCl) at room temperature. The corresponding capacitance in this case consists of two types of capacitance in series: a quantum component arising from the electronic density of states and an electrochemical component arising from the ion screening and diffusion. By varying the electrolyte concentration, we determine the relative contributions of the quantum and electrochemical capacitance. This technique, proven in concept for the case of carbon nanotubes, is applicable to a broad class of reduced dimensional devices, including nanowires, nanoribbons, and quantum dots, of any material. Thus, this represents a first in class measurement of the quantum effects on capacitance in reduced dimensional systems in contact with liquid electrolytes, an important and emerging theme in the interface between nanotechnology, energy, and life.

4.2 Results and Discussion

4.2.1 Integrated on-chip shield

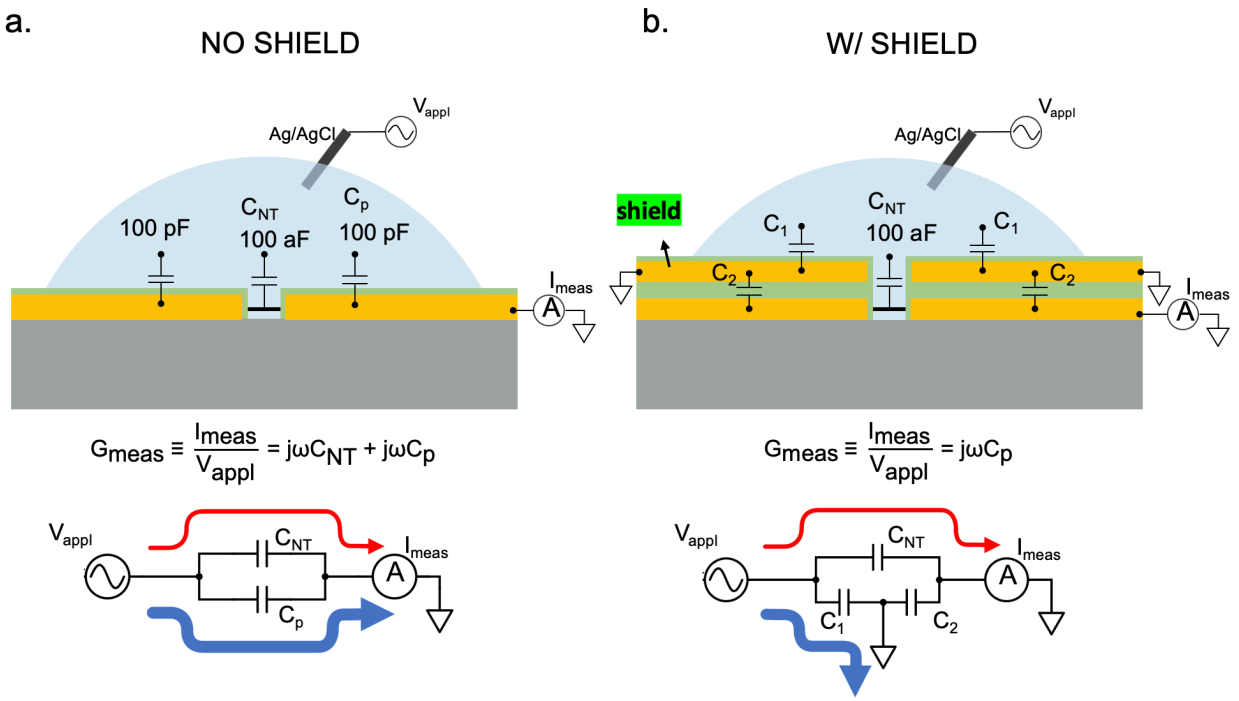

Figure 4.3: Schematic diagrams and corresponding circuits of a liquid-gated nanotube device, (a) w/o integrated shield, and (b) w/ integrated shield. For non-shielding case, the measured current between the liquid and the contact electrodes contains parasitic current (blue arrow line in the left panel) that is ~ 6 orders of magnitude larger than the current passing through the nanotube (red arrow line), which easily swamps the current signal of interest and make it too difficult to measure. For the shielding case, the parasitic current (blue arrow line in the right panel) is directed to ground instead of the current meter.

Figure 4.3 illustrates the integrated on-chip shield concept and design. In the unshielded measurement geometry (Figure 4.3a), the measurement of the nanotube-electrolyte capacitance is typically done in parallel with a much larger background parasitic capacitance which must be subtracted off. With the liquid in capacitive contact with the contact pads, this procedure is not feasible, as the parasitic capacitance is typically of order 100 pF and the capacitance to be measured is of order 100 aF, six orders of magnitude smaller. Note that microfluidic confinement of the electrolyte may help to reduce the

parasitic capacitance, however, to reach the required level (order of 100 aF), it requires an extreme narrow channel which will generate large streaming potential and significant noise due to the current fluctuation along the channel and the local potential drift at the device gate.[72–74] (In a dry environment, the liquid is not present so this procedure is feasible.[8,75]) In order to mitigate the effects of the unwanted parasitic capacitance on the measurement, we implemented a "shield" which shunts all parasitic capacitive current to ground, while still allowing the capacitive current through the device-electrolyte interface to flow into the current amplifier to be measured (Figure 4.3b). The Si/SiO_2 substrate is used as a bottom shield to further eliminate the background parasitic capacitance. Thus, the top and bottom shields together form a sandwich-like structure that effectively shields out the parasitic current as well as noise from the environment.

4.2.2 Fabrication process

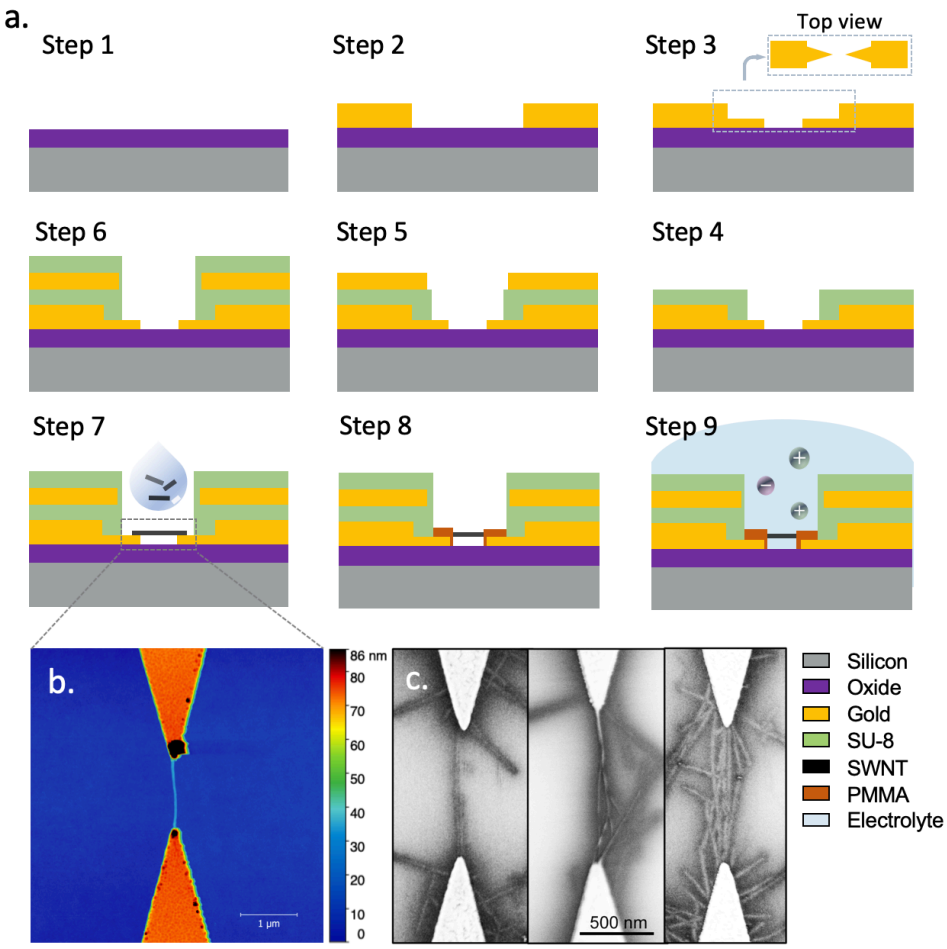

Figure 4.4: (a) Fabrication process for a SWNT FET device with the integrated shield. Step 1: A highly doped silicon wafer with a 300 nm oxide layer. Step 2: Source drain electrodes fabrication using standard photolithography. Step 3: Fine-tip electrodes fabrication using e-beam lithography. Step 4: Dielectric layer fabrication. Step 5: Top shielding layer fabrication. Step 6: Top passivation layer fabrication. Step 7: Nanotube deposition using dielectrophoresis (DEP). Step 8: Final PMMA passivation layer with only the nanotube exposed. Step 9: Electrolyte solution brought in contact with the nanotube acting as the top-liquid gate. (b, c) Topographic images of the SWNTs imaged by AFM and SEM. The SWNTs were DEP-attached to the source-drain electrodes. Multiple amounts of SWNTs (1~100 nanotubes) between the source and drain electrodes were observed.

We fabricated the device and integrated on-chip shield according to the procedure outlined in Figure 4.4. The device fabrication is detailed in the Methods section 4.3 . Briefly, a pair of source-drain electrodes is first fabricated on top of a highly doped low-resistivity silicon wafer with a 300 nm oxide layer, using standard photo and e-beam lithography

followed by metal evaporation and lift-off processes. A three-layer structure (dielectric/metal/dielectric layers) is then fabricated layer-by-layer covering the source-drain electrodes everywhere except for a small window (~ 10 by 10 um) opened in the center of the device. This window allows the front tips of the electrodes to be exposed and form contact with liquid solutions. SU-8 is chosen as the dielectric material, which is spin-coated to have ~ 1 um in thickness and patterned using photolithography. For the metal layer, 50 nm gold is deposited with 30 nm of Ti underneath to increase adherence to the dielectric layer. After the three-layer structure is made, the device is brought under oxygen plasma to etch out any photoresist residue on the tips of source-drain electrodes. At this stage, the SWNTs is deposited across the source-drain contact electrodes using dielectrophoresis (DEP).[76–81] We drop a purified SWNT-suspended solution (from NanoIntegris) into the central window and use DEP force to attract the SWNTs to align and attach onto the contact electrode tips. An anneal (160 °C, 5 mins) is used afterward to enhance the electric contact between the electrode tips and the SWNTs. Finally, the device is spin-coated with PMMA as the final passivation layer, and a 600 nm width channel is opened using e-beam lithography to expose the SWNTs and allow aqueous solution to come in and form contact. Due to the hydrophobic properties of the small central chamber, bubbles are easy to form and prevent the contact. Therefore, we always wet the device with alcohol before adding any aqueous solution. In the same batch of devices, one random picked device will omit and only omit the SWNT deposition step to behave as a control device, which allow us to estimate the remaining parasitic capacitance. We observed the parasitic capacitance for a control device is ~ 1 fF, and the measured capacitance of the control device has no dependence on both the back and the top gate voltage.

4.2.3 Transport characteristics

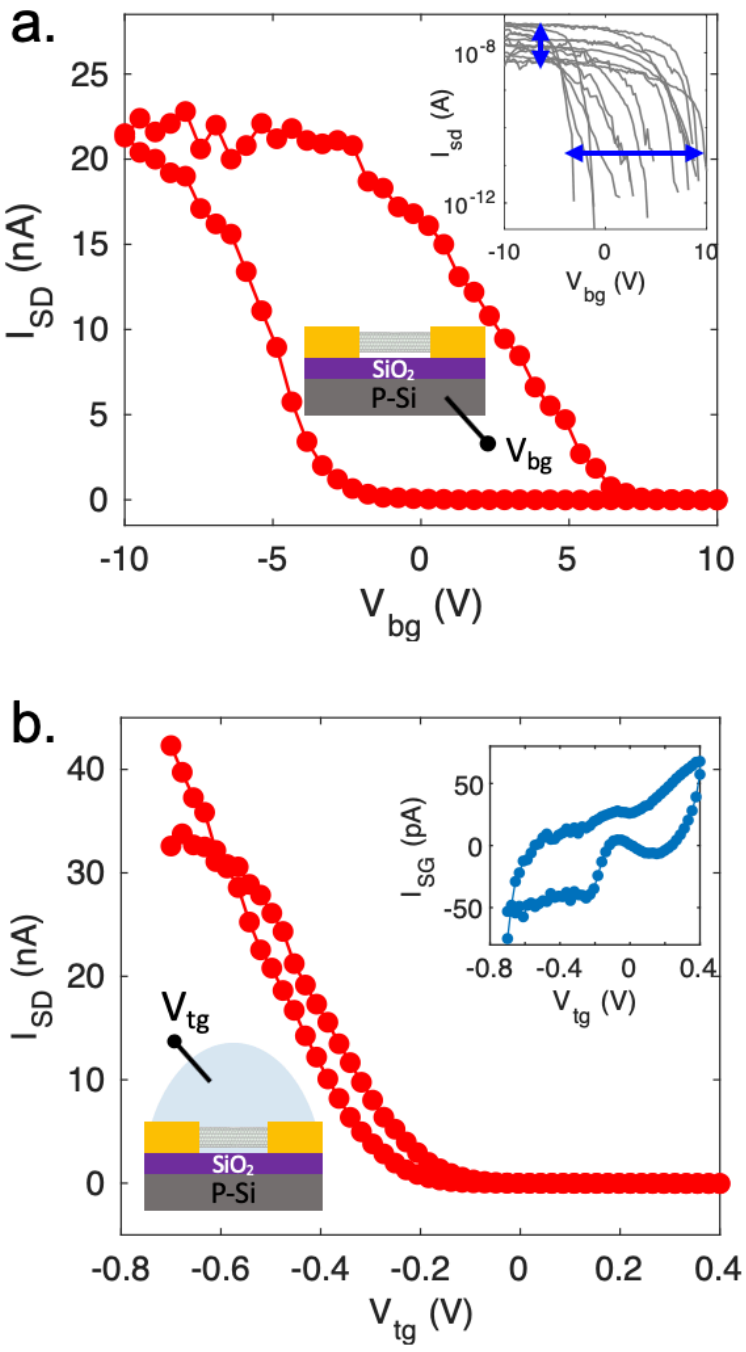

Figure 4.5: (a) Source-drain current as a function of the back-gate voltage before applying the liquid-gate. The source-drain bias voltage is 100 mV, and the back-gate voltage sweeps between -10 V and 10 V at 3 V/s. The inset shows the source-drain current on a logarithmic scale for different devices. (b) Source-drain current as a function of the top liquid-gate voltage. The source-drain bias voltage is 100 mV, and the liquid-gate voltage sweeps between -0.7 V and 0.4 V at 0.1 V/s. The inset shows the capacitive gate current before applying the shield connections.

We first characterize the transport of the nanotube devices by measuring the gate dependent source-drain conductance (see Figure 4.5). A voltage bias (100 mV) is applied between the source-drain electrode and the current is monitored at the source electrode to quantify the conductance of the nanotubes. The nanotube is first back-gated by the silicon substrate between –10 V and +10 V. After the back-gate measurement, a droplet of electrolyte (100 mM KCl) is placed on the center of the device, and a top-gate voltage (between – 0.7 V to 0.4 V) is applied to the electrolyte solution using an Ag/AgCl reference electrode. Figure 4.5a shows the source-drain current as a function of the back-gate voltage, and Figure 4.5b shows that as a function of the top-liquid-gate voltage. In the switching range of the both gates, exponential dependence is observed, suggesting semiconducting SWNTs are formed across the source-drain electrode tips. The slope of the subthreshold in the back-gate measurement is ~ 800 mV/decade, while in the liquid-gate measurement, due to the strong coupling of ions, the slope is large and about 60~90 mV/decade, agreeing with others' works.[82,83] The SWNTs behaved in the p-type conductive region at negative gate voltage and no n-type conductance was observed in our measurement range. The back-gate measurement in a dry environment shows a large hysteresis phenomenon,[84] however in the liquid-gate case, the hysteresis phenomenon is very minor. The transport characteristics for multiple devices are shown in the inset of Figure 4.5a; the different ON-state current and threshold voltage suggest different number and doping of SWNTs formed across the source-drain tips. The liquid-gate current is shown in the inset of Figure 4.5b, which is minor and mainly capacitive current rather than charge transfer current at the SWNT's surface. (Note that the transport measurement was done prior to the shield connections and capacitance measurement)

The two-stage DC transport measurements (the back-gated and the liquid-gated) are also used as a verification of the devices prior to the electrochemical capacitance measurements. 42 devices were tested, in which 18 devices showed on/off switch when back-gate was applied (the inset of Figure 4.5a), which confirms semiconducting nanotubes had been successfully deposited across the source-drain electrodes and formed a good electrical contact. Next, in the liquid-gate test, 4 out of the 18 devices showed on/off switch, which verified the liquid solution had contacted the nanotube directly, no bubbles or photoresist residue blocked in between. These 4 devices were then carried to the electrochemical capacitance measurement, discussed in the next. Although measurement on a large number of devices can provide better statistical analysis, capacitance measurement on these 4 devices has shown consistency with each other both on the shape of the capacitance and the order of value. The low yield in the last step (writing the liquid-gate channel to expose the nanotubes) was due to the unpredictable PMMA thickness in the central window, which can be improved a lot with using a thinner SU-8 dielectric layer to prevent PMMA building up at the sidewalls. This was confirmed in our test batches in the end.

4.2.4 Capacitance measurement

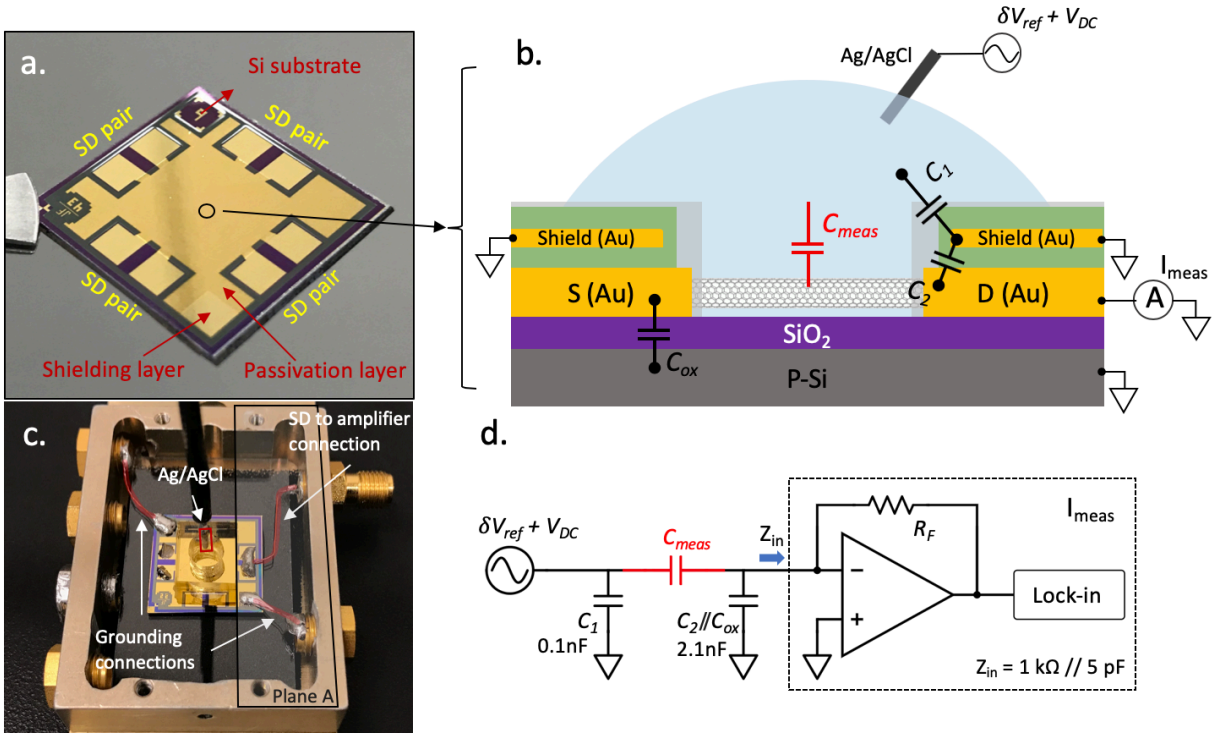

Figure 4.6: (a) Optical image of the SWNT device chip containing 4 pairs of source-drain electrodes. The source-drain electrodes are patterned underneath the shielding layer and form contact with nanotubes in the center of the chip. (b) Schematic diagram of the SWNT device, with the parasitic capacitances labeled. C_1 (0.1 nF), C_2 (0.1 nF), and C_{ox} (2 nF) are the parasitic capacitances of the top passivation layer, the medium dielectric layer, and the bottom oxide layer respectively. The top shielding layer and the bottom silicon are both grounded. The source and drain electrode are wired together and connected to the measurement input. A phase-locked AC perturbation voltage is added on the liquid gate; the corresponding complex current is measured by a pre-amplifier and a following lock-in amplifier to quantify the capacitance between the carbon nanotube and the electrolyte solution. (c) Wire connections of the chip inside a faraday box. Copper wires between the chip and the SMA connectors are highlighted with red color. A PDMS chamber is placed on top of the chip as a liquid reservoir. The Ag/AgCl reference electrode is brought in the reservoir by a coaxial cable. Plane A is covered with grounded metal plate during the measurement to further eliminate the parasitic current. (d) Circuit model of the device and the measurement. Currents that pass through the parasitic capacitances (C_1, C_2 and C_{ox}) are directed to ground. Currents that pass through the SWNT-electrolyte interface are input to the pre-amplifier and the lock-in amplifier, to characterize the corresponding capacitance C_{meas}. The input impedance of the pre-amplifier is 1 kΩ // 5 pF.

Once the DC transport characteristics confirm the presence of a well-behaved semiconducting nanotube in the device, an AC perturbation voltage is superimposed on top of the DC liquid-gate to measure the capacitance as follows (Figure 4.6). An AC voltage (1

kHz, 50 mV in RMS) is applied to the electrolyte using an Ag/AgCl reference electrode, and the source and drain of the nanotube are wired together and connected to a virtual ground which measures the corresponding AC current between the electrolyte and the nanotube. The AC voltage on the electrolyte causes a capacitive current to flow into the nanotube and into the virtual ground; the measured capacitance is then determined by $V_{AC}/I_{meas} = 1/j\omega C_{meas}$. In practice there are additions to this, such as the ohmic contact resistance of the SWNT to gold, the nanotube resistance, the electrolyte resistance, and a possible faradaic current from the nanotube to the electrolyte. These resistive components contribute negligible measured current in comparison to the capacitive current of the nanotube-to-electrolyte, as discussed in detail in 4.2.9 . A low noise pre-amplifier (FEMTO DLPCA-200, with input noise current 13 fA/$\sqrt{Hz}$) followed by a lock-in amplifier (Stanford Research SR830) is used for the current measurement. The top and bottom shield layers are grounded; the source-drain electrodes are shorted together and connected to the input of the transimpedance pre-amplifier. Most of the current distribution through the liquid and air is terminated at the grounded shields, only the current that passes through the liquid-SWNT interface finally gets carried out to the measurement electronics. To further eliminate the parasitic current and environmental noise, a grounded aluminum foil is used to cover the exposed source-drain electrode areas (plane A in Figure 4.6c) such as the soldering points and the current collection wires. After proper shielding, the parasitic capacitance measured on a control device is decreased to ~ 1fF. This is essential to make the capacitance measurement possible for individual SWNTs exposed to conductive liquid.

To further quantify the electrochemical capacitance of nanotubes with respect to a unit length, we want to know the total length of the nanotubes that contributes to the measured

signal and divide the measured capacitance by the total length. However, due to the nature of the DEP method we used here, the total number and length of nanotubes are difficult to determine. Here, we provide a rough estimation of the total length using SEM imaging. Note that ~30% error is expected, since some tubes may not be electrically connected, and some are bundled, hidden or hardly visible. The total numbers of nanotubes are counted as ~ 20, 20, 10, 3 respectively for the 4 validated devices, and the separation of the contact electrodes (hence the length of nanotubes) is ~ 1 μm. A better-controlled approach (such as CVD-grown nanotubes) rather than DEP can provide length-calibration with higher precision. However, the shape of the capacitance and the order of value have been measured in this work, which can be used as a basis for the future measurements and applications. Semiconducting SWNTs with similar diameters have similar DOS near the Fermi level.[85] The nanotubes we used here have a narrow diameter range (between 1.2 nm and 1.4 nm). Hence the averaged capacitance of a few mixed nanotubes with similar diameters still reveals the properties of the DOS for a single one (see Figure 4.10b).

4.2.5 Capacitance vs. gate voltage

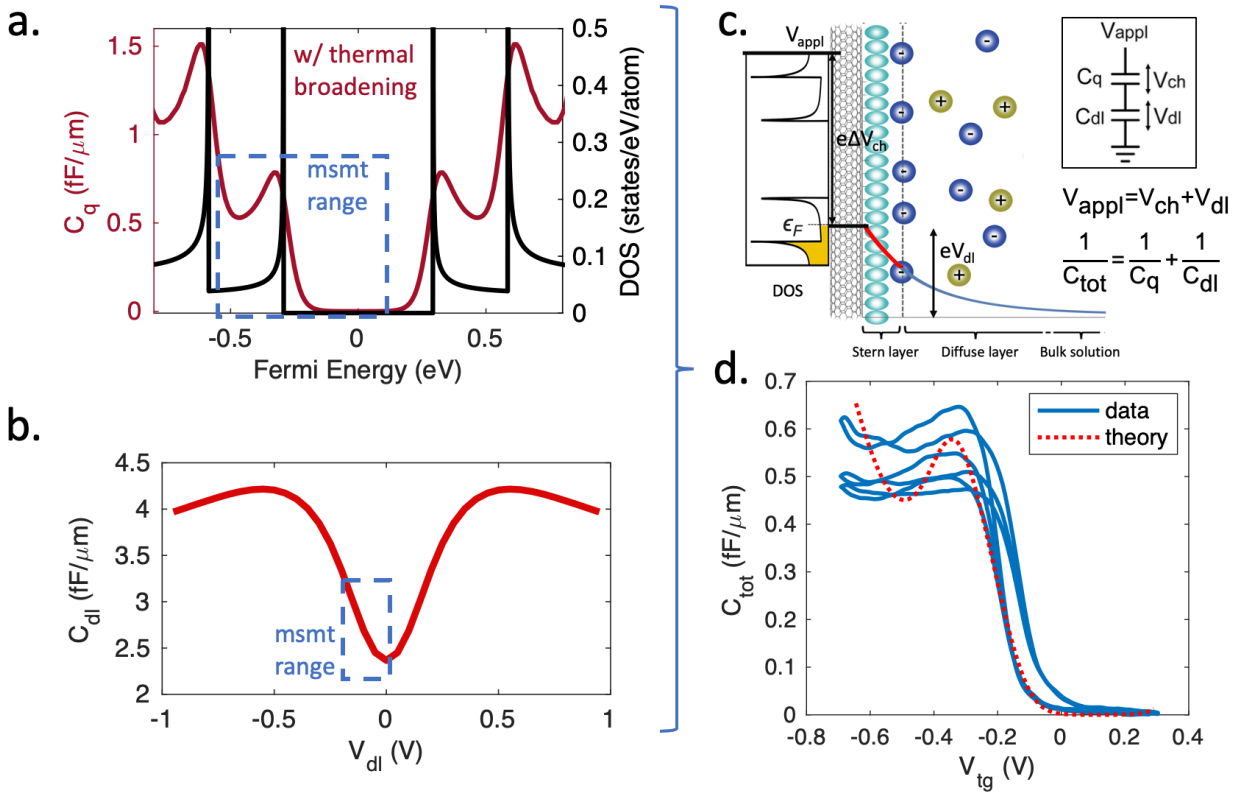

Figure 4.7: (a) Calculated density of states (DOS) of a SWNT with diameter 1.2 nm (black curve) and the resulting quantum capacitance (red curve) at room temperature. (b) Calculated double layer capacitance of a nanocylinder with diameter 1.2 nm, immersed in 10 mM KCl aqueous solution. (c) Schematic of the double layer structure with the state alignment between the nanotube and the solution. The applied voltage drops in part as the change of chemical potential of the nanotube, and then decays exponentially in the Stern and diffuse layer in the solution. (d) Measured SWNT capacitance as a function of the liquid-gate voltage at 100 mV/s (three cyclic scans are shown), in caparison with the theoretical estimation (dashed red curve).

We first discuss the measured capacitance at low electrolyte concentration (10 mM KCl). The quantum capacitance is proportional to the DOS, which is sharply dependent on the Fermi energy. At room temperature, this dependence is thermally broadened. Additional measurement broadening is due to the finite applied AC voltage swing and the small variation (±0.1 nm) of the tube diameters, which will be discussed later. Figure 4.7a shows the DOS and thermally broadened quantum capacitance of a SWNT with 1.2 nm diameter as functions of the Fermi energy. The DOS of a SWNT is calculated based on zone-

folding of graphene's band structure.[8,17] In addition, the electrochemical capacitance depends on the electrolyte-nanotube potential drop. The theory of this for 1d conductors is non-trivial and was discussed by us in ref.[16] and others.[14,15] Figure 4.7b shows the predicted electrochemical double layer capacitance as a function of the double layer potential V_{dl} in the solution. The voltage drop and Fermi energy together sum to the applied voltage, and the two capacitors add in series, as show in Figure 4.7c. Since we use an aqueous electrolyte, we restrict the applied voltage between -0.7 V to 0.3 V to avoid electrolysis. This restricts the measurement range of the Fermi energy E_F and the double layer voltage V_{dl} to be the box regions shown in Figure 4.7a,b. Since the quantum capacitance is smaller by a factor of 5, it dominates the total capacitance-voltage curve, shown theoretically in Figure 4.7c in the red dashed line. The dominant component is the vanishing total capacitance in the "gap region" around 0 volts, and a sharp turn on as the voltage approaches the first singularity in the 1d DOS. The singularity is thermally smeared, and the second singularity is just visible within our voltage window (another measurement in Figure 4.10 shows the 2nd singularity). The electrochemical capacitance in comparison varies smoothly, but also increases with decreasing voltage in our window.

The experimental result (Figure 4.7d) shows this expected behavior, including a dramatic vanishing of C_{tot} at around zero bias, as well as a point of inflection and then increase, indicated that the first singularity in the DOS has been reached. Multiple cyclic sweeps are shown and consistent from sweep to sweep within 10%, which little hysteresis. The deviation over time is possibly due to surface contamination and the resulted doping from electro-migration and minor redox reactions. This confirms measurement of the total

capacitance of a nanotube in contact with an electrolyte, the first such measurement, enabled by the integrated on-chip shield.

4.2.6 Quantitative theory

We next discuss the quantitative predictions that led to the red curve in Figure 4.7c, as well as measurements and theory at different electrolyte concentrations. Whereas the quantum capacitance depends only on the internal quantum structure of the nanotube (DOS), the electrochemical capacitance depends strongly on the molarity of the solution. This gives us an experimental "knob" to determine the relative contributions of the two capacitances to the total capacitance quantitatively. To compare the measured capacitance with theory, we calculated each capacitance component (quantum and electrochemical) separately, and then combined them together in series to calculate the total capacitance as a function of the total applied voltage.

$$C_{tot}^{-1} = C_q^{-1} + C_{dl}^{-1} \tag{4.1}$$

The quantum capacitance at a given chemical potential V_{ch}, is given by,[8,17,86]

$$C_q(V_{ch}) = \int_{subband} dE \cdot F_T(E - eV_{ch}) \cdot C_q^0 \sum_{j=-3}^{3} (1 - (E_j/E)^2)^{-1/2}$$
$$E_j = \hbar v_F \frac{2j}{3\mathrm{d}}, C_q^0 = \frac{4e^2}{\pi \hbar v_F} \tag{4.2}$$

where, $F_T(E) = (4k_BT)^{-1}\mathrm{Sech}^2(E/2k_BT)$ is thermal broadening function, k_B is Boltzmann constant, T is temperature, v_F is the Fermi velocity, and we included the first three electron

and hole sub-bands. Figure 4.7a shows the calculated quantum capacitance as a function of the Fermi energy. Due to the choice of the reference electrode and the doping of the SWNT, the potential of the SWNT at the half-filling state has an offset with respect to the Ag/AgCl reference electrode. This offset can be estimated by aligning the threshold of the measured capacitance-voltage curve with the theoretical curve. Figure 4.7d shows aligned curves after setting a voltage offset ~ 0.12 V to the theoretical curve.

The double layer capacitance for a carbon nanotube has been calculated in our previous work, based on a modified Poisson-Boltzmann equation,[13,16,49,57,58,60]

$$\frac{1}{r}\frac{d}{dr}\left(\varepsilon_r\varepsilon_0 r\frac{d}{dr}\right)\varphi = \frac{2\rho_q \sinh\left(\alpha\cdot\frac{q\varphi}{k_BT}\right)}{1+2v\sinh^2\left(\alpha\cdot\frac{q\varphi}{2k_BT}\right)} \tag{4.3}$$

where, φ is the electric potential distribution along the radial direction of a nanotube in solution, ρ_q *is* the space charge density in the bulk solution, α is the correlation parameter, q is the charge of the ions, and ν is the packing parameter. Together with the appropriate boundary conditions listed in our previous work,[16] we can calculate the potential distribution in the contact solution. From the potential distribution, the double layer capacitance can be determined,

$$C_{dl}(V_{dl}, c_0) = \frac{dQ}{dV_{dl}} = -\varepsilon_r\varepsilon_0\frac{d}{dV_{dl}}\oiint_{r=r_H}\nabla\varphi\cdot\overrightarrow{dS} \tag{4.4}$$

Figure 4.7b shows the calculated double layer capacitance of a nano-cylindrical electrode with 1.2 nm diameter, immersed in 10 mM KCl aqueous solution.

With the two types of capacitance in series, the applied liquid-gate potential V_{appl} splits into two parts: the chemical part V_{ch} over the quantum capacitance C_q, and the electrostatic part V_{dl} over the double layer capacitance C_{dl}. The ratio between the two capacitances is fully determined by the ratio of the potential drop between the two,

$$\frac{C_q}{C_{dl}} = \frac{V_{dl}}{V_{ch}} \tag{4.5}$$

Combining the equations 4.1-4.5, we can calculate the total capacitance as a function of the applied gate potential. Figure 4.7d shows the calculated curve plotted together with the measured one for the case of 10 mM. The measured capacitance shows clearly the main predicted features of this model: The capacitance vanishes near the origin due to the quantum capacitance component vanishing there arising from the bandgap in the density of states. As the voltage is reduced, the capacitance sharply rises, due to the sharp density of states and the band edge singularity in the 1d material. The second subband causes the capacitance to rise even more, although the second subband is not fully resolved. (See Figure 4.10c where it is more clearly observed). The electrochemical capacitance rises more slowly with reducing voltage, leading to a smoothing of the singularity in the DOS effect, together with thermal and voltage smoothing.

4.2.7 Capacitance vs. ionic concentration

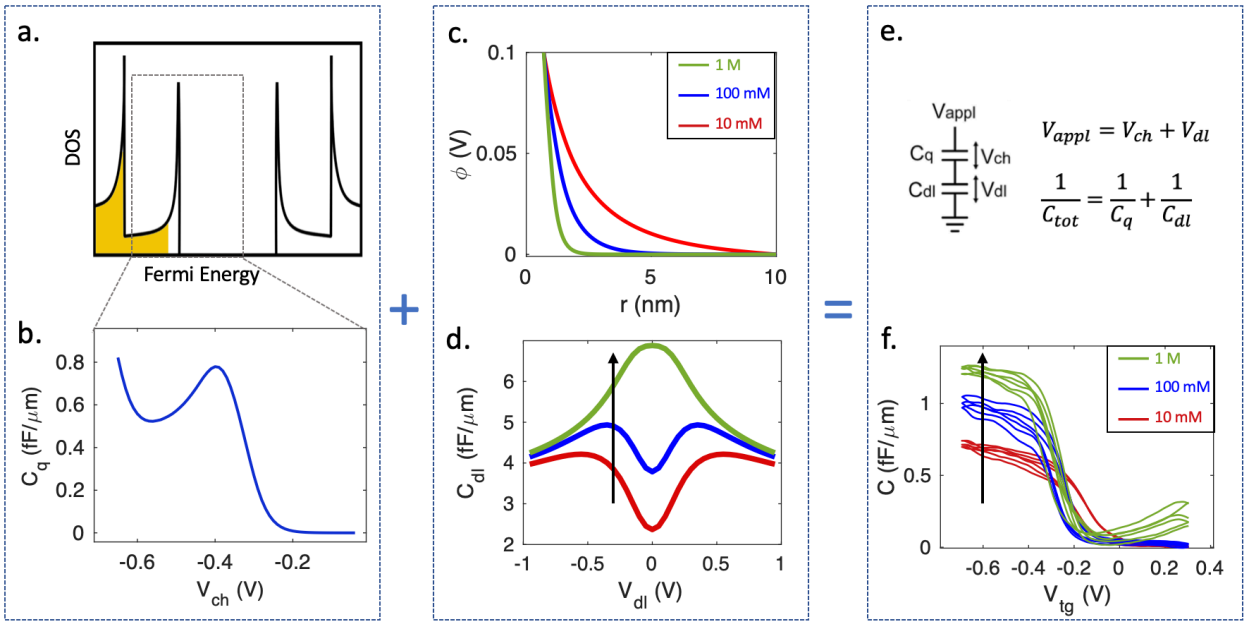

Figure 4.8: (a) The DOS of a SWNT, and (b) the resulted quantum capacitance. (c) The different Debye screening length of a SWNT in solution with different ionic concentrations, and (d) the resulted double layer capacitance. (e) The relationship between the two types of capacitances. (f) The measured SWNT capacitance as a function of the liquid-gate voltage at different ionic concentration between 10 mM and 1M. Three cyclic scans are shown for each concentration.

With the basic model and experiments well in agreement, we now discuss the theoretical and experimental dependence on concentration in more detail. The applied voltage is divided among the two capacitors, and this ratio will depend on the value of the capacitances, which depends on the electrolyte concentration through the dependence of C_{dl} on the electrolyte concentration. As discussed in our previous paper,[16] C_{dl} vs. V_{dl} can peak or trough at the origin depending on the concentration. Figure 4.8d shows this theoretical dependence for three concentrations (10 mM, 100 mM, 1 M). This can be combined with the quantum capacitance calculations to predict the dependence of the total capacitance on electrolyte concentration. As can be seen in Figure 4.8d, the overall effect of the increasing concentration in our voltage window is to increase C_{dl}. This would increase

the overall capacitance, and this trend is indeed observed in the data, as shown in Figure 4.8f.

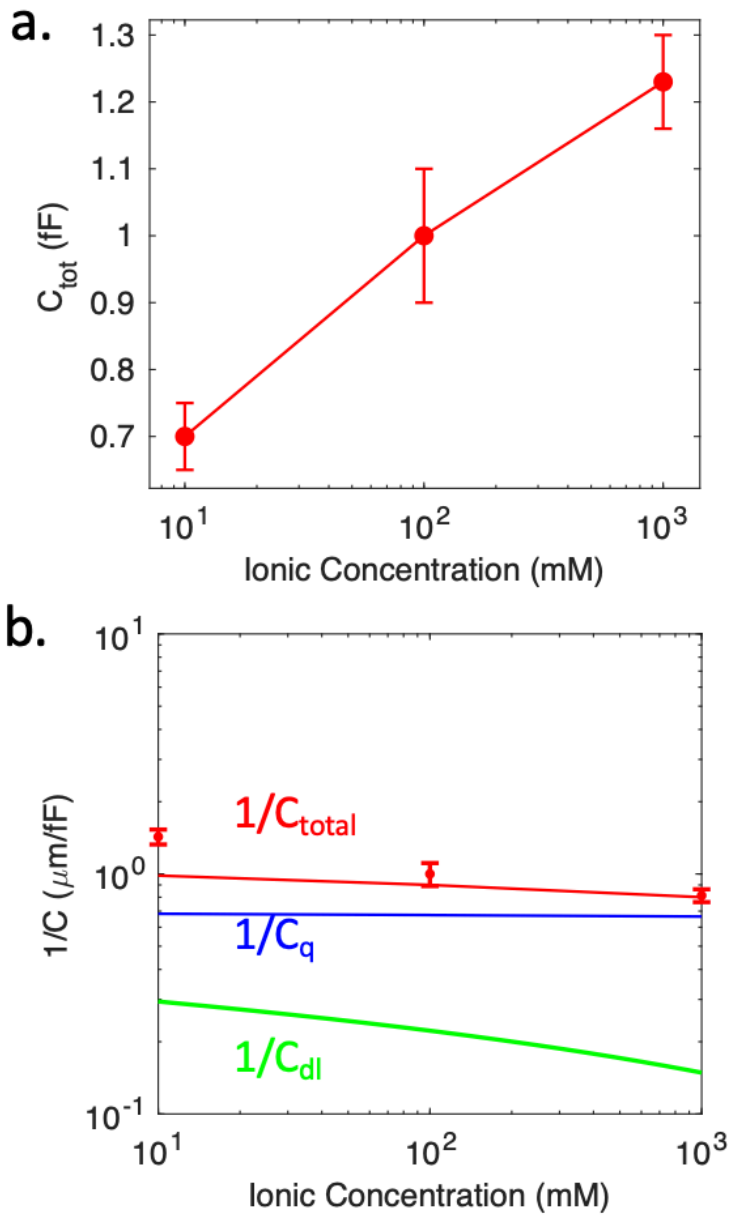

Figure 4.9: (a) The measured total capacitance as a function of ionic concentration at a fixed gate potential -0.7 V. (b) The calculated total capacitance and its components as functions of ionic concentration at a fixed gate potential -0.7 V.

In order to dissect this further, we plot in Figure 4.9 the measured total capacitance as a function of the ionic concentration at a fixed gate potential –0.7 V. At this potential, the

double layer and quantum capacitance are predicted and shown in Figure 4.9b. The model and the data are in agreement with the fundamental conclusion of this paper that the quantum capacitance dominates, and the trend with increasing ionic concentration confirms this interpretation since the total capacitance increases with increasing ionic concentration in agreement with the expectations of the theoretical model. The change of the slope of the capacitance based on ionic concentration is slightly higher than the theory, whose origin is unknown.

4.2.8 Ensemble averaged capacitance

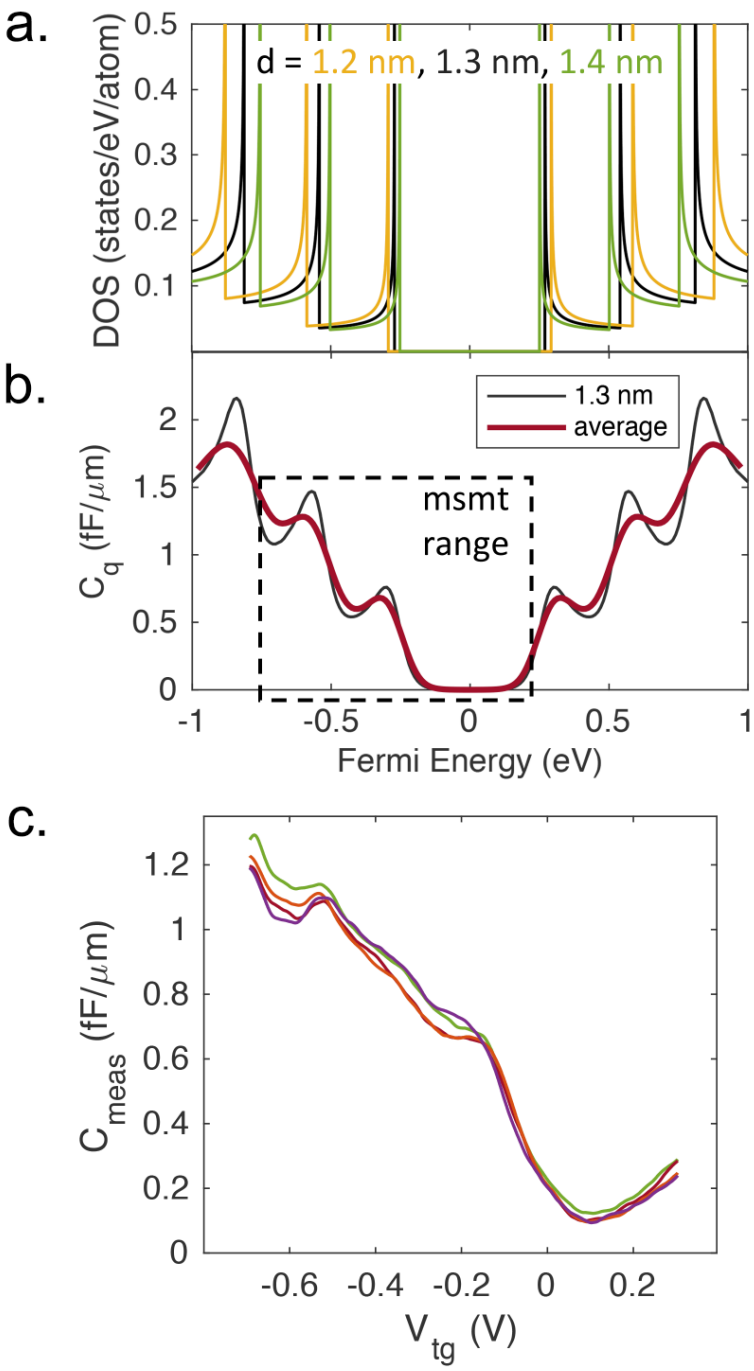

Figure 4.10: Average capacitance of mixed SWNTs as a function of the liquid-gate voltage. (a) DOS of SWNTs with different diameters. (b) Calculated average capacitance of SWNTs with diameters following a normal distribution (mean at 1.3 nm and deviation at 0.1 nm), and its comparison with the capacitance of a single tube. (c) Measured capacitance of a mixture of SWNTs. Multiple measurement sweeps are shown.

In a prior work,[16] we measured the ensemble capacitance for millions of nanotubes in a mat. In this work, we provide a bridge to that work by measuring a few parallel nanotubes with similar diameters (1~50 tubes, see Figure 4.4c), using our integrated on-chip shield. For devices that contain a mixture of nanotubes with similar diameters, the misaligned subbands (Figure 4.10a) will overlap and result in a shift-averaged capacitance curve, which can be calculated by,

$$C_q(V_{ch}) = \int d\mathrm{d} \cdot \mathcal{N}(\mathrm{d}_0, \Delta\mathrm{d}) \cdot C_q(V_{ch}, d) \tag{4.6}$$

where $N(d_0, \Delta d)$ is the probability density function for the normal distribution of the tube diameters (mean diameter d_0 = 1.3 nm and standard deviation Δd = 0.1 nm). Figure 4.10b shows the averaged quantum capacitance of a mixture of nanotubes (red thick curve) versus that of a single one (black thin curve). The overall capacitance gets smeared when mixed nanotubes are measured, while the shape of the capacitance curve is still present. Figure 4.10c shows a measurement example, in which multiple nanotubes (20 ~ 30 tubes) are attached across the source-drain electrodes. The theoretical capacitance curve agrees with the measured curve, regarding the shapes and bump positions at the first two singularities.

The shield and small number of tubes in this work enables us to explore the dependence on a wide range of voltages (-0.7 V to 0.3 v), in contrast to our previous work for large number of nanotubes, where we only explored the capacitance at the clear ON state (V_{tg} = -0.7 V to -0.5 V). In the previous work, millions of nanotubes formed macroscopic film as the gate channel, whose capacitance was measured as a whole. Due to

the large length of the gate channel (~ 200 μm), nanotubes were gated unevenly along the channel. The unevenly gating became severe when the sheet resistance of the channel got increased (V_{tg} > -0.5 V), hence it prevented an accurate capacitance measurement near the OFF-gate range. Here in this paper, nanotubes are attached to the contact electrodes across the gate channel parallelly and individually, the capacitance value of nanotubes can be determined in a wider range of gate voltage, including the OFF state. Because of this qualitatively new regime, in this work we are able to clearly observe the bias dependence in the gap, and in the second subband, thus demonstrating for the first time the combined effects of quantum mechanics and electrochemistry in this new regime of operation.

4.2.9 Details of C_{meas}

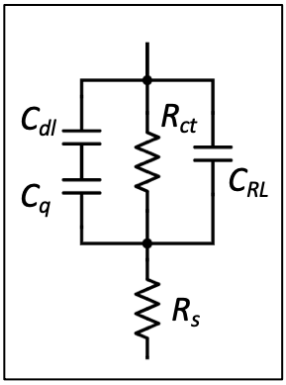

The measured capacitance C_{meas} contains the quantum capacitance C_q and the double layer capacitance C_{dl} in series as the main components. In parallel with the capacitances there are the charge transfer resistance R_{ct} which is much larger compared to the capacitive impedance in our measurement window and can be ignored. Also, in parallel, there is the remaining parasitic capacitance at non-shielded space, which is constant and can be simply subtracted as a background. Finally, the electrode contact resistance and the resistance of the electrolyte is much smaller than that of the tube-liquid interface, hence it

can be ignored. Note that the double layer capacitance is not an ideal capacitance; it has a phase shift value different from −90°, which can be phenomenally described by adding a constant phase element (CPE) in series with the double layer capacitance.[43,44,46] The phase shift phenomenon was also observed in liquid-gated graphene studies.[87] The ratio between the imaginary part of the current and the real part current after the background subtract suggests that the phase shift of the current is at the value ~ 70°.

4.2.10 Conclusion

Taken collectively, these measurements demonstrate the net effect of quantum capacitance and atomic scale radius of curvature for one, a few, to a macroscopic number of nanotubes in contact with an electrolyte. As such, it provides an experimental foundation backed by detailed electrochemical calculations and quantum theory that covers the general case of *any* number of nanotubes in contact with liquid. Although we have shown how the quantum and electrochemical capacitance of a carbon nanotube as a 1d wire, this technique is applicable to a broad class of materials, including nanoribbons, quantum dots, nanowires, and any other small capacitance structures in contact with liquid solution, which is an important and emerging theme in the interface between nanotechnology, energy, and life.

4.3 Methods

Device Fabrication. Carbon nanotube FET devices with integrated on-chip shield were fabricated using the process flow shown in Figure 4.4a. Step 1: A highly p-doped silicon wafer with a 300 nm thermal oxide layer was cleaned using Remover PG, followed by IPA

rinse, air dry and baked at 150 °C for 10 mins. Step 2: A layers of photoresist (PMGI SF6) was spin-coated (3500 rpm, 45s) onto the wafer surface followed by a soft-bake at 170 °C for 5 mins. Another layer of photoresist (Shipley S1827) was spin-coated on top of SF6 layer using the same spin speed and duration, followed by a soft-bake at 115 °C for 90 s. The coated wafer was then brought in contact with the photomask and exposed to UV light (10 mW/cm2 @ 365 nm, 20 s) using Karl Suss MA6 Mask Aligner. The exposed photoresist was developed for 60 s using Microposit MF-319, rinsed with DI water and air dried. Ti (10 nm)/Au (50 nm) were deposited by e-beam evaporation, followed by a lift-off process using Remover PG for ~10 hours. The source-drain base electrodes were made. Step 3: A layer of e-beam resist (MicroChem PMMA A6) was spin-coated (3500 rpm, 45s) onto the base electrodes, and then baked at 180 °C for 90 s. Tiny scratches were created near the area under e-beam lithography for focus check. The devices were then aligned under SEM and exposed/patterned by e-beam to form the fine electrode tips (shown in the “top view”). The exposed PMMA was developed for 60 s in 1:3 MIBK:IPA solution, followed by IPA rinse, DI water rinse and air dry. Ti (10 nm)/Au (30 nm) were deposited by e-beam evaporation, followed by a lift-off process using Remover PG for ~10 hours. Low power sonication was used for 10 s in the end. The devices were then rinsed by fresh Remover PG followed by DI water rinse and air dry. Now the fine-tip electrodes were made onto the base electrodes. Step 4: The devices were dehydrated on top of a hotplate with the temperature slowly ramping up from room temperature to 180 °C and stayed for 10 mins. After cooling down, the devices were spin-coated (500 rpm, 10 s and then 3500 rpm, 50 s) with a layer of negative photoresist (MicroChem SU-8) as the dielectric layer. The coated SU-8 layer was then soft-baked with temperature ramping from 65 °C to 95 °C at 5 °C/min, staying at 95 °C

for 2 mins before cooling down. The devices were aligned and brought in contact with the photomask and exposed to UV light (10 mW/cm2 @ 365 nm) for 9 s. The exposed SU-8 was developed for 2 mins with sonication used in the last 30 seconds and continuing to develop in a fresh developer for 1 more minute with sonication, followed by IPA rinse, DI water rinse and air dry. The patterned SU-8 was then exposed to a UV lamp for 3 mins and crosslinked on a hotplate with the temperature slowly ramping up from room temperature to 200 °C and stayed for 10 mins before cooling down. Now the devices were covered with a dielectric layer with only the electrode tips exposed. Step 5: The devices were cleaned with Remover PG for 3 mins followed by DI water rinse, air dry, and bake for 5 mins at 160 °C. The same process in step 2 was used here to fabricate the metal shield layer, with some changes: 1. oxygen plasma (100W 60 s) was used prior to the metal deposition to etch the SU-8 surface lightly and hence increase the adhesion between SU-8 layer and the metal shield layer. 2. A thicker Ti (30 nm) was deposited instead of 10 nm for the same purpose. 3. The time of the lift-off process was shortened to 3 hours with the help of shaking (60 rpm) to prevent the dissolution of the SU-8 layer and the peel-off of the metal layer. Step 6: The same process in step 4 was used here to fabricate the passivation layer that protects the shield layer. Step 7: After the three-layer structure (dielectric/shield/passivation layers) was made, the devices were brought under oxygen plasma (100 W 10 mins) to etch off any photoresist residue on the tips of the source-drain electrodes. Then, a diluted ultra-purified nanotube suspension (IsoSol-S100 99.9% purity, Nanointegris Inc) was dropped on top of the devices. An AC electric field (1 MHz, 8 V) was applied between the source and drain electrodes for ~3 seconds. A single or a few nanotubes were expected to be attracted, aligned and attached across the source-drain electrodes. The devices were rinsed, air dried

and then baked (160 °C, 5 mins) to increase the bonding between the contact electrodes and the nanotubes. Step 8: PMMA spin-coating and e-beam lithography were used again here to form the final passivation layer, whiles only exposing the middle segment of the nanotubes as the open channel for liquid gating. Step 9: The devices were bonded with a PDMS reservoir to hold liquid. Alcohol treatment was used to prevent bubbles on the hydrophobic surface and then the reservoir was filled with an aqueous electrolyte solution.

Capacitance Measurements. The electrochemical capacitances of the nanotube devices are measured using a lock-in technique (Figure 4.6b, d). A fixed AC voltage δV_{ref} (1 kHz, 50 mV in RMS) plus a varied DC voltage V_{DC} (- 0.7 V ~ 0.3 V) is applied to the electrolyte solution through an Ag/AgCl reference electrode. The corresponding current between the solution and the nanotubes is collected at the source-drain electrodes by the pre-transimpedance-amplifier (FEMTO DLPCA-200, input noise: 13 fA/$\sqrt{Hz}$). The output of the preamplifier is then connected to the lock-in amplifier (Stanford Research SR830, the time constant is set to 3 s with 24 dB/oct roll-off) to narrow down the bandwidth and quantify the complex current I_{meas}. The measured capacitance is then determined by $1/j\omega C_{meas} = \delta V_{ref} / Im(I_{meas})$. The top shield layer and the bottom substrate are grounded so that the large stray capacitances between the solution and the electrode leads and between the leads and the ground are shielded out of the measurement circuit. Additional shields are applied by covering the current collection wires with aluminum foil. After all the shields, the remaining parasitic capacitance is decreased to ~ 1fF.

Chapter 5: Beyond the Debye Screening Length: Scanning Microwave Microscopy of Vital Mitochondria in Respiration Buffer

5.1 Introduction

The ultra-structure of mitochondria is critically related to metabolism and cell death pathways.[88,89] The inner membrane is folded and has cristae necks of diameter ~ 10 nm. The change in this ultrastructure and its relationship to cell death pathways (apoptosis) is controversial and difficult to study, as imaging with optical microscopy lacks the required spatial resolution. Electron microscopy can only provide a snapshot in time of a frozen sample. In addition to ultra-structure, mitochondria are electrically active and sustain a membrane potential of ~ 0.1 V, but there are no tools to patch clamp due to the complex nature of the ultrastructure. Real time nano-probes that have high spatial resolution and function in liquid are needed to further the field of mitochondrial biology. Atomic force microscopy in liquid alone cannot provide this information, as it only provides topological information about the surface of the organelle. The ultrastructural changes are mostly *inside* the organelle and are not imaged by AFM alone.

SMM has the potential to measure the inside of living systems, acting as a “nano-radar”. In dry applications, variable frequency measurements penetrate deep into semiconductor samples (in a frequency dependent way), enabling calibrated measurements of doping

profiles in all three dimensions: X and Y with the physical scan, and Z by varying the frequency. Excellent progress shows spatial resolution of 50 nm and capacitance can be calibrated to the ~100 aF scale.[90] Translating these technological advances into liquid environment presents many challenges, discussed in more depth below. Progress to date includes imaging of the outer shape of vesicles/exosomes[91] in liquid, imaging of the surfaces of cells in culture or tissue[92–94] or even low contrast images of the inside of CHO and E-Coli.[95] However, to date, no images of vital sub-cellular organelles, either inside or outside cells, have ever been published.

In this work, we demonstrate imaging using SMM of vital mitochondria in respiration buffer. The mitochondria are isolated from cultured HeLa cells and tethered to a solid graphene support. The mitochondria are kept vital (alive) using a respiration buffer which provides nutrients to sustain the Krebs cycle. We verify that the mitochondria are "alive" by measuring the membrane potential using a voltage sensitive fluorescent dye (TMRE).[96] The organelles are measured capacitively at 7 GHz. Several technical advances are demonstrated which enable this work: 1) The SMM operates in an electrophysiologically relevant liquid (hence conducting) environment; 2) The SMM operates in tapping mode, averaging the microwave reflection measurement over many tapping periods; 3) A tuned reflectometer enables increased sensitivity; 4) Variable frequencies up to 18 GHz are used; 5) In contrast with traditional matching/resonant methods that exhibit high quality factor that fail in the presence of liquids, interferometric/tuned reflectometer gives the possibility to adjust the quality factor or sensitivity even in the presence of the liquid.

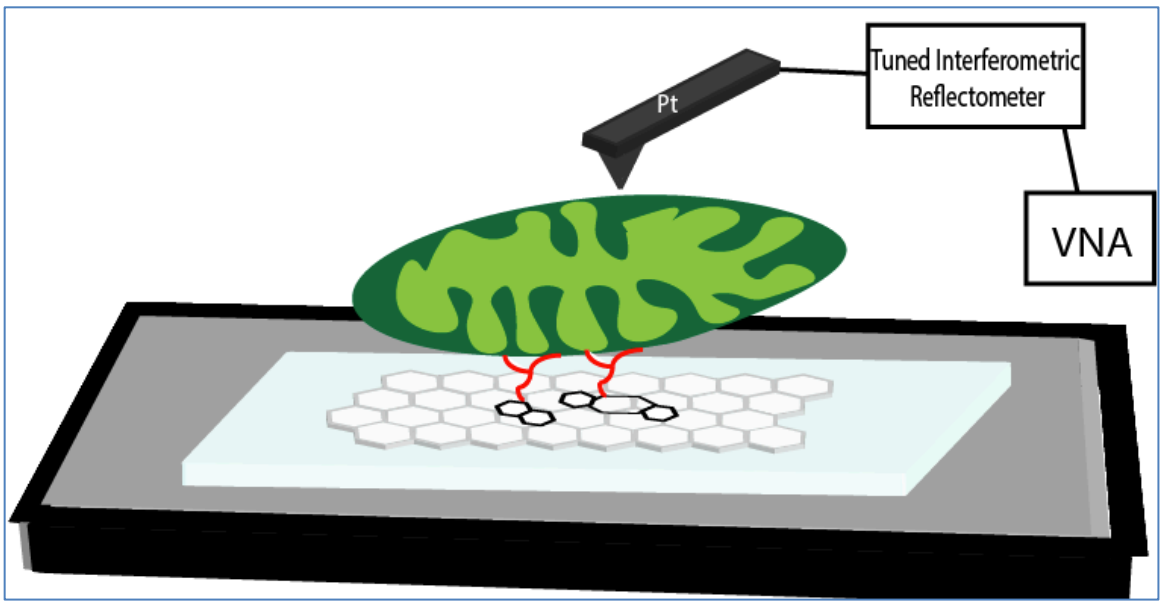

Figure 5.1: Cartoon of a tethered mitochondrion onto a graphene support in a liquid environment. The live mitochondrion is then imaged via SMM tapping mode capability.

5.2 Materials and Methods

5.2.1 Mitochondrial isolation

On the days of the experiment, 10^7 HeLa cells were harvested for mitochondrial isolation. Before isolation, the confluent cells were stained with MitoTracker Green FM and TMRE for 0.5-1 hour. Mitochondria from the cultured cells were isolated using differential centrifugation steps. We followed the isolation protocol described in [97]. From this step forward through tethering and SMM imaging, the isolated mitochondria were suspended in respiration buffer (140 mM KCl, 2 mM MgCl2, 10 mM NaCl, 0.5 mM EGTA, 0.5 mM KH2PO4, 2 mM HEPES, 5 mM succinate, pH 7.2 adjusted with KOH), which results in ADP-stimulated respiration and coupled with oxygen consumption would maintain the isolated mitochondria in a vital state. The isolated mitochondrial samples were then divided into two separate aliquots, one fluorescently imaged for proof of life and the second imaged via SMM. Using an Olympus inverted microscope with two LED excitation sources (490 nm &

565 nm), we observed the red and green fluorescence signals from MitoTracker Green and TMRE. To process and analyze the images, ImageJ software was used.

5.2.2 Graphene device fabrication and functionalization

CVD graphene was transferred onto PDMS and functionalized via a series of solution deposition methods. The graphene transfer and functionalization schemes are described in [97]. Isolated mitochondria were then loaded onto the graphene device and incubated for 15 min at 4°C, followed by a wash to remove the untethered ones before imaging.

5.3 Scanning Microwave Microscope (SMM)

The scanning microwave microscope, from Keysight™ (model 7500) consists of an AFM interfaced with a performance vector network analyzer, as shown in Figure 5.2. A microwave signal is transmitted from the PNA to a conductive AFM probe that operates in tapping mode with the sample being scanned. The probe also serves as a receiver to capture the reflected microwave signal from the contact point. By directly measuring the complex reflection coefficient, the impedance of the sample at each scanned point can be then mapped, simultaneously with the surface topography.[98] In the proposed configuration, a homemade tuned interferometric system is developed to control the interference frequency position and the level of the magnitude of the reflection coefficient. The interferometer is built up in coaxial form with a hybrid coupler, passive and variable phase-shifter and attenuator, and a low-noise amplifier.

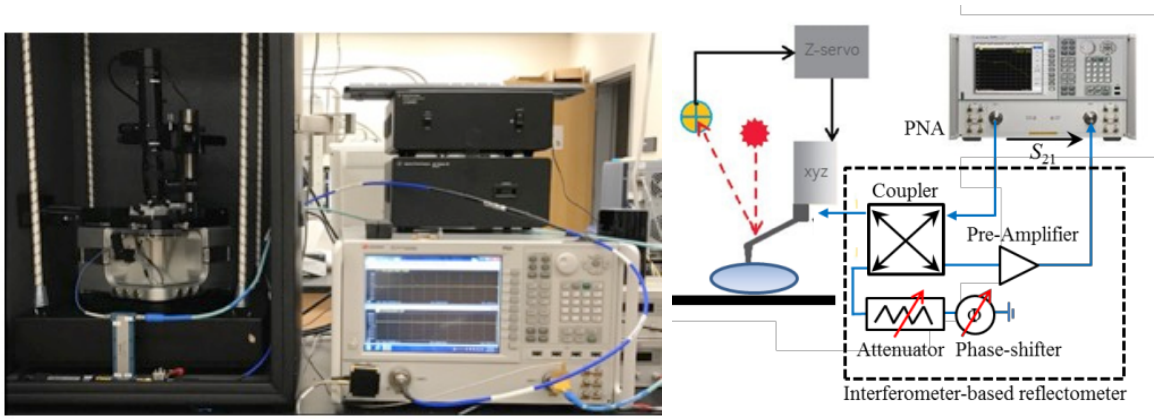

Figure 5.2: The photo and diagram of the SMM setup.

According to Figure 5.2, the basic principle consists of splitting the PNA source microwave signal into two coherent signals, i.e. the reference signal to the AFM tip and the interference signal. The coupler acts as a reflectometer to separate the incident wave and the reflected wave from at the tip interface. The reflected wave is then combined with the interference signal to provide the output signal at the output of the coupler. This signal is cancelled by properly tuning the attenuator and phase-shifter. The resulting signal is amplified and measured by the PNA receiver in transmission mode. The interference signal is shown in Figure 5.3. By changing the variable phase shifter and attenuator in the interferometer's reference arm, the magnitude and position of the interference peaks can be adjusted. At the best impedance match points (purple curve in the inset of Figure 5.3), the system is at the best sensitivity to the tip-sample impedance. Capacitance change down to attofarad can be measured in such condition.[90]

When the tip-sample is immersed into water, there are noticeable changes we can see in Figure 5.3. The S_{21}-spectrum shifted to the small frequency direction by ~0.2GHz. By comparing the image of standard sample at different resonance frequencies, we observed a trend of increasing in the SMM resolution as the microwave frequency going up. In addition,

the resonance phenomenon gets weak when the frequency goes up. To compromise, we choose the peak at ~7GHz to image the mitochondria.

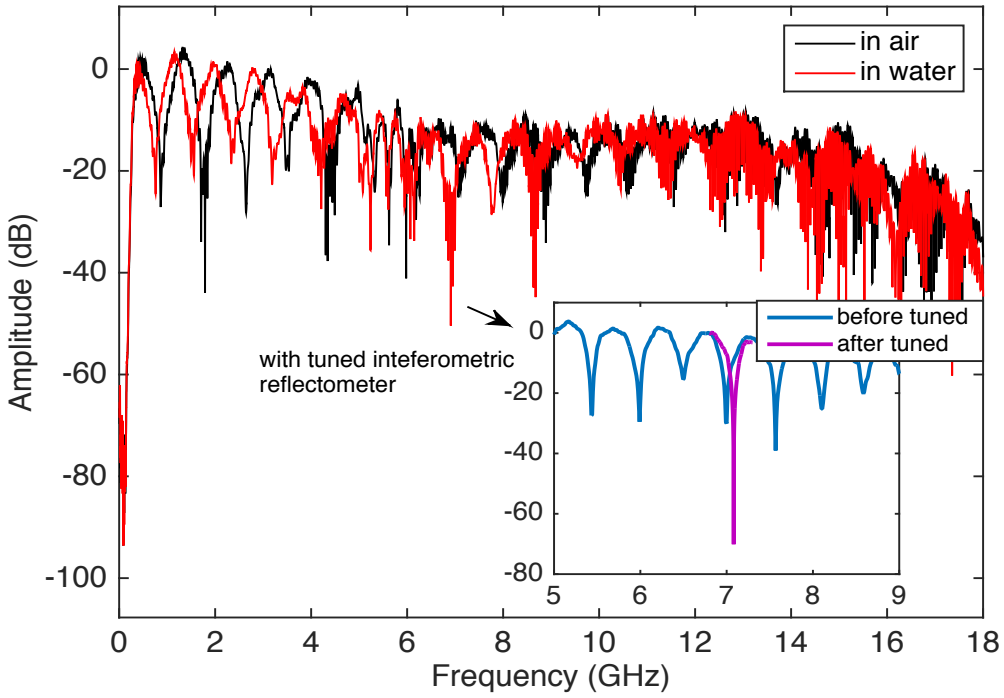

Figure 5.3: The interference signals. The change of the interference signal in water vs. in air. The inset shows the tuning of the interference peak in water.

5.4 Mitochondria Studies

5.4.1 Verification of mitochondria with optical microscopy

Figure 5.4 shows isolated mitochondria from HeLa cancer cell lines that were fluorescently tagged. These organelles were then tethered to the surfaces of graphene coated glass substrates using a step-wise organic functionalization scheme as described in the methods section. The TMRE potentiometric dye is a cell permeant, positively charged dye that accumulates in active mitochondria due to their negative charge, and fails to do so

in inactive or depolarized mitochondria given the diminished charge. As a result, a TMRE fluorescence signal is indicative of the vitality of isolated mitochondria.

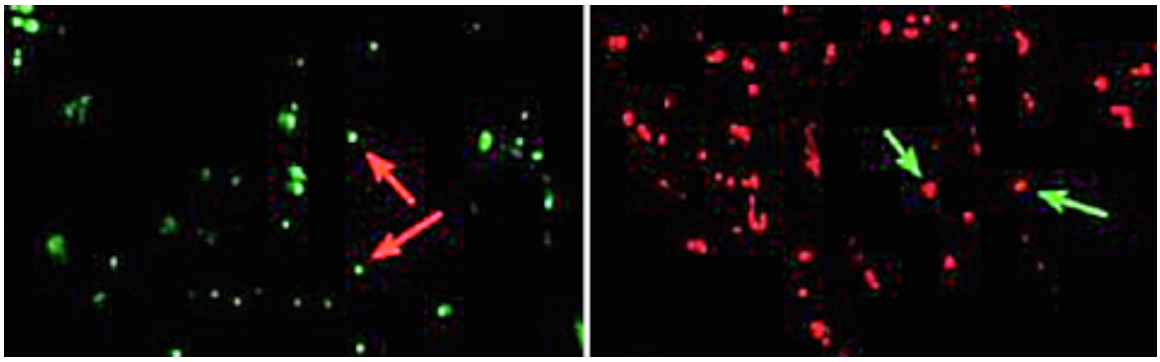

Figure 5.4: The left image shows Mito-Tracker green tagged isolated mitochondria and the right are TMRE potentiometric fluorescently tagged mitochondria. Both images have been modified with added false color.

5.4.2 SMM characterization of mitochondria

The device was brought into contact with the SMM probe in tapping mode with gentle tip-sample interaction to prevent displacement or damage of mitochondria. We then did a tuning of the reflectometer and selected the inference peak at ~7 GHz (Figure 5.3) for mitochondria imaging.

We acquired an uncalibrated capacitance map of a single vital mitochondria as seen in Figure 5.5. The diameter of the mitochondria is ~1 μm. The graphene layer underneath has a surface roughness of a few nm, whose ripples can be seen in the topographic image. Mitochondria, as non-conductive organelles, sitting on the conductive background of graphene, give the SMM image of mitochondria a very sharp contrast. Graphene was used in anticipation of future studies that would exploit its pH sensing capability [97] simultaneously with SMM and AFM studies presented in this manuscript.

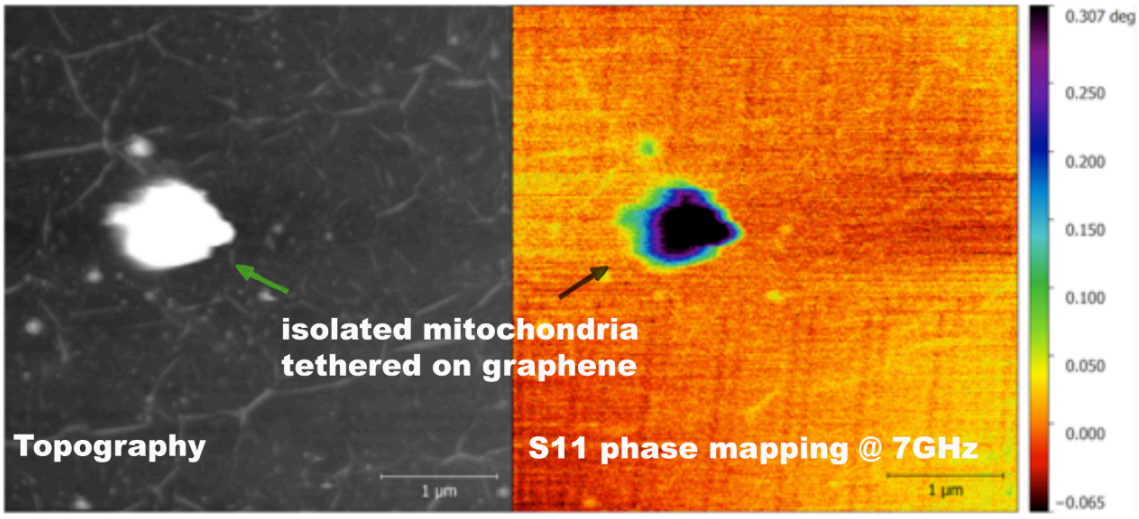

Figure 5.5: A single live mitochondrion (isolated from HeLa cell culture and tethered on graphene support) with standard topographic imaging mode (black and white image), and scanning microwave microscopy (color image)

5.5 Discussion

In this work, we have presented the first SMM image of a vital sub-cellular organelle. The topographic and SMM images are consistent with the known outer morphology of mitochondria. However, the potential advantage of SMM is the ability to see inside the organelle, which has not yet been demonstrated in this work. In principle, this could provide more information than simply topographic mode. In the past, this concept has been proven with dry materials samples, able to penetrate progressively deeper into a solid as the frequency is increased.[99] It is our claim that, having demonstrated SMM imaging of a vital organelle, that this opens a new window of opportunity for future imaging of the ultra-structure of all sorts of organelles. Although mitochondria are of particular interest in medicine and biology[100] and are highly electrically active[101] making them an excellent target for new nano-electronic imaging technologies, the technique should be applicable to other systems such as exosomes, chloroplasts, and bacteria.

5.6 Conclusion

We have demonstrated the first SMM images of vital isolated mitochondria in physiologically relevant respiration buffer. The mitochondrial capacitance is assayed and imaged. This represents proof of concept of SMM in electrophysiologically active organelles, which provides information complementary to optical and electron microscopies. Since this approach is fully functional in biological buffer, it enables studies of the changes mitochondria undergo under different chemical environments, such as cell death signals (e.g. BCL2 proteins), different metabolites, mitochondrial ROS, and many other studies, all in real time.

Bibliography

(1) Hodgkin, A. L.; Huxley, A. F. A Quantitative Description of Membrane Current and Its Application to Conduction and Excitation in Nerve. *J. Physiol.* **1952**, *117*, 500–544.

(2) Jalife, J.; Delmar, M.; Anumonwo, J.; Berenfeld, O.; Kalifa, J. *Basic Cardiac Electrophysiology for the Clinician*; John Wiley & Sons, 2011.

(3) Nicholls, D. G.; Ferguson, S. J. *Bioenergetics*; Elsevier, 2002.

(4) Chen, T.; Peng, H.; Durstock, M.; Dai, L. High-Performance Transparent and Stretchable All-Solid Supercapacitors Based on Highly Aligned Carbon Nanotube Sheets. *Sci. Rep.* **2014**, *4*, 3612.

(5) Dunn, B.; Kamath, H.; Tarascon, J.-M. Electrical Energy Storage for the Grid: A Battery of Choices. *Science* **2011**, *334*, 928–935.

(6) Béguin, F.; Frackowiak, E. *Carbons for Electrochemical Energy Storage and Conversion Systems*; CRC Press: Boca Raton, FL, 2010.

(7) Yang, N.; Chen, X.; Ren, T.; Zhang, P.; Yang, D. Carbon Nanotube Based Biosensors. *Sens. Actuators. B. Chem.* **2015**, *207*, 690–715.

(8) Ilani, S.; Donev, L. A. K.; Kindermann, M.; McEuen, P. L. Measurement of the Quantum Capacitance of Interacting Electrons in Carbon Nanotubes. *Nat. Phys.* **2006**, *2*, 687–691.

(9) Chmiola, J. Anomalous Increase in Carbon Capacitance at Pore Sizes Less Than 1 Nanometer. *Science* **2006**, *313*, 1760–1763.

(10) Kondrat, S.; Wu, P.; Qiao, R.; Kornyshev, A. A. Accelerating Charging Dynamics in Subnanometre Pores. *Nat. Mater.* **2014**, *13*, 387–393.

(11) Lee, A. A.; Kondrat, S.; Kornyshev, A. A. Single-File Charge Storage in Conducting Nanopores. *Phys. Rev. Lett.* **2014**, *113*, 048701.

(12) Kondrat, S.; Georgi, N.; Fedorov, M. V.; Kornyshev, A. A. A Superionic State in Nano-Porous Double-Layer Capacitors: Insights from Monte Carlo Simulations. *Phys. Chem. Chem. Phys.* **2011**, *13*, 11359–11366.

(13) Wang, H.; Pilon, L. Accurate Simulations of Electric Double Layer Capacitance of Ultramicroelectrodes. *J. Phys. Chem. C* **2011**, *115*, 16711–16719.

(14) Henstridge, M. C.; Dickinson, E. J. F.; Compton, R. G. On the Estimation of the Diffuse Double Layer of Carbon Nanotubes Using Classical Theory: Curvature Effects on the Gouy-Chapman Limit. *Chem. Phys. Lett.* **2010**, *485*, 167–170.

(15) Pak, A. J.; Paek, E.; Hwang, G. S. Relative Contributions of Quantum and Double Layer Capacitance to the Supercapacitor Performance of Carbon Nanotubes in an Ionic Liquid. *Phys. Chem. Chem. Phys.* **2013**, *15*, 19741–19747.

(16) Li, J.; Pham, P. H. Q.; Zhou, W.; Pham, T. D.; Burke, P. J. Carbon-Nanotube-Electrolyte Interface: Quantum and Electric Double Layer Capacitance. *ACS Nano* **2018**, *12*, 9763–9774.

(17) Ilani, S.; Mceuen, P. L. Electron Transport in Carbon Nanotubes. *Annu. Rev. Condens. Matter Phys* **2010**, *1*, 1–25.

(18) Hároz, E. H.; Kim, J.-H.; Kono, J.; Nanot, S.; Hauge, R. H. Optoelectronic Properties of Single-Wall Carbon Nanotubes. *Adv. Mater.* **2012**, *24*, 4977–4994.

(19) Bard, A. J.; Faulkner, L. R. *Electrochemical Methods. Fundamentals and Applications*, 2nd ed.; John Wiley & Sons, Inc.: New York, 2001.

(20) Maribo-Mogensen, B.; Kontogeorgis, G. M.; Thomsen, K. Comparison of the Debye–Hückel and the Mean Spherical Approximation Theories for Electrolyte Solutions. *Ind. Eng. Chem. Res.* **2012**, *51*, 5353–5363.

(21) Loehe, J. R.; Donohue, M. D. Recent Advances in Modeling Thermodynamic Properties of Aqueous Strong Electrolyte Systems. *AIChE J.* **1997**, *43*, 180–195.

(22) Henderson, D.; Jiang, D.; Jin, Z.; Wu, J. Application of Density Functional Theory To Study the Double Layer of an Electrolyte with an Explicit Dimer Model for the Solvent. *J. Phys. Chem. B* **2012**, *116*, 11356–11361.

(23) Kornyshev, A. A.; Partenskii, M. B.; Schmickler, W. Self-Consistent Density Functional Approach to a Metal/Electrolyte Solution Interface. *Zeitschrift für Naturforsch. A* **1984**, *39*, 1122–1133.

(24) Bagotsky, V. S. *Fundamentals of Electrochemistry*, 2nd ed.; John Wiley & Sons, Inc.: New Jersey, 2005.

(25) Brown, M. A.; Goel, A.; Abbas, Z. Effect of Electrolyte Concentration on the Stern Layer Thickness at a Charged Interface. *Angew.Chem. Int. Ed.* **2016**, *55*, 3790–3794.

(26) Simon, P.; Gogotsi, Y. Materials for Electrochemical Capacitors. *Nat. Mater.* **2008**, *7*, 845–854.

(27) Simon, P.; Gogotsi, Y. Charge Storage Mechanism in Nanoporous Carbons and Its Consequence for Electrical Double Layer Capacitors. *Philos. Trans. R. Soc. A Math. Phys. Eng. Sci.* **2010**, *368*, 3457–3467.

(28) Forse, A. C.; Merlet, C.; Griffin, J. M.; Grey, C. P. New Perspectives on the Charging Mechanisms of Supercapacitors. *J. Am. Chem. Soc.* **2016**, *138*, 5731–5744.

(29) Kondrat, S.; Kornyshev, A. A. Pressing a Spring: What Does It Take to Maximize the Energy Storage in Nanoporous Supercapacitors? *Nanoscale Horiz.* **2016**, *1*, 45–52.

(30) Rochester, C. C.; Kondrat, S.; Pruessner, G.; Kornyshev, A. A. Charging Ultrananoporous Electrodes with Size-Asymmetric Ions Assisted by Apolar Solvent. *J. Phys. Chem. C* **2016**, *120*, 16042–16050.

(31) Kornyshev, A. A. The Simplest Model of Charge Storage in Single File Metallic Nanopores. *Faraday Discuss.* **2013**, *164*, 117–133.

(32) Kondrat, S.; Kornyshev, A. Corrigendum: Superionic State in Double-Layer Capacitors with Nanoporous Electrodes. *J. Phys. Condens. Matter* **2013**, *25*, 119501.

(33) Chen, H.; Zeng, S.; Chen, M.; Zhang, Y.; Li, Q. Fabrication and Functionalization of Carbon Nanotube Films for High-Performance Flexible Supercapacitors. *Carbon N. Y.* **2015**,

92, 271–296.

(34) Malik, R.; Zhang, L.; McConnell, C.; Schott, M.; Hsieh, Y. Y.; Noga, R.; Alvarez, N. T.; Shanov, V. Three-Dimensional, Free-Standing Polyaniline/Carbon Nanotube Composite-Based Electrode for High-Performance Supercapacitors. *Carbon N. Y.* **2017**, *116*, 579–590.

(35) Barisci, J. N.; Wallace, G. G.; Baughman, R. H. Electrochemical Studies of Single-Wall Carbon Nanotubes in Aqueous Solutions. *J. Electroanal. Chem.* **2000**, *488*, 92–98.

(36) Rutherglen, C.; Burke, P. Nanoelectromagnetics: Circuit and Electromagnetic Properties of Carbon Nanotubes. *Small* **2009**, *5*, 884–906.

(37) Ilani, S.; Donev, L. A. K.; Kindermann, M.; McEuen, P. L. Measurement of the Quantum Capacitance of Interacting Electrons in Carbon Nanotubes. *Nat. Phys.* **2006**, *2*, 687–691.

(38) Xia, J.; Chen, F.; Li, J.; Tao, N. Measurement of the Quantum Capacitance of Graphene. *Nat. Nanotechnol.* **2009**, *4*, 505–509.

(39) Xu, H.; Zhang, Z.; Peng, L.-M. Measurements and Microscopic Model of Quantum Capacitance in Graphene. *Appl. Phys. Lett.* **2011**, *98*, 133122.

(40) Rouhi, N.; Jain, D.; Burke, P. J. High-Performance Semiconducting Nanotube Inks: Progress and Prospects. *ACS Nano* **2011**, *5*, 8471–8487.

(41) Bisquert, J. Theory of the Impedance of Electron Diffusion and Recombination in a Thin Layer. *J. Phys. Chem. B* **2002**, *106*, 325–333.

(42) Heller, I.; Kong, J.; Williams, K. A.; Dekker, C.; Lemay, S. G. Electrochemistry at Single-Walled Carbon Nanotubes: The Role of Band Structure and Quantum Capacitance. *J. Am. Chem. Soc.* **2006**, *128*, 7353–7359.

(43) Brug, G. J.; van den Eeden, A. L. G.; Sluyters-Rehbach, M.; Sluyters, J. H. The Analysis of Electrode Impedances Complicated by the Presence of a Constant Phase Element. *J. Electroanal. Chem.* **1984**, *176*, 275–295.

(44) Bisquert, J.; Garcia-Belmonte, G.; Bueno, P.; Longo, E.; Bulhões, L. O. S. Impedance of Constant Phase Element (CPE)-Blocked Diffusion in Film Electrodes. *J. Electroanal. Chem.* **1998**, *452*, 229–234.

(45) Shoar Abouzari, M. R.; Berkemeier, F.; Schmitz, G.; Wilmer, D. On the Physical Interpretation of Constant Phase Elements. *Solid State Ionics* **2009**, *180*, 922–927.

(46) Pajkossy, T. Impedance of Rough Capacitive Electrodes. *J. Electroanal. Chem.* **1994**, *364*, 111–125.

(47) Leiva, E. P. M.; Sánchez, C. G.; Vélez, P.; Schmickler, W. Theory of Electrochemical Monoatomic Nanowires. *Phys. Rev. B* **2006**, *74*, 035422.

(48) Hatlo, M. M.; van Roij, R.; Lue, L. The Electric Double Layer at High Surface Potentials: The Influence of Excess Ion Polarizability. *Europhys. Lett.* **2012**, *97*, 28010.

(49) Goodwin, Z. A. H.; Feng, G.; Kornyshev, A. A. Mean-Field Theory of Electrical Double Layer In Ionic Liquids with Account of Short-Range Correlations. *Electrochim. Acta* **2017**, *225*, 190–197.

(50) Mohammadzadeh, L.; Quaino, P.; Schmickler, W. Interactions of Anions and Cations in Carbon Nanotubes. *Faraday Discuss.* **2016**, *193*, 415–426.

(51) Schmickler, W.; Henderson, D. Charge Storage in Nanotubes: The Case of a 2-1 Electrolyte. *Condens. Matter Phys.* **2017**, *20*, 33004.

(52) Schmickler, W.; Henderson, D. On the Capacitance of Narrow Nanotubes. *Phys. Chem. Chem. Phys.* **2017**, *19*, 20393–20400.

(53) Mohammadzadeh, L.; Goduljan, A.; Juarez, F.; Quaino, P.; Santos, E.; Schmickler, W. Nanotubes for Charge Storage – towards an Atomistic Model. *Electrochim. Acta* **2015**, *162*, 11–16.

(54) Goduljan, A.; Juarez, F.; Mohammadzadeh, L.; Quaino, P.; Santos, E.; Schmickler, W. Screening of Ions in Carbon and Gold Nanotubes — A Theoretical Study. *Electrochem. commun.* **2014**, *45*, 48–51.

(55) Schmickler, W. A Simple Model for Charge Storage in a Nanotube. *Electrochim. Acta* **2015**, *173*, 91–95.

(56) Rochester, C. C.; Pruessner, G.; Kornyshev, A. A. Statistical Mechanics of "Unwanted Electroactuation" in Nanoporous Supercapacitors. *Electrochim. Acta* **2015**, *174*, 978–984.

(57) Burt, R.; Birkett, G.; Zhao, X. S. A Review of Molecular Modelling of Electric Double Layer Capacitors. *Phys. Chem. Chem. Phys.* **2014**, *16*, 6519–6538.

(58) Kilic, M. S.; Bazant, M. Z.; Ajdari, A. Steric Effects in the Dynamics of Electrolytes at Large Applied Voltages. I. Double-Layer Charging. *Phys. Rev. E* **2007**, *75*, 021502.

(59) Nightingale, E. R. Phenomenological Theory of Ion Solvation. Effective Radii of Hydrated Ions. *J. Phys. Chem.* **1959**, *63*, 1381–1387.

(60) Butt, H.; Graf, K.; Kappl, M. *Physics and Chemistry of Interfaces*; Wiley-VCH: New York, 2003.

(61) Gavryushov, S.; Linse, P. Polarization Deficiency and Excess Free Energy of Ion Hydration in Electric Fields. *J. Phys. Chem. B* **2003**, *107*, 7135–7142.

(62) Liang, J.; Akinwande, D.; Wong, H.-S. P. Carrier Density and Quantum Capacitance for Semiconducting Carbon Nanotubes. *J. Appl. Phys.* **2008**, *104*, 064515.

(63) Wang, Y. Y.; Pham, T. D.; Zand, K.; Li, J.; Burke, P. J. Charging the Quantum Capacitance of Graphene with a Single Biological Ion Channel. *ACS Nano* **2014**, *8*, 4228–4238.

(64) Kornyshev, A. A.; Luque, N. B.; Schmickler, W. Differential Capacitance of Ionic Liquid Interface with Graphite: The Story of Two Double Layers. *J. Solid State Electrochem.* **2014**, *18*, 1345–1349.

(65) Yang, Z.; Wu, H. The Electrochemical Impedance Measurements of Carbon Nanotubes. *Chem. Phys. Lett.* **2001**, *343*, 235–240.

(66) Ströck, M. Eight Allotropes of Carbon https://commons.wikimedia.org/wiki/File:Eight_Allotropes_of_Carbon.png.

(67) Zarr, R. The Curse of Moore's Law

https://energyzarr.typepad.com/energyzarrnationalcom/2009/05/the-curse-of-moores-law.html.

(68) Wang, W. CMOS-Nano Hybrid Research of CNSE NanoDesign and Modeling Group http://www.nanotech-now.com/columns/?article=217.

(69) Pugliese, K. M.; Tolga Gul, O.; Choi, Y.; Olsen, T. J.; Sims, P. C.; Collins, P. G.; Weiss, G. A. Processive Incorporation of Deoxynucleoside Triphosphate Analogs by Single-Molecule DNA Polymerase i (Klenow Fragment) Nanocircuits. *J. Am. Chem. Soc.* **2015**, *137*, 9587–9594.

(70) Stern, E.; Klemic, J. F.; Routenberg, D. a; Wyrembak, P. N.; Turner-Evans, D. B.; Hamilton, A. D.; LaVan, D. a; Fahmy, T. M.; Reed, M. A. Label-Free Immunodetection with CMOS-Compatible Semiconducting Nanowires. *Nature* **2007**, *445*, 519–522.

(71) Francoislaforge. Scanning electrochemical microscopy https://commons.wikimedia.org/wiki/File:Fig2_SECM.jpg.

(72) Wipf, M.; Stoop, R. L.; Navarra, G.; Rabbani, S.; Ernst, B.; Bedner, K.; Schönenberger, C.; Calame, M. Label-Free FimH Protein Interaction Analysis Using Silicon Nanoribbon BioFETs. *ACS Sensors* **2016**, *1*, 781–788.

(73) Kim, D. R.; Lee, C. H.; Zheng, X. Probing Flow Velocity with Silicon Nanowire Sensors. *Nano Lett.* **2009**, *9*, 1984–1988.

(74) Lee, J.; Wipf, M.; Mu, L.; Adams, C.; Hannant, J.; Reed, M. A. Metal-Coated Microfluidic Channels: An Approach to Eliminate Streaming Potential Effects in Nano Biosensors. *Biosens. Bioelectron.* **2017**, *87*, 447–452.

(75) Lu, Y. R.; Bangsaruntip, S.; Wang, X. R.; Zhang, L.; Nishi, Y.; Dai, H. J. DNA Functionalization of Carbon Nanotubes for Ultrathin Atomic Layer Deposition of High Kappa Dielectrics for Nanotube Transistors with 60 MV/Decade Switching. *J. Am. Chem. Soc.* **2006**, *128*, 3518–3519.

(76) Banerjee, S.; White, B.; Huang, L.; Rego, B. J.; O'Brien, S.; Herman, I. P. Precise Positioning of Carbon Nanotubes by Ac Dielectrophoresis Using Floating Posts. *Appl. Phys. A Mater. Sci. Process.* **2007**, *86*, 415–419.

(77) Dimaki, M.; Bøggild, P. Dielectrophoresis of Carbon Nanotubes Using Microelectrodes: A Numerical Study. *Nanotechnology* **2004**, *15*, 1095–1102.

(78) Stokes, P.; Khondaker, S. I. Local-Gated Single-Walled Carbon Nanotube Field Effect Transistors Assembled by AC Dielectrophoresis. *Nanotechnology* **2008**, *19*, 175202.

(79) Vijayaraghavan, A.; Oron-Carl, M.; Blatt, S.; Vijayaraghavan, A.; Blatt, S.; Weissenberger, D.; Weissenberger, D.; Oron-Carl, M.; Hennrich, F.; Hennrich, F.; et al. Ultra-Large-Scale Directed Assembly of Single-Walled Carbon Nanotube Devices. Supporting Information. *Nano Lett.* **2007**, *7*, 1556–1560.

(80) Sorgenfrei, S.; Meric, I.; Banerjee, S.; Akey, A.; Rosenblatt, S.; Herman, I. P.; Shepard, K. L. Controlled Dielectrophoretic Assembly of Carbon Nanotubes Using Real-Time Electrical Detection. *Appl. Phys. Lett.* **2009**, *94*, 1–3.

(81) Islam, M. R.; Joung, D.; Khondaker, S. I. Towards Parallel Fabrication of Single Electron

Transistors Using Carbon Nanotubes. *Nanoscale* **2015**, *7*, 9786–9792.

(82) Männik, J.; Heller, I.; Janssens, A. M.; Lemay, S. G.; Dekker, C. Charge Noise in Liquid-Gated Single-Wall Carbon Nanotube Transistors. *Nano Lett.* **2008**, *8*, 685–688.

(83) Sharf, T.; Wang, N. P.; Kevek, J. W.; Brown, M. A.; Wilson, H.; Heinze, S.; Minot, E. D. Single Electron Charge Sensitivity of Liquid-Gated Carbon Nanotube Transistors. *Nano Lett.* **2014**, *14*, 4925–4930.

(84) Kim, W.; Javey, a; Vermesh, O.; Wang, O.; Li, Y. M.; Dai, H. J. Hysteresis Caused by Water Molecules in Carbon Nanotube Field-Effect Transistors. *Nano Lett.* **2003**, *3*, 193–198.

(85) Mintmire, J. W.; White, C. T. Universal Density of States for Carbon Nanotubes. *Phys. Rev. Lett.* **1998**, *81*, 2506–2509.

(86) Liang, J.; Akinwande, D.; Wong, H.-S.-S. P. S. P. Carrier Density and Quantum Capacitance for Semiconducting Carbon Nanotubes. *J. Appl. Phys.* **2008**, *104*, 064515.

(87) Crosser, M. S.; Brown, M. a.; McEuen, P. L.; Minot, E. D. Determination of the Thermal Noise Limit of Graphene Biotransistors. *Nano Lett.* **2015**, 150720103852006.

(88) Cogliati, S.; Enriquez, J. A.; Scorrano, L. Mitochondrial Cristae: Where Beauty Meets Functionality. *Trends Biochem. Sci.* **2016**, *41*, 261–273.

(89) Perkins, G. A.; Ellisman, M. H. Remodeling of Mitochondria in Apoptosis. In *Mitochondria and Cell Death*; Hockenbery, D. M., Ed.; Springer New York: New York, NY, 2016; pp 85–110.

(90) Dargent, T.; Haddadi, K.; Lasri, T.; Clément, N.; Ducatteau, D.; Legrand, B.; Tanbakuchi, H.; Theron, D. An Interferometric Scanning Microwave Microscope and Calibration Method for Sub-FF Microwave Measurements. *Rev. Sci. Instrum.* **2013**, *84*, 123705.

(91) Jin, X.; Hwang, J. C. M.; Farina, M.; Di Donato, A.; Mencarelli, D.; Morini, A.; Venanzoni, G.; De Angelis, F.; Piacenza, F.; Malavolta, M.; et al. Imaging of Exosomes by Broadband Scanning Microwave Microscopy. In *2016 46th European Microwave Conference (EuMC)*; IEEE, 2016; pp 1211–1214.

(92) Farina, M.; Piacenza, F.; De Angelis, F.; Mencarelli, D.; Morini, A.; Venanzoni, G.; Pietrangelo, T.; Malavolta, M.; Basso, A.; Provinciali, M.; et al. Investigation of Fullerene Exposure of Breast Cancer Cells by Time-Gated Scanning Microwave Microscopy. *IEEE Trans. Microw. Theory Tech.* **2016**, *64*, 4823–4831.

(93) Farina, M.; Mencarelli, D.; Morini, A.; Pierantoni, L.; Jin, X.; Hwang, J. Developments of Microwave Microscopy for Application to Biological Samples. In *2017 International Conference on Manipulation, Automation and Robotics at Small Scales (MARSS)*; IEEE, 2017; pp 1–5.

(94) Farina, M.; Di Donato, A.; Monti, T.; Pietrangelo, T.; Da Ros, T.; Turco, A.; Venanzoni, G.; Morini, A. Tomographic Effects of Near-Field Microwave Microscopy in the Investigation of Muscle Cells Interacting with Multi-Walled Carbon Nanotubes. *Appl. Phys. Lett.* **2012**, *101*, 203101.

(95) Tuca, S.-S.; Badino, G.; Gramse, G.; Brinciotti, E.; Kasper, M.; Oh, Y. J.; Zhu, R.; Rankl, C.; Hinterdorfer, P.; Kienberger, F. Calibrated Complex Impedance of CHO Cells and E . Coli

Bacteria at GHz Frequencies Using Scanning Microwave Microscopy. *Nanotechnology* **2016**, *27*, 135702.

(96) Nicholls, D. G. Fluorescence Measurement of Mitochondrial Membrane Potential Changes in Cultured Cells. In *Mitochondrial Bioenergetics: Methods and Protocols*; Palmeira, C. M., Moreno, A., Eds.; Humana Press: New York, 2012; pp 119–133.

(97) Pham, T. D.; Pham, P. Q.; Li, J.; Letai, A. G.; Wallace, D. C.; Burke, P. J. Cristae Remodeling Causes Acidification Detected by Integrated Graphene Sensor during Mitochondrial Outer Membrane Permeabilization. *Sci. Rep.* **2016**, *6*, 35907.

(98) Wu, S.; Kienberger, F.; Tanbakuchi, H. Scanning Microwave Microscopy: Advances In Quantitative Capacitance And Carrier Density Measurements At The Nanometer Scale. In *Scanning Probe Microscopy for Energy Research*; Bonnell, D. A., Kalinin, S. V., Eds.; World Scientific: Singapore, 2013; pp 481–512.

(99) Plassard, C.; Bourillot, E.; Rossignol, J.; Lacroute, Y.; Lepleux, E.; Pacheco, L.; Lesniewska, E. Detection of Defects Buried in Metallic Samples by Scanning Microwave Microscopy. *Phys. Rev. B* **2011**, *83*, 121409.

(100) Wallace, D. C. Bioenergetic Origins of Complexity and Disease. *Cold Spring Harb. Symp. Quant. Biol.* **2011**, *76*, 1–16.

(101) Huser, J.; Blatter, L. A. Fluctuations in Mitochondrial Membrane Potential Caused by Repetitive Gating of the Permeability Transition Pore. *Biochem. J.* **1999**, *343*, 311–317.